Modeling of Continuum Transport and Meso-Scale Kinetics during Solution Crystal Growth

A THESIS
SUBMITTED TO THE FACULTY OF THE GRADUATE SCHOOL
OF THE UNIVERSITY OF MINNESOTA
BY

Wei Wang

IN PARTIAL FULFILLMENT OF THE REQUIREMENTS
FOR THE DEGREE OF
DOCTOR OF PHILOSOPHY

Jeffrey J. Derby, Adviser

May, 2014

Acknowledgments

There are many people that helped and supported me during my graduate studies in Minnesota.

First and foremost, I thank my advisor Jeffrey J. Derby. From him, I have learned not only the fundamental knowledge I need to finish this thesis, but more importantly how to solve a problem and how to present my work clearly. Jeff also showed the students how to be a nice and graceful person, and a good leader. I'm very grateful to have Jeff as my advisor.

I need to thank my committee members Professors Satish Kumar, Victor Barocas, and Xiang Cheng. I caused them lots of inconvenience due to my remote location when finishing up my thesis. I thank them for being patient and supportive with me, and thank them for their time and understanding.

I thank the Derby group members, Andrew Yeckel, David Gasperino, Yong-Il Kwon, Lisa Lun, Nan Zhang, Parthiv Daggolu, Gaurab Samanta, Hui Xie, who accompanied me in 281 Amundson Hall during my graduate studies. All derby group members know how important Andrew is. I can't complete this thesis without Andrew's help and support. I learned a lot from the other Derby members while working and/or talking with them. It's lucky for me to get to know these talented people.

I want thank the staff members in the CEMS department who really helped making my life delightful. I thank Julie Prince for being Julie Prince. Julie's warm smile always brightened up my days. She helped me with too many things for me to list them here. I also thank Teresa Bredahl, to whom I always turned when I have a hard-to-classify question. And I thank Mary Nissen, who made the complicated payroll procedure so easy for us CEMS students.

Additionally, I can't finish this thesis without the love and support from my family, and my life in Minnesota would be boring and dull without the wonderful friends I met here.

At last but not least, I thank my dear husband, Siguang Sui, for whom I became who I am.

to my husband, Siguang Sui,
my mom, Xianqiu Huang
and my dad, Jiakuan Wang

Abstract

Solution crystal growth is widely applied in many industries and fundamental research, and it is employed to crystallize materials ranging from inorganic molecules, small organic molecules, to large organic molecules. However, despite the broad application, fundamental factors regarding this crystal growth process are not well understood. In this thesis, numerical models are developed to study the influences of macro-scale mass transfer limitations and meso-scale growth kinetics on solution crystal growth.

A parallel, finite element model is implemented to compute three-dimensional fluid flow and mass transfer during crystal growth and is especially applied to the growth systems in Atomic Force Microscopy fluid cells. This work assesses the parametric sensitivity of growth conditions to factors such as the strength of flow, the frequency of scanning motion, the size of the crystal, and the kinetics of the growing surface. Accounting for such effects will be very important to understand solution crystal growth and to interpret AFM measurements of growth dynamics. Additionally, a simplified two-dimensional numerical model focused on the region near the growing crystal surface and the AFM cantilever was developed based on the calculated results of the three-dimensional model. With this two-dimensional model, we provide basic understanding of the fluid flow and mass transfer where the AFM measurements were made, and simplified the revision of AFM measurements interpretation.

A fundamental theoretical model based on the phase-field approach is developed to simulate nano-scale island growth and spiral step growth on crystal surfaces in a supersaturated liquid and is validated by comparison to zinc oxide nanowires synthesis experiments. Results obtained by this work help to explain how experimental factors affect the crystal growth and crystal microstructures and the correlation between island growth and spiral growth mechanisms.

Contents

List of Tables

List of Figures

Chapter 1

Introduction

Contents

The formation of crystals is called crystal growth or crystallization. This is a phase-transition process, during which atoms and molecules from a disordered melt or solution phase self-assemble into an highly ordered solid phase. This process is so beautiful that it is called "the art" in one of the famous text books about crystal growth [24]. This procedure is normally very complicated and requires the control of many parameters that correlate nonlinearly to each other [104]. Especially for solution crystal growth from liquid solutions, since the mass transport of solute molecules through a liquid phase is quite slow, besides crystal growth factors, the mass transfer effects need to be taken into account to fully understand this process. Although both experimental techniques and modern characterization techniques have led to a deeper understanding of solution crystal growth process, many of the mechanisms that occur during growth cannot be directly measured in experi-

ments. As a result, mathematical modeling plays an important role in the understanding of solution crystal growth.

The work presented in this thesis is focused on applying mathematical models to understand solution crystal growth from liquid phase. This work consists of two parts. The first part is a macro-scale fluid dynamics study focused on the mass transport limitations during solution crystal growth, and the second part is a meso-scale phase-field study on the growth kinetics during crystal growth from liquid phase. Impact of factors in both length scales are very important in solution crystal growth process, and both parts of this work contribute to our understanding of this growth process.

1.1 Solution Crystal Growth

Crystals can form from melt phase, solution phase or vapor phase. Müller and Friedrich laid out a very clear overview chart of bulk crystal growth methods, as shown in Fig.1.1 [88]. Among all methods shown in this figure, crystal growth from the melt (melt crystal growth) and growth from solutions (solution crystal growth) are most common and important for the growth of bulk crystals. Melt crystal growth is the traditional technology of manufacturing many crystals, including high-tech products for electronics, photonics and solar cells. However, many materials undergo phase transitions below their melting temperature. To produce crystals of these materials, melt growth would not be applicable, and solution crystal growth becomes the method of choice. Solution crystal growth is applied to produce a variety of crystals, including single crystals of various oxide materials, such as yttrium iron garnet (YIG) and yttrium aluminum garnet (YAG) [19,43,64], non-linear optical materials such as potassium dihydrogen phosphate (KDP) and potassium titanyl phosphate (KTP) [33, 143], semi-organic crystals [5], crystals of small organic molecules [111], and crystals of large organic molecules like proteins [114, 117]. Furthermore, in the modern nano technology, solution crystal growth is applied to synthesize nano particles [85,95] and nanowires [10, 82]. In addition, solution crystal growth is also widely applied in chemical separations [78, 136].

Despite the broad application of solution crystal growth, many fundamental factors remain poorly understood. This process is governed by thermodynamic, kinetic and transport factors, which makes it very difficult to control. Factors such as solution concentration, mixing regime, interface condition, vessel design, and transport profile can have a major impact on the size, number, and quality of crystals produced.

Classically, the solution crystal growth process can be explained in terms of thermo-

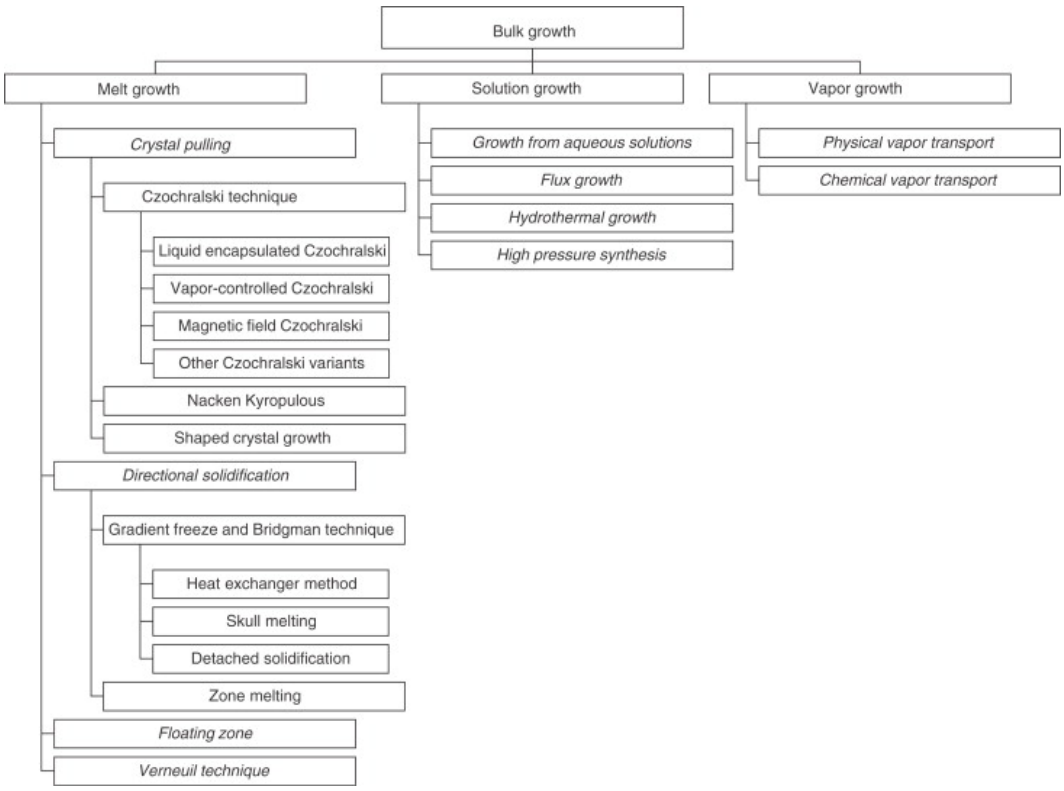

Figure 1.1: Crystal growth methods overview [88].

dynamic, kinetic and transport phenomena. Thermodynamics describes the driving force of crystallization. Kinetics accounts for the surface nucleation and step evolution. And transport takes into account the bulk and surface transport. In following sections, we will discuss how these phenomena affect solution crystal growth.

1.1.1 Thermodynamics in solution crystal growth

Thermodynamically, the formation of a crystal from liquid solution is a first-order phase transition. The driving force of this transition is the difference of chemical potential between the crystal phase and the liquid phase. Under equilibrium condition, the free energy is continuous across the phase boundary, or interface. However, crystal growth occurs in non-equilibrium states, in which crystal phase is surrounded by supersaturated solution. In this circumstance, the crystal phase is thermodynamically stable, while the solution phase is thermodynamically metastable. As a result, this chemical potential difference prompts the formation of solid crystal phase.

Thermodynamics is applied to explain the nucleation during crystal growth. Three-dimensional nucleation happens during the initial state of crystal growth, when nuclei form from liquid solution as origins for crystal growth; two-dimensional nucleation happens during the following crystal growth process, when two-dimensional nuclei form on the surfaces of these three-dimensional nuclei and serve as origins of new layers. Nucleation must occur when a solution is supersaturated, but not all nuclei are stable. The free energy per molecule is higher on the crystal surface than in crystal bulk. Molecules on the surface are less bonded to their neighbors, which makes the surface less stable. For nuclei, the effect of surface free energy is much greater than large crystals.

A important concept used to differentiate stable nuclei from unstable ones is called "critical size". Critical size is a threshold point. When a nucleus is smaller than the critical size, every molecule adding to the crystal surface or nuclei edge would boost the total free energy of the system, due to the increase of surface free energy contribution. Nuclei of this kind are more likely to dissolve, rather than grow. When a nucleus becomes larger than the critical size, the drop in bulk free energy during phase transition starts to dominant the process, and surface free energy becomes less important. At this point, the addition of a molecule to the system would lower the total free energy, and nucleus tends to grow bigger. As shown in Fig. 1.2, the total Gibbs free energy change per molecule $\triangle g$ can be determined as:

$$\triangle g = \triangle g_b + \triangle g_s, \tag{1.1}$$

where $\triangle g_b$ is the bulk change in Gibbs free energy from liquid to bulk crystal per molecule, and $\triangle g_s$ is the change in surface term. The total change of Gibbs free energy per molecules starts to decrease at $\partial \triangle g / \partial r = 0$. r value at this point is called critical radius, which demonstrates the nucleus critical size [151]. This size highly depends on solution supersaturation rate. If the supersaturation is high enough, the critical size can reduce to one molecule size, and the nucleation barrier vanishes [13].

1.1.2 Kinetics in solution crystal growth

In addition to thermodynamics, kinetics is important in the crystal growth process. Kinetics effects in crystal growth explain the crystal growth rate in terms of step movement velocity along crystal surfaces.

The growth rate of a crystal is determined by how fast new layers can be added to

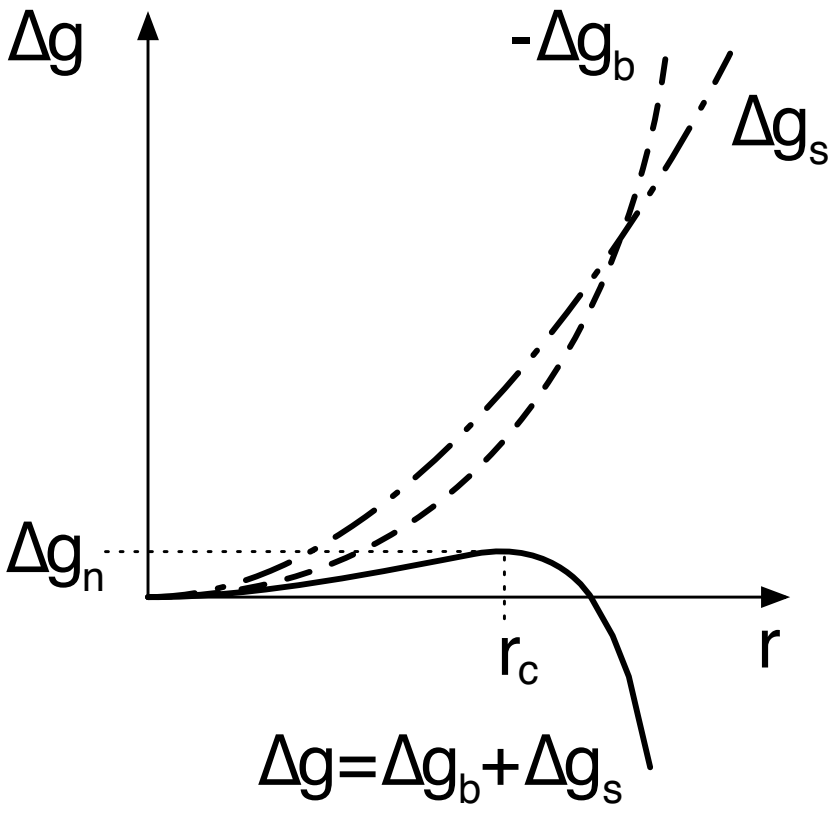

Figure 1.2: Critical radius of crystal growth can be defined by the change of Gibbs free energy. In this profile, $\triangle g_b$ is the bulk change in Gibbs free energy from liquid to bulk crystal per molecule, and $\triangle g_s$ is the change in surface term. The total change of Gibbs free energy per molecules starts to decrease at $\partial \triangle g / \partial r = 0$. r value at this point is called critical radius, which demonstrates the nucleus critical size [151]

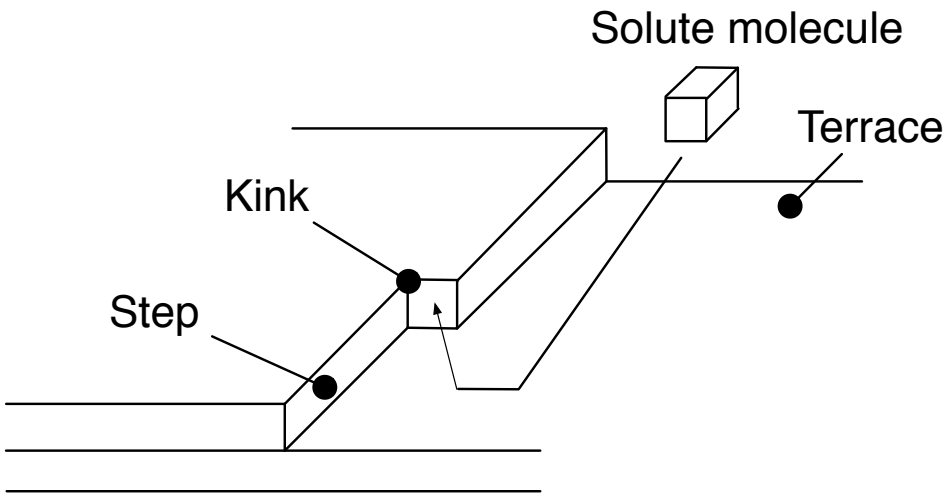

Figure 1.3: Schematic showing surface terrace, step and kink site on a crystal surface.

its surfaces. For a perfect crystal, the rate-limiting step is the two dimensional nucleation of a new layer. However, the experimentally observed crystal growth rate appears to be much faster than the calculated growth rate based on two dimensional nucleation theories. Therefore, step growth theory [22, 23, 48] was proposed to describe crystal growth as a process of step generation and movement. As showed in Fig. 1.3, a growing crystal surface consists of terraces and steps. A Terrace is the flat region and a step is the boundary between a raised terrace and a lower terrace. Steps are mostly incomplete and contains kink sites. Molecules attaching to kink sites have more bonds to neighboring molecules, and therefore is less likely to move compared to other free molecules on the surface [26–28]. During the growth, molecules on the terraces surface or along the step are not static, and they constantly attach and detach [140]. These molecules tend to diffuse to the more stable kink site. Consequently, steps elongate and the raised terraces expand, and the crystals grow as a result. Experimental evidence of this theory was observed in a large number of systems using atomic force microscopy(AFM) [149, 151].

1.1.3 Transport factors in solution crystal growth

Although kinetic theories about crystal growth are well established, it is not sufficient to explain the growth of crystals from liquid solution, because the transport effect is not taken into account. The transport of heat, mass, and momentum is important in crystal growth process. Flow in the solution phase is especially important for the heat and mass transport in growth systems. Solution crystal growth has suffered from a generally low growth rate, due to the slow diffusion of solute molecules through a liquid phase. For growth in high-temperature solutions (also known as flux growth), the growth rate is generally more than two orders of magnitude smaller than that in melt growth. As a result, the effect of mass transfer on solution crystal growth is nearly always significant. Such effects are known to slow the crystal growth rate and under certain circumstances can lead to morphological instabilities. It hence becames very important to identify how the mass transport, the surface attachment, or the heat transfer process would affect the crystal growth rate, and alleviate the limitations accordingly. More details about this topic will be further discussed in 1.2.2.

1.2 Numerical Modeling of Solution Crystal Growth

1.2.1 Traditional kinetics models

As stated in Section 1.1.1, crystal growth process is mostly kinetic control. Many crystal growth theories and models have been proposed to describe crystal growth kinetics.

One famous model formulated by Kossel [71] and Stranski [115] is the layer-by-layer model. In this model crystal growth rate is limited by two-dimensional nucleation, and growth will not occur unless the energy barrier required for two-dimensional nucleation is overcome. In experimental observations, however, crystals grow under a supersaturation level much lower than this nucleation requirement. This disagreement originates from the fact that most of the real crystals are imperfect, while Kossel and Stranski assumed the crystal surface to be perfect. Burton and Cabrera [22] suggested that a vicinal surface provides step source which corrects the difference between theory and experimental observations. Meanwhile, Frank [48] presented the kinematic wave theory which monitors the change of average step density, and noted that screw dislocation across the growing crystal surface would serve as a continuous step source. Based on these works, Burton, Cabrera, Frank postulated the Burton-Cabrera-Frank (BCF) mechanism [23]. This mechanism is also called the spiral layer-by-layer mechanism and is proposed to account for the real crystal growth. It was proved soon after its proposal by the observation of beryl crystal growth [55].

BCF theory represents the growth of crystals following a mechanism of step generation and movement. When a screw dislocation outcrops on a smooth interface, a step is created on the surface. The growth of the crystal starting from such a step advance like a spiral staircase around the dislocation as shown in Fig. 1.4. This process consists of three stages. First, the solute molecule in the bulk solution is transported to the crystal surface by diffusion and convection, and absorbed onto the crystal surface or desorbed back into the bulk solution. Second, the solute molecule diffuses on the crystal surface and incorporates into the growing step. During the incorporation, the kink site which formed along the growth step is preferred, because there are more dangling (unsaturated) bonds on this site than on the other sites. Finally, the heat of crystallization is removed from the crystal surface through the bulk crystal and the solution during the last stage of growth. Experimental evidence of BCF theory was obtained from a large number of crystal growth systems using high resolution microscopes, and one example is shown in Fig. 1.5.

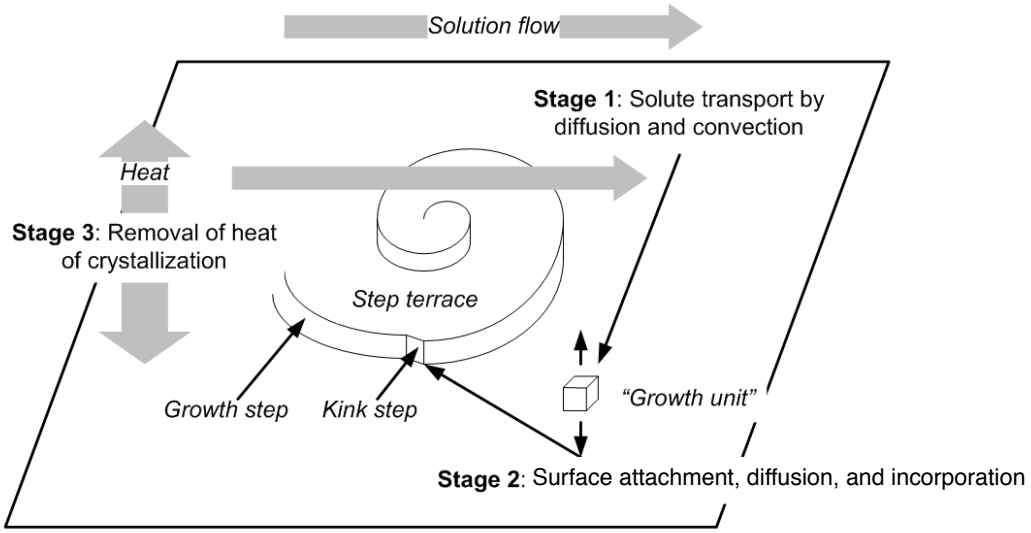

Figure 1.4: Mechanism of the BCF model

1.2.2 Continuum transport models

As mentioned in Section 1.1.3, kinetics alone is not sufficient to explain solution crystal growth process. Although the BCF mechanism of crystal growth is well established, we need to take transport effects into account to fully understand solution crystal growth.

To determine the optimum flow condition for solution crystal growth, Bordui and Motakef conducted a series of growth and flow visualization experiments, and pointed out the importance of the solution flow in controlling the solvent inclusion during the growth [18]. However, the details about mass transport in the liquid phase are not revealed, and the mechanism of crystal formation remains unclear. To better understand the transport effect in the liquid phase, numerical models are needed to provide a detailed picture of flows and mass transport in the supersaturation field.

Continuum transport models for solution crystal growth consider fluid dynamics of fluid flow and mass transfer of solute molecules in crystal growth systems. Fluid flow and mass transfer are simulated with the Navier-Stokes and convection diffusion equations as governing equations. Challenges to this modeling is due to three-dimensional geometries, which require enormous computational resources and forced convection that creates numerical instabilities. Previous continuum transport models [79, 89] have been limited to two-dimensional geometries and natural convection. With recent advances in numerical methods on massively parallel supercomputers [100, 120, 141], three-dimensional continuum transport models have become possible and have been successfully applied to study solution crystal growth systems [147,154]. In this thesis, we developed a three-dimensional fluid dynamics model to study the mass transport limitation during crystal growth in AFM fluid cell systems. This topic will be discussed in Chapter 2.

1.2.3 Step models

To understand the mechanism of solution crystal growth, many step growth mathematical models were developed. Classical spiral growth models developed by Chernov [28] and Glimer, Ghez, and Cabrera [53, 54] coupled solute transport with step advancing. However, these models analyzed only steady-state behavior with a constant terrace width, and cannot be applied to study dynamic behaviors during crystal growth. Rosenberger and coworkers developed a series of numerical models to analyze the dynamics of solution crystal growth and coupled the bulk solute transport with step growth on the crystal surface. However, many idealizations were assumed in these papers including arbitrary simplification of the step kinetic law. [80, 127, 128]. Derby *et al.* [73, 75] developed a numerical

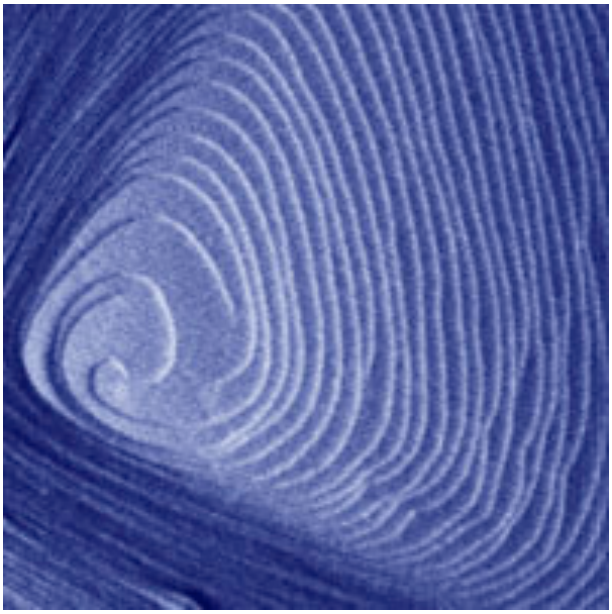

Figure 1.5: Evidence of spiral crystal growth around a screw dislocation in an $8 \times 8\,\mu m$ Atomic Force Microscope image during the growth of potassium dihydrogen phosphate [149].

model that not only accounted for both the bulk solute transport and the step growth on the crystal surface, but also analyzed the dynamics of solution crystal growth. However, this model assumed steps as one-dimensional lines and cannot be applied to study two-dimensional growth features. To extend this model to two-dimensional is hindered by the explicit tracking of all moving boundaries (steps) of complicate patterns. This difficulty, however, can be avoided by employing the phase-field method. In this thesis, a phase-field modeling studying solution crystal growth mechanism in ZnO nanowire growth system will be presented in Chapter 3.

1.3 Thesis Overview

In this thesis, analyses are presented on crystal growth processes. The goal of these analyses is to better understand and therefore control crystal growth. The work presented in this thesis is divided into three chapters.

In Chapter 2, a macro-scale fluid dynamics model is presented to study solution crystal growth systems in AFM fluid cells. A parallel, three-dimensional finite element model is applied to compute fluid flow and mass transfer during crystal growth in these fluid cells. This study is focused on the parametric sensitivity of crystal surface concentration, which characterizes different crystal growth conditions. How different crystal growth behaves in a fluid cell is studied, and the factors influencing crystal surface concentration are analyzed and compared. By studying these effects, we understand the mass transport limitation of solution crystal growth in AFM fluid cells and how to better interpret AFM measurements of crystal growth from liquid solution.

In Chapter 3, A fundamental theoretical model based on the phase-field method is presented. This model is applied to simulate nano-scale island growth and spiral step growth on crystal surfaces in a supersaturated liquid and is validated by comparison to experimental observation of zinc oxide nanowire growth. Results obtained by this work help to explain how experimental factors affect the crystal growth and crystal microstructures, and the correlation between island growth and spiral growth mechanisms.

In Chapter 4, we conclude this thesis with a summary of the work presented, and discuss future directions and questions for research that would extend our current studies.

Chapter 2

Macro-Scale FEM Study of an AFM Fluid Cell

Contents

2.1 Introduction of Crystal Growth in Atomic Force Microscope Fluid Cells

Atomic Force Microscope (AFM) is a very high-resolution type of scanning probe microscope, with demonstrated resolution of fractions of a nanometer. It was invented by Binnig, Quate and Gerber in 1986, and is one of the foremost tools for imaging, measuring and manipulating matter at the atomic scale [14,138]. The AFM has been widely used in scientific research since its invention, because this instrument can provide a true three-dimensional surface profile. And most importantly, the AFM does not require any special treatments to the samples, and most AFM modes can work perfectly in ambient air [60]. Moreover, with the invention of AFM fluid cell, now AFM can provide *in situ* measurement under liquid environment [87].

The AFM fluid cell is used by numerous research groups to image a variety of specimens, such as macro-biomolecules and crystals grown in solutions [58, 77, 83, 134]. All fluid cells, irrespective of their design, basically perform three functions: contain the sample, contain the liquid, and provide a stable optical path for the laser beam which is reflected off the back of the cantilever. A general layout of a liquid cell is shown in Fig. 2.1. This design eliminates the liquid-air interface and the movement of the liquid surface, which correspondingly reduces the laser beam refraction.

Fig. 2.2 shows a photograph of a real AFM fluid cell. By comparing it with a coin, we can tell that an AFM fluid cell is really small. In this cell, inlet and outlet channels are cut into the cell, and a shelf is centered at the top of the cell, along with a spring-loaded metal arm to secure the AFM cantilever and substrate in place. Crystal surfaces are imaged by securing seed crystals to a metal disk using a water-resistant cement.

Over the past ten years the AFM fluid cell has become a common tool for investigating the growth of crystal surfaces from solution. With the AFM, scientists are able to image the growth of crystal surfaces with atomic-scale resolution. Recently, the Digital Instrument AFM fluid cell has been used to measure the velocity of individual steps during solution crystal growth [58, 112]. These experiments have promoted our interest in understanding mass-transfer characteristics within the AFM fluid cell. Particularly, we are interested in understanding the impact of the geometry of the AFM fluid cell and the AFM tip on mass-transfer near the crystal surface being imaged. Moreover, the crystal growth kinetic coefficient β can be determined in AFM fluid cells. β is a materials property. It is very important because it is normally the parameter that characterizes different crystal growth.

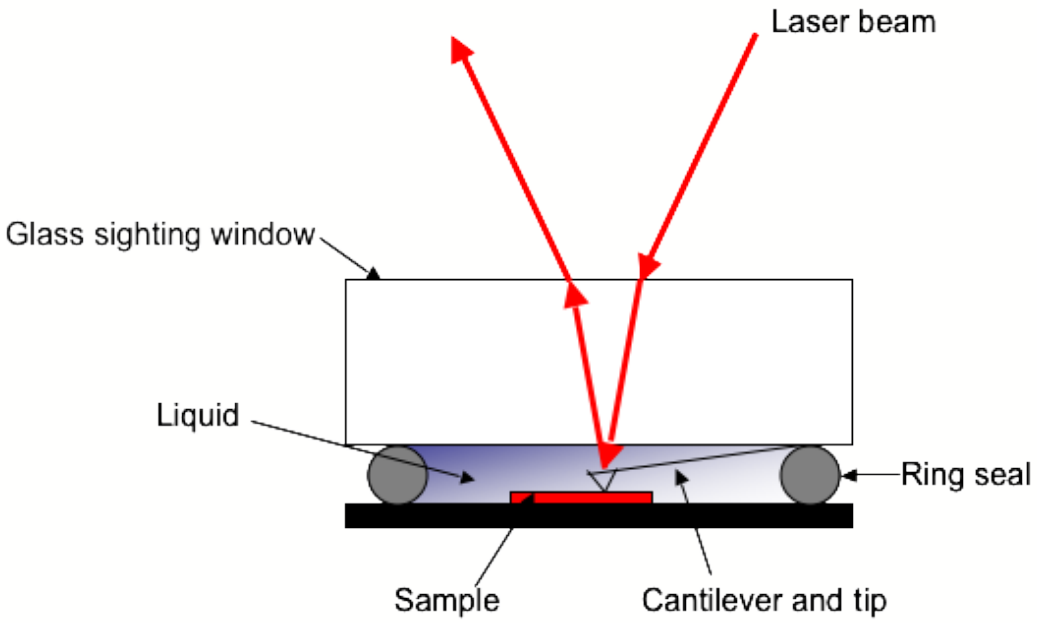

Figure 2.1: Schematic of an AFM fluid cell.

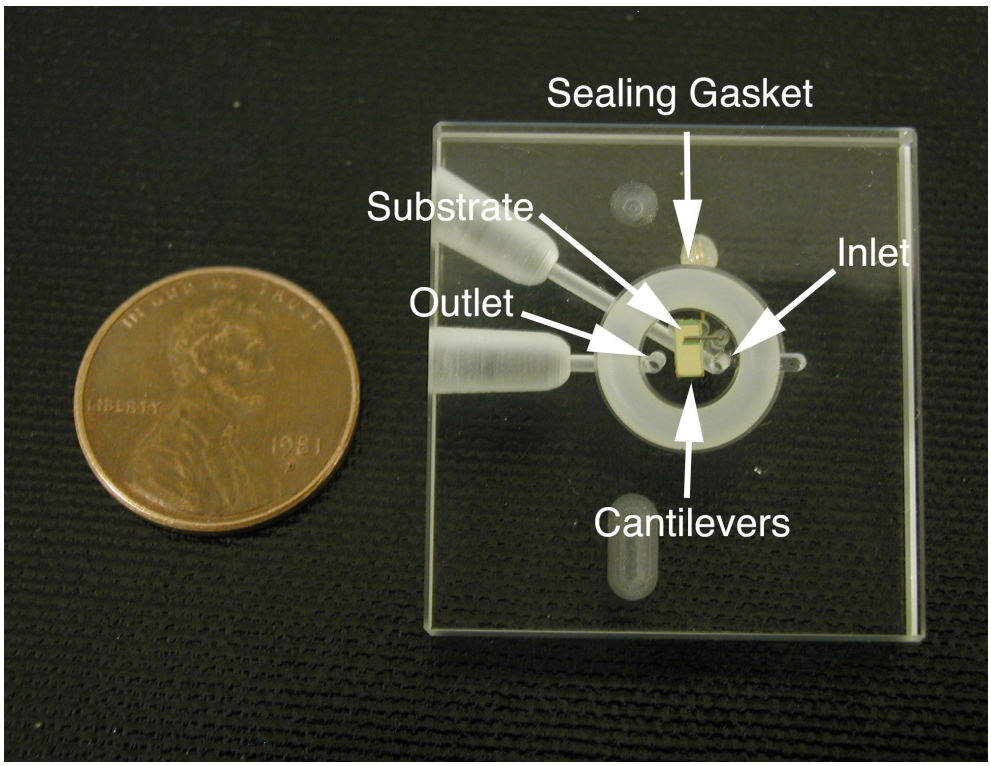

Figure 2.2: Photograph of a AFM fluid cell [50].

β represents the ratio between crystal growth rate and surface supersaturation.

$$v_c = \beta \sigma_s, \tag{2.1}$$

where v_c is the crystal growth rate and σ_s is the surface supersaturation. In AFM fluid cells, σ_s is unknown. In this case, people commonly assume it to be equal to the bulk supersaturation σ_0. However, experiments indicated mass transport limitation in AFM fluid cells has great impact on AFM measurements [65]. As shown in Fig. 2.3, with different mixing methods, the measured step velocity can differ much from each other. Crystals grow in quiescent solution show lowest step velocity. Pre-mixed flow helps improve crystal growth and step velocity of crystals is higher compared to the quiescent case. Among all cases, crystals grow in in-line missed solution show the highest step velocity. This difference in step velocity indicates the existence of mass transport limitation in AFM fluid cells.

Additionally, as shown in Fig. 2.3, the materials property β, which should maintain constant, is changing under different experiment conditions. This occurs because the as-

sumption that surface supersaturation equals to bulk supersaturation needs to be adjusted. As a result, there exists a need to understand the limitations associated with mass transport of solute molecules, and to adjust this assumption accordingly.

However, despite the direct visualization of crystal growth enabled by in situ AFM, there are currently no independent means of determining the flow conditions present during AFM measurement of solution crystal growth. An experimental mass-transfer characterization of this system would be difficult to conduct due to the small dimension of the AFM fluid cell, and would likely disturb the natural processes within the system. Although direct measurement is not possible, numerical studies can provide an accurate method to investigate mass and momentum transfer in solution growth systems. Computational models can complement experimental observation by providing a detailed profile of flows and mass transfer in the AFM system, particularly near the measurement tip.

During the crystal growth in the AFM fluid cell system, control over bulk supersaturation can be achieved by maintaining the temperature of the solution and changing the solute content of the reservoir, or by varying the temperature for fixed solute content [150]. However, control over bulk supersaturation does not necessarily ensure control over supersaturation near the crystal surface, if a concentration boundary layer exists. The conditions for the existence of mass and momentum boundary layers have been well studied and can be related to dimensionless parameters particular to the geometry of the system and the physical characteristics of the fluid [94, 106].

If the solution used in the fluid cell is assumed to be a dilute binary mixture, the species conservation equation for a binary mixture can be employed to gain basic insight on concentration boundary layers within the cell. A key parameter in any forced convection mass transfer problem is the Peclet number (Pe), which describes the importance of convective relative to diffusive mass transfer.

$$Pe \equiv \frac{UL}{D_i} \tag{2.2}$$

In the above equation for the Peclet number, U is the characteristic velocity of the system, L is the characteristic length, and D_i is the diffusivity of species i in solution. The Peclet number arises from the nondimensionalization of the species conservation equation, and is capable of providing useful mass transfer information only if meaningful characteristic parameters are chosen for the nondimensionalization. A more advanced discussion about the Peclet number will be included in Section 2.2. For the AFM fluid cell, the characteristic velocity of the system can be chosen as the maximum fluid velocity at the cell inlet, and the characteristic length can be chosen as the size of the crystal. With

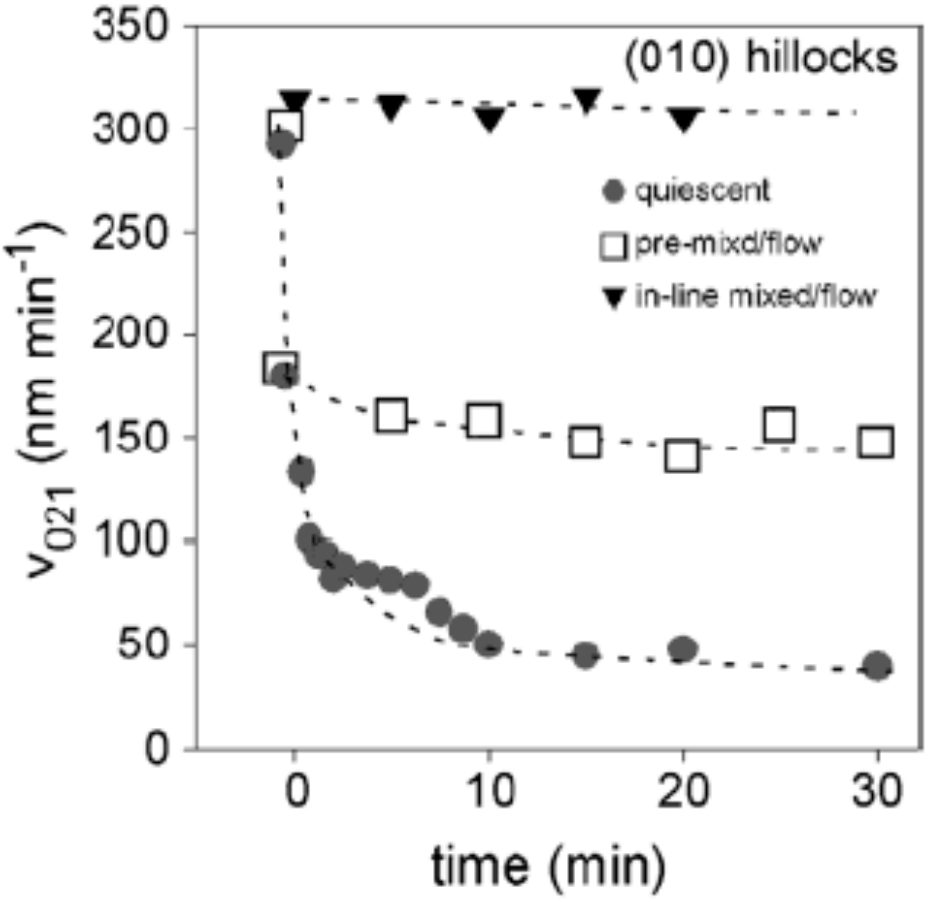

Figure 2.3: Step velocity varies with different mixing method. This plot shows how step velocity change with time while crystals grow in quiescent solution (circle line), in pre-mixed solution(square line), and in in-line mixed solution(triangle line). Among three cases, step velocity of crystals grow in in-line mixed solution is the highest [65].

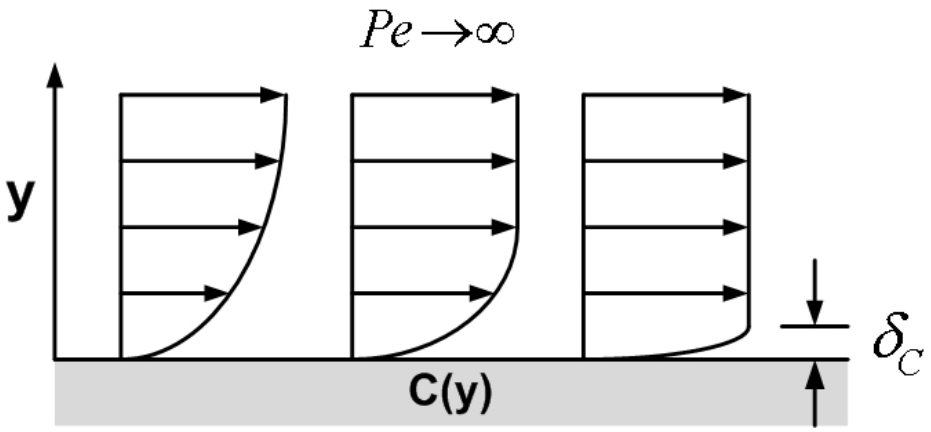

Figure 2.4: Concentration profile C versus height y near crystal surface for increasing Peclet number. The boundary layer is represented by δ_C

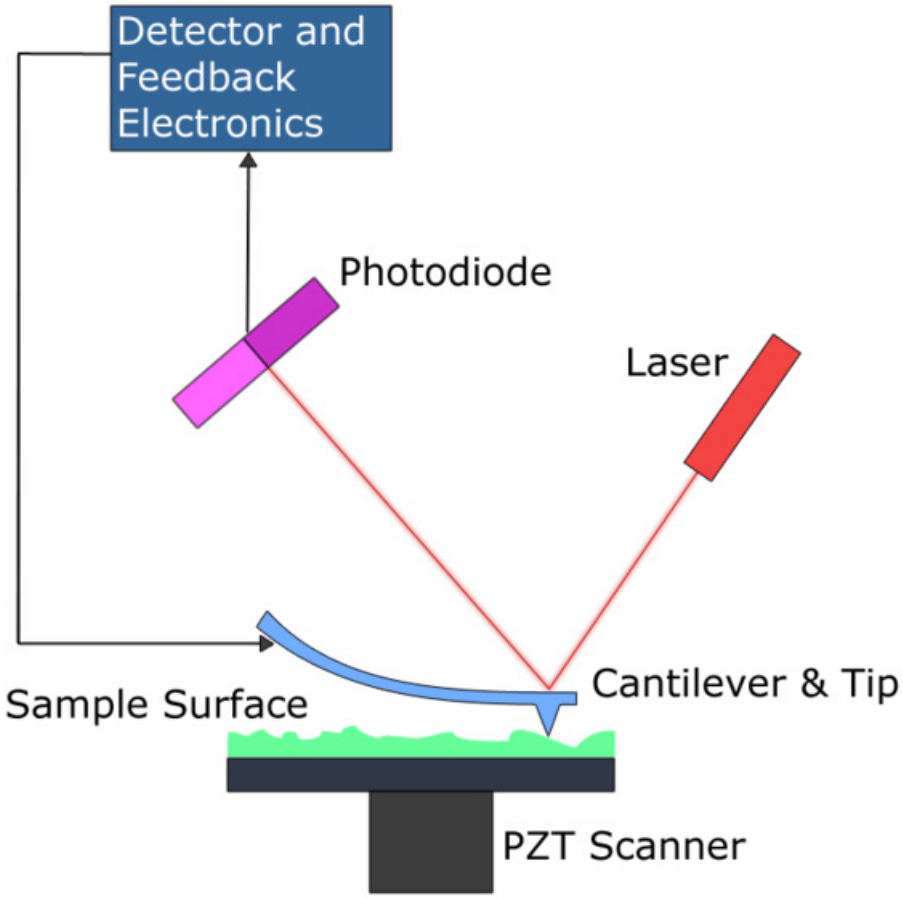

Figure 2.5: Schematic representation of the AFM.

these choices, calculation of the Peclet number for average experimental flow rates yields $Pe = 10^6$. The large Peclet number for the system indicates that concentration boundary layer phenomena within the cell will be important, ultimately affecting the supersaturation distribution on the crystal surface. The general correlation between the concentration profile near the crystal surface and the Peclet number is shown in Fig. 2.4. We will conduct numerical studies to determine the nature of the concentration boundary layer near the crystal surface, and the impact of changes in bulk fluid velocity and concentration on the supersaturation field near the AFM tip.

2.1.1 Atomic force microscope apparatus

The AFM images specimen surface by scanning them with a sharp probe and measuring changes in the magnitude of the distance between the probe and these surfaces. The schematic of the AFM in Fig. 2.5 illustrates the main features of an AFM. There are three main functional parts of the AFM including probe system, scanning system, and detection system.

The first and most important part of the AFM is the probe system, which includes a cantilever and a probe. Fig. 2.6 shows the main feature of an AFM probe system. Generally speaking, the tip height ranges from $2.5\mu m$ to $3.5\mu m$. The thickness t of the cantilever ranges from $0.4\mu m$ to $0.7\mu m$. The Length L for the large triangular cantilever ranges from $180\mu m$ to $196\mu m$, and the L for the small cantilever ranges from $100\mu m$ to $115\mu m$. As can be seen, the probe is mounted at the end of the cantilever. The probe has a microfabricated, extremely sharp tip, and the sharpness of this tip determines the resolution of this microscope [15]. AFM tips produced by current lithographic techniques have spatial resolution controllable down to $10nm$ [72]. Typical AFM tips have a radius around $200\mathring{A}$ and are made from oxide-sharpened silicon nitride (Si_3N_4).

The cantilever on which this probe is mounted typically has a very low spring constant ranging from $0.01-0.10N/m$. This allows the probe to move vertically with the fluctuation of the specimen surface and enables the AFM to control the force between the tip and the sample with great precision [87]. When the AFM tip moves close to contact with a sample surface, interatomic force between the tip and the surface causes the cantilever to deflect as illustrated in Fig. 2.7 . The cantilever typically has two basic geometries, which are triangular and rectangular geometry. The triangular geometry seen in Fig. 2.6 (b) is designed to minimize torsional motion and is the choice for pure topographical imaging. This kind of cantilevers is what we will mainly deal with in this research project. However, if

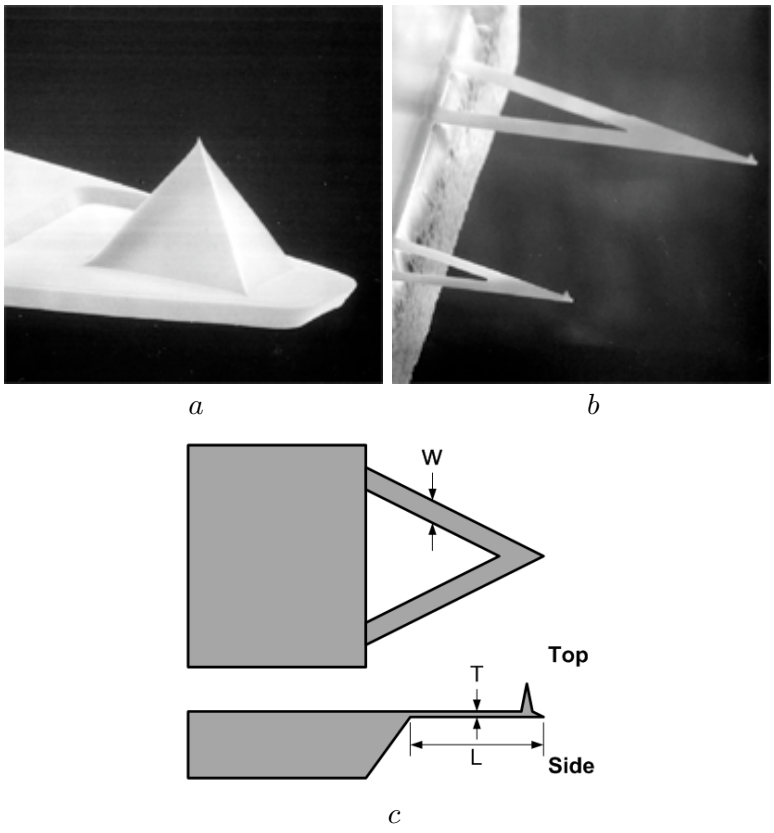

Figure 2.6: (a) Scanning electron microscope (SEM) picture of an AFM tip. (b) SEM picture of an AFM probe system. (c) Schematic diagram of an AFM probe system. (Veeco product picture)

lateral force caused by frictional properties of a sample is desired, the rectangular geometry which has a greater degree of rotational freedom and is sensitive to this force, would be the better choice [1].

The second feature of the AFM is the scanning system. Modern AFM scanning systems have two basic types of scanning mechanism. They scan either the sample or the tip. Both mechanisms rely upon piezoelectric transducers. This is because the nano-scale AFM resolution requires an accurate positioning. This positioning is achieved by applying the reverse piezoelectric effect of the piezoelectric transducers [118] . This effect means that if the opposite face of a piezoelectric crystal is subjected to a potential difference, the piezoelectric material experiences phase transition, and the crystal changes shape [122]. As a result, the AFM scanner, which consists of piezoelectric ceramics, can expand with the potential difference. Most importantly, this motion is incredibly reproducible, accurate enough for atomic scale movement, and easy to be controlled by electric signals. These features make the piezoelectric transducer a perfect choice for the AFM scanning system.

The final part of the AFM is the detection mechanism, which is used to measure the motion of the tip. Several different mechanisms are applied to the AFM detection system, such as the contact mode, the tapping mode, and noncontact mode. The most widespread method for detecting is the optical beam deflection method [2, 86]. This mechanism is illustrated in Fig. 2.5. In this method, a laser beam is focused onto the end of the cantilever, which is directly over the tip, and then reflects off onto a photodiode detector. This detector is split into four segments to increase the accuracy in the modern technique. During the scanning, the tip moves in response to the sample topography, and these movements change the angle of the reflected laser beam. As a result, the laser spot on the photodiode moves, producing changes in intensity in each quadrant of this photodiode. These changes are then read and transformed to the z-direction deflection of the tip, and this deflection represents the surface "height" at that scanning point [103]. This method is simple but both very sensitive and accurate enough for the atomic scale measurement. Furthermore, it is the mechanism mostly used for liquid based AFM imaging.

In the remainder of this chapter, we represent a three-dimensional fluid dynamics model to study the fluid flow and mass transport limitation during crystal growth in these AFM fluid cells.

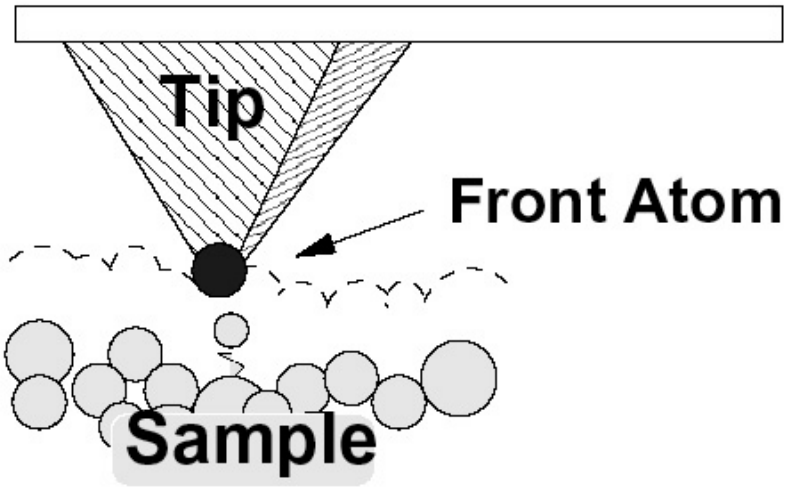

Figure 2.7: Schematic of an AFM tip-sample interaction. The tip follows the contour indicated by the dashed line above the sample to maintain constant force between the tip and the sample [14]

.

2.1.2 Previous work on AFM fluid cell

Gratz and Hansma initiated the *in situ* AFM study of a growing crystal in 1991 [150]. Since then, AFM has become a widely used tool for studying crystal growth and dissolving in solution. Lately, AFM was used to study the steady-state kinetics in solution crystal growth. In this study, solute concentration was assumed to be a constant value throughout the fluid cell. This assumption however, is not true. Due to the mass transfer limitation, solute concentration near the growing crystal surface is lower than the bulk concentration. Mass transfer study of this system can help understanding the true supersaturation condition. Additionally, other crystal growth features, such as dislocation source activity, two and three-dimensional nucleation, and impurity effects [150] were also studied using AFM fluid cells. A comprehansive understanding of these phenomena, however, requires knowledge of fluid flow and mass transfer characteristics in this system.

Schmidt and Alkive [108] developed a series of experiments to verify the impact of fluid flow on AFM fluid cell imaging. Their experimental results at atomic scale indicated that atomic spacing of an image was not affected by the fluid-flow environment. However, when flow rate exceeds $0.08cm^3/s$, excessive noise would prevent successful imaging at the atomic scale. Schmidt and Alkive stated that this noise resulted from the shear stress acting on the AFM tip.

Coles *et al.* studied the hydrodynamics of AFM fluid cell for interfacial kinetics measurement [30]. The fluid cell they worked with was based on the Topometrix liquid immersion cell, with the addition of an inlet tube. A two-dimensional model of this modified AFM fluid cell using FIDAP program was developed, which is a finite-element method based fluid dynamics program. In one of their studies they simulated the flow pattern with a flow rate of $0.0014cm^3/s$, and the contour plot is shown in Fig. 2.8. As we can see, the flow pattern is complex. Coles *et al.* indicated that the simulated dissolution rate was consistent with the experimental data. If the flow profiles within the fluid cell were known, a flux boundary condition could be set at the crystal surface to compare a theoretical dissolution mechanism with experimental observations.

Further work of the hydrodynamics of AFM fluid cells was done by the Compton group [31, 61] . A two-dimensional model of hydrodynamics was constructed to study the dissolution of different systems, such as calcite system and salicylic acid and calcium carbonate system. These studies showed disagreement between the numerical solution and experimental data. The limitation of the two-dimensional model is suspected to be one reason of this disagreement.

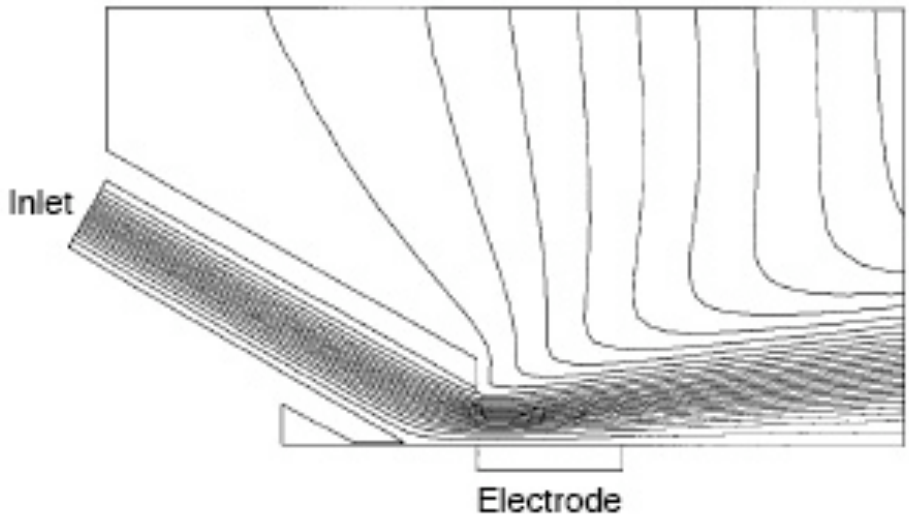

Figure 2.8: The two-dimensional cross-section of solution modelled with FIDAP, showing jet and electrode positions, with streamline contours for a flow rate of 0.0014 $ml\ s^{-1}$ [30].

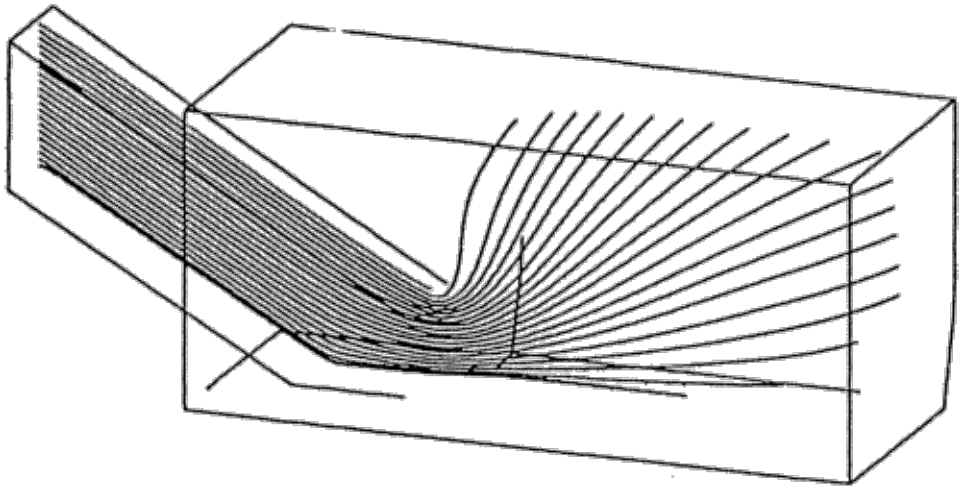

Figure 2.9: Schematic view of the simulated portion of the AFM cell, showing the jet tube, at the left, and particle path trajectories as the solution spreads out into the cell. The sample surface is at the bottom. [139].

In 2000, the Compton group completed a three-dimensional model of AFM fluid cell system using the FIDAP 7.62 program [139]. A parabolic flow profile was set at the flow inlet, a zero-gradient boundary condition was set at the free boundaries of the box, and a no-slip boundary condition was imposed at the bottom surface. Fig. 2.9 shows a simulated particle path trajectory at a fairly low flow rate. At higher flow rate, the jet of solution flow would move closely along the sample surface with a smaller degree of spreading. It was concluded that this three-dimensional finite element hydrodynamics simulation accurately calculated the dissolution flux of salicylic acid in this modified AFM fluid cell system, and this solution was accurate over a wider range of flow rates than the two-dimensional model.

The work done by Compton *et al.* showed the effect of fluid flow inside a modified AFM fluid cell. Compton's finite element model which matched the experimental data is clearly a progress. This work developed the context for a better characterization of the mass and momentum transfer inside AFM fluid cells. This feature is very important for crystal growth studies using AFM fluid cells. However, Compto's model has its own limitations. The AFM fluid cell system they worked with is a simplified geometry. A real geometry of the modern AFM fluid cell is needed for more accurate simulation.

Gasperino *et al.* formulated a three-dimensional finite element model to analyze incompressible flow hydrodynamics and solute transport in a modern Digital Instruments (DI) AFM fluid cell (part 150-000-002). Results from this work revealed significant interactions

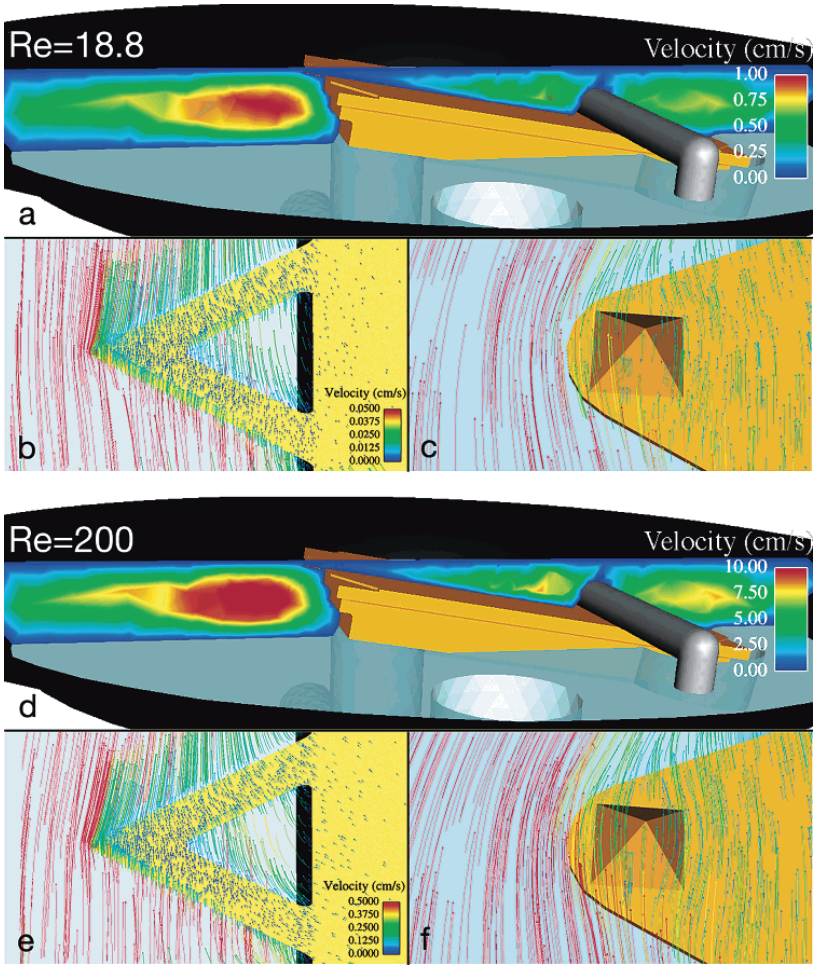

Figure 2.10: (a and d) Velocity magnitude from the computational simulations are projected on a clip plane of the global domain of the fluid cell that intersects the larger of the two AFM cantilevers. (b and e) Pathline portraits of flow past the sample-scanning side of the large AFM cantilever. (c and f) Pathline portraits of flow past the scanning tip attached to the large cantilever. Pathlines for the bottom two visualizations are colored by the same velocity scale. Image groups are for Reynolds number equal to (a,b,c) 18.8 and (d,e,f) 200. [50]

between fluid flow and the complicated system geometry. Gasperino *et al.* revealed that under operating conditions much of the flows was directed away from measurement regions, and solute molecules consumed by crystal growth could not be replenished completely by convective mass transport in these regions.

Gasperino *et al.* applied this finite element model to simulate the growth of calcium oxalate monohydrate (COM) crystal. The rates of crystal growth on specific crystal faces have been measured in this fluid cell [50]. Fig. 2.10 shows their results about the fluid flow under the conditions of $Re = 18.8$ and $Re = 200$, where $Re = UL\rho/\mu$. They found that the flow at $Re = 18.8$ is much more viscous in nature than the flow at $Re = 200$, with pathlines that are uniformly spaced and aligned smoothly with the system geometry. The faster flow at $Re = 200$ is affected more strongly by inertia. The pathline does not spread evenly across the cell; instead, there are areas of dead space that are passed by the surrounding flow.

Mass transfer effect was also studied in this paper. As showed in Fig. 2.11, solute depletion was observed indicating mass transfer limitation in this fluid cell system associated with shielding by the cantilever and tip. Gasperino *et al.* also observed that although the depletion region beneath the cantilever is apparent for all flow rates, the depletion layer around the crystal surface is almost symmetrical at low flow rate, while the depletion layer shifts along the crystal surface in the direction of flow as flow rates increased.

The work of Gasperino *et al.* is a big step toward a clearer understanding of how the continuum transport affects the crystal growth during the imaging in AFM fluid cells. However, this work is focused on COM crystal growth system. Since AFM is wildly used in crystal growth measurements, more general study about other crystal growth systems is needed to fully understand the mass transport limitation and its impact on crystal growth in AFM fluid cells. To extend Gasperino's work and to comprehend the understanding of hydrodynamics and mass transfer impact in this AFM fluid cell system, more work needs to be done.

2.2 Model Formulation

In this section, we introduce the governing equations in our simulation system, and the methods used to solve the governing equations are presented. These methods include the finite element method (FEM) with the Galerkin/Least-Squares (GLS) formulation, method of the finite element mesh generation, and numerical solvers with which we solve the equations.

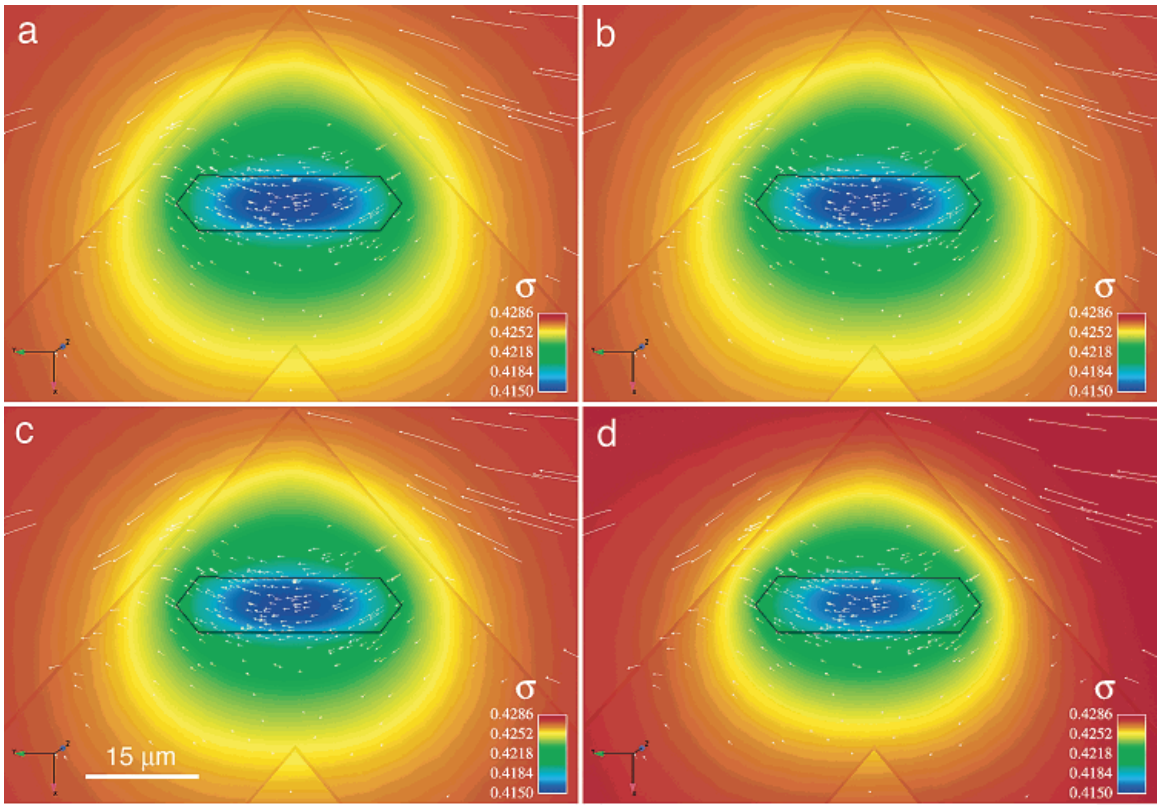

Figure 2.11: Visualizations of the computed supersaturation, σ, along the plane containing the growing crystals, below the large cantilever, for Reynolds number equal to (a) 0.02, (b) 0.2, (c) 18.8, and (d) 100. The crystal (outlined in black) is located directly under the large cantilever (semi-transparent). Pathlines (colored white) lying in a plane between the cantilever and the crystal surface are included. Flow is from right to left in all images. [50]

2.2.1 Governing equations

In this section, we introduce the equations describing mass and momentum transport in AFM fluid cells. To construct a mathematical model for this system, we assume that (a) the fluid flowing through the cell is incompressible, which is a reasonable approximation for liquid, (b) the system is isothermal (at 25 °C), so that buoyant flow effect can be ignored, (c) the transport properties are independent of temperature and composition, (d) the scan rate is slow and its amplitude is small compared to the fluid flow through the system and the dimensions of the system, allowing stage movement effect to be ignored, and (e) the mass transfer can be described by the convection and diffusion of a dilute single species (the solute) dissolved in water (the solvent). We also invoke a quasi-steady-state assumption for flow and mass transfer. The characteristic time for convective transport is $L/U \sim O(0.1s)$, where L is the thickness of the fluid cell and U is the centerline velocity at the fluid cell inlet. The time scale for diffusive transport near the crystal is $L_c^2/D \sim O(1s)$, where L_c is the length of a growing crystal and D is the diffusion coefficient for the solute. As the characteristic time for normal crystal growth is on the order of $1h$, these conditions would justify the use of the quasi-steady-state assumption. With this assumption, the partial derivatives with respect to time in the governing equations go to zero, leaving us with a boundary value problem (BVP). If the time-dependent terms are left in the equations, then we have an initial value boundary problem (IBVP). A detailed derivation of the governing transport equations from the first principle can be found in detail in published papers [16, 34].

Momentum equations and boundary conditions

Momentum conservation in the AFM fluid cell domain is described by the Navier-Stokes (NS) equations for incompressible flow with the continuity constraint. If we choose the AFM fluid cell as a stationary frame of reference and neglect body forces, the differential equation of change of momentum per unit volume (p.u.v.) is given by:

$$(\rho \mathbf{v} \cdot \boldsymbol{\nabla} \mathbf{v}) \quad = \quad \boldsymbol{\nabla} \cdot \underline{\underline{\mathbf{T}}} \tag{2.3}$$

where v is the velocity (with cartesian coordinates v_x, v_y, v_z), p is the dynamic pressure, and $\underline{\underline{\mathbf{I}}}$ is the identity tensor. The first term in Equation 2.3 represents the rate of momentum accumulation per unit volume , the second term shows the net momentum inflow per unit

volume by convection, the third term illustrates the viscous force per unit volume, and the last term describes the force per unit volume due to pressure field. The corresponding continuity equation is:

$$\boldsymbol{\nabla} \cdot \mathbf{v} = 0 \tag{2.4}$$

We rewrite the NS equations in a dimensionless form, which is useful both physically and computationally, and the non-dimensionalized NS equations can be written as:

$$Re(\partial \bar{\mathbf{v}} + \bar{\mathbf{v}} \cdot \bar{\boldsymbol{\nabla}} \bar{\mathbf{v}}) = \bar{\boldsymbol{\nabla}} \cdot (\bar{\boldsymbol{\nabla}} \bar{\mathbf{v}} + (\bar{\boldsymbol{\nabla}} \bar{\mathbf{v}})^T) - (\frac{L}{\mu U}) \bar{\boldsymbol{\nabla}} \bar{p} \underline{\underline{\mathbf{I}}} \tag{2.5}$$

$$\bar{\boldsymbol{\nabla}} \cdot \bar{\mathbf{v}} = 0 \tag{2.6}$$

$$\tag{2.7}$$

where $\bar{\mathbf{v}}$ is the velocity scaled by the centerline velocity at the fluid cell inlet U, $\bar{\boldsymbol{\nabla}}$ is scaled by the characteristic length L which is the crystal size in our model, $\bar{t}$ is the time scaled by the convective time $\frac{L}{U}$, $\bar{p}$ is pressure scaled by viscous pressure $\frac{\mu U}{L}$. And Re is the Reynolds number and is defined as:

$$Re = \frac{UL\rho}{\mu} \tag{2.8}$$

$$\tag{2.9}$$

To complete the NS equations, appropriate boundary conditions for the AFM fluid cell domain are applied. The no-slip and no-penetration boundary condition is applied along all the solid surfaces in the AFM fluid cell and the growing crystal surface. Because the stationary fluid cell is taken as the frame of reference, the no-slip and no-penetration boundary conditions simplify to

$$\bar{\mathbf{v}} = 0 \tag{2.10}$$

which is known as a Dirichlet boundary condition, or essential boundary condition.

A Dirichlet boundary condition is applied at the inlet of the fluid cell as a parabolic velocity profile [16]:

$$\mathbf{n} \cdot \mathbf{v}(r) = v_{max} \left[1 - \left(\frac{r}{R_0} \right)^2 \right] \tag{2.11}$$

where $\mathbf{n}$ is the normal vector to the cross section of the inlet. The centerline velocity equals to the maximum velocity (v_{max}) of the system. The implementation of this boundary condition assumes that flow is fully developed at the fluid inlet. The final boundary condition for the NS equations is applied at the fluid outlet, and is known as an open boundary condition. At the cross section of the fluid cell outlet, an outflow condition is applied:

$$\mathbf{n} \cdot \bar{\boldsymbol{\nabla}} \bar{\mathbf{v}} = 0 \tag{2.12}$$

which represents a well-developed flow downstream of the computational domain.

Species equations and boundary conditions

The material balance on an arbitrary species in a dilute binary mixture can be expressed in the following mass conservation equation:

$$\mathbf{v} \cdot \boldsymbol{\nabla} \mathbf{C} \;=\; D \boldsymbol{\nabla}^2 \mathbf{C}, \tag{2.13}$$

where C is the concentration of the dilute species, and D is the diffusivity of the molecules in water at 25 °C. The first term of Equation 2.13 represents the net species inflow per unit volume by convection, and the last term is the net species inflow per unit volume by diffusion. Equation 2.13 is known as the convective-diffusion equation, and describes species transport in a finite volume. The term on the right hand side of Equation 2.13 is based on Fick's law for binary diffusion for a dilute species, and should be a valid approximation for our model.

For the same reason as we scaled the NS equations, we rewrite Equation 2.13 in a non-dimensional form. Relative supersaturation, σ, is used to non-dimensionalize solute concentration C, and σ can be defined as:

$$\sigma \;=\; \frac{C - C_{eq}}{C_{eq}} \tag{2.14}$$

where C_{eq} is the equilibrium mass fraction of solute at a given temperature and pressure, and C is the local concentration of solute. In this case, the mass conservation equation can be written as:

$$Pe(\bar{\mathbf{v}} \cdot \bar{\boldsymbol{\nabla}}\sigma) = \bar{\boldsymbol{\nabla}}^2\sigma \tag{2.15}$$

where Sc is the Schmidt number and Pe is the Péclet number, and they are defined as:

$$Pe = \frac{UL}{D} \tag{2.16}$$

Boundary conditions for Equation 2.15 are applied at the crystal surfaces, inlet and other boundary surfaces.

At the crystal surfaces, the crystal growth rate was assumed to be linearly depend on supersaturation. If we further assume that the solvent, water, is rejected at the interface directly at the crystal surface, Westphal and Rosenberger [137] have shown that the interfacial mass flux of solute to the crystal surface ($\mathbf{N}$) is given by

$$\mathbf{N} = -\frac{\rho D}{1-C}\boldsymbol{\nabla}C \tag{2.17}$$

where ρ is the density of the solvent. A solute mass balance at the interface yields:

$$(-\mathbf{n}) \cdot \mathbf{N} = \rho_c V_f \tag{2.18}$$

where ρ_c is the density of the crystal, V_f is he normal growth rate of the crystal interface, and $\mathbf{n}$ represents the outward unit vector normal to the interface. The left part of Equation 2.18 represents the total flux of solute to the interface. If we define V_f with the kinetic data from Gvozdev [58], and assume a linear dependence on supersaturation, σ, over the crystal surfaces, then we have:

$$V_f = \beta\sigma \tag{2.19}$$

In this equation, β is the crystal growth kinetic coefficient, and σ is defined same as

Equation 2.14. This coefficient is an important material physical property in our studies. As shown in Equation 2.19, β is the proportionality constant between crystal growth velocity and supersaturation. The magnitude of β represents the ease of crystal growth process under certain circumstances and is of fundamental importance.

Combining Equations 2.18 with Equations 2.17 and 2.19, we derive the following equation to represent the supersaturation field at the crystal surfaces:

$$\mathbf{n} \cdot \boldsymbol{\nabla} C \;=\; \frac{\rho_c V_f}{\rho D}(1 - C) \tag{2.20}$$

We rearrange the above equation and get:

$$\mathbf{n} \cdot \bar{\boldsymbol{\nabla}} \sigma \;=\; \frac{L \rho_c \beta \sigma}{D C_{eq}}(1 - \frac{C_{eq}}{\rho}(\sigma + 1)) \tag{2.21}$$

Equation 2.21 is the boundary condition we apply at the growing crystal surface. The main purpose of incorporating the crystal surfaces with this boundary condition is to get quantitatively meaningful concentration gradients near these surfaces, and to check the effects of these gradients on the continuum mass transport processes.

In Equation 2.21, we combine the first dimensionless term on the right hand side and named it the modified Damköhler Number Da,

$$Da \;=\; \frac{L \rho_c \beta}{D C_{eq}}, \tag{2.22}$$

and Equation 2.21 becomes:

$$\mathbf{n} \cdot \bar{\boldsymbol{\nabla}} \sigma \;=\; Da \sigma (1 - \frac{C_{eq}}{\rho}(\sigma + 1)). \tag{2.23}$$

Da in our case represents the ratio between crystal growth rate and the diffusive mass transport rate. This parameter is of great importance in our research. We show in Section 2.3 that this is one of the parameters that has greatest effect on surface concentration.

At the inlet to the fluid cell, a Dirichlet boundary condition is imposed as:

$$\sigma = \sigma_0 \tag{2.24}$$

where σ_0 is a constant value of the relative supersaturation at the inlet.

At the flow outlet, the condition

$$\mathbf{n} \cdot \bar{\boldsymbol{\nabla}} \sigma = 0 \tag{2.25}$$

is applied. This condition describes a well-developed concentration field exiting the computational domain. The same mathematical condition is applied to the other surfaces in this system, representing a no-flux condition for the solute.

2.2.2 Implementation of finite element method

The governing equations and associated boundary conditions are solved using a Galerkin mixed-order finite element method employing a higher-order, quadratic representation of the velocity and supersaturation fields with a linear, discontinuous basis for pressure. This basis set is a three-dimensional adaptation of the Crouzeix–Raviart P_2^+–P_{-1} element [12,32], containing 15 nodes, 45 velocity degrees of freedom, 15 concentration degrees of freedom, and 4 pressure degrees of freedom per tetrahedral element. Our approach employs Newton's method with an iterative linear solver and is implemented using MPI protocols on parallel computers [38, 74]. Several preconditioning methods are employed with GMRES via PETSc [9] for the linear solver.

Computations were carried out on a mesh containing 250,517 elements. Details of this mesh is provided in the "Finite Element Mesh" section. This mesh, comprising over 2 million unknowns, required approximately 10 minutes of computation time per solution on an 8-processor Linux cluster at the University of Minnesota Supercomputing Institute. With the higher-order basis set, these computations are significantly more accurate than our prior studies [50], which yielded a global mass flux error of less than 0.2% and were also validated via flow visualization experiments in the AFM cell.

Finite element method overview

Equations governing macroscopic transport are nonlinear, coupled, partial differential equations (PDE). Due to the complexity of these equations, it is not possible to solve them analytically except for simple geometries and boundary conditions. Therefore, they must be solved numerically. The computational domain is spatially discretized, and partitioned into small elements. These PDEs are spatially discretized based on the domain discretization.

For this purpose, we employ the finite element method (FEM), which has been applied successfully to previous three-dimensional continuum transport models for melt and solution growth systems [37, 102, 142]. FEM offers several advantages over other discretization techniques, such as the finite difference method, such as easy accommodation of complex three-dimensional geometries and facile implementation of different types of boundary conditions. In addition, the data structure generated by FEM is well suited to be implemented on a parallel supercomputer.

The first step in the finite element formulation of a problem is the discretization of the computational domain into smaller subdomains, known as finite elements. These elements share points in the computational domain called nodes. The second step includes the approximation of the solution to the problem in each element by a linear combination of Lagrangian interpolation polynomials, also known as basis functions. A useful characteristic of Lagrangian basis functions is that they can be chosen to equal to unity at the nodes where they are defined, and zero at all other nodes in the domain. The coefficient in the linear combination is the nodal value of the solution on that element.

The next step is to reformulate those governing equations into their *weak forms*. The term "weak" refers to the reduced continuity of the basis needed for solution of the PDE, which is required to be only once-differentiable for a second-order PDE. The weak form also allows for easy application of natural boundary conditions. When the approximations for the field variables are substituted into the weak form of the governing equations and integrated, a set of algebraic equations are obtained for the unknown nodal variables. To find a continuous solution to the governing PDEs over the entire domain, basis functions are used to interpolate between nodes. This set of equations is then assembled into vector form to obtain global set of equations involving all unknowns in the problem. The accuracy of the numerical solution can be improved by increasing the degree of the basis functions or by increasing the number of nodes used in the discretization.

Finite element mesh

One of the key ideas of the FEM is that we divide the given computational domain into smaller subdomains and approximate the unknown variables by a linear combination of Lagrangian interpolation functions (also called basis functions) that are defined locally over each subdomain. These subdomains, often in form of cubes or tetrahedra, are called the finite elements, and the partitioned computational domain as a whole is called the finite element mesh. The elements in the mesh are defined by points in the computational domain

called nodes. In finite element method, we determine the values of the unknown variables at these nodes, which, along with the underlying local interpolation functions, will give us an approximate solution at any point inside the computational domain. In our three-dimensional model, shown in Figure 2.12 and Figure 2.13, the elements are tetrahedra. Tetrahedral elements were chosen because of their simplicity and enhanced flexibility in meshing complicated geometries.

Three-dimensional meshes can either be structured or unstructured. Structured meshes have the property that all interior nodes of the mesh have an equal number of adjacent elements and typically consist of quadralateral or hexahedral elements. This property is often well-suited for finite difference methods or for FEM problems, where block-structured techniques can be used to align mesh elements with non-trivial boundaries or important physical domains a priori. Unstructured meshes have the property that any number of elements can meet at a single node. This property allows unstructured mesh generation methods to often perform better than structured methods when applied to complicated geometries by assuring that a greater majority of elements are "well shaped", which is defined as a minimum restriction on the angles and aspect ratio of each element. Gambit is an automatic mesh generation software package designed by the CFD software company Fluent Inc.. In addition to unstructured meshing options, it also has intelligent CAD functions and a user-friendly interface. Based on these criteria, we chose to use Gambit to generate our AFM fluid cell mesh.

Our approach to generating the AFM fluid cell mesh was to first impose node spacing on all lines forming the computational geometry and then to generate two-dimensional meshes on every surface. To mesh the two-dimensional surfaces, Gambit uses the Advancing Front Method in conjunction with two-dimensional Delaunay Triangulation. This method first discretizes the boundary, then fits the boundary with triangles, continually filling the domain with at least one edge or face on the front. After all of the surfaces were meshed, Gambits tetrahedral meshing algorithm based on the Delaunay Triangulation Method was used. Delaunay triangulation is one of the most popular methods for generating unstructured meshes. The procedure is essentially composed of two phases: placement of the mesh vertices and triangulation. During the first phase of the algorithm, nodes are placed in the interior of the domain using a type of Advancing Front Method. In our case, nodes were already generated on all surfaces, allowing the modified Advancing Front Method to place nodes with the spatial density desired. The second phase of the algorithm is based upon Delaunay Triangulation. This technique utilizes the Delaunay criterion, which states that any node must not be contained within the circumsphere of any tetrahedra within the

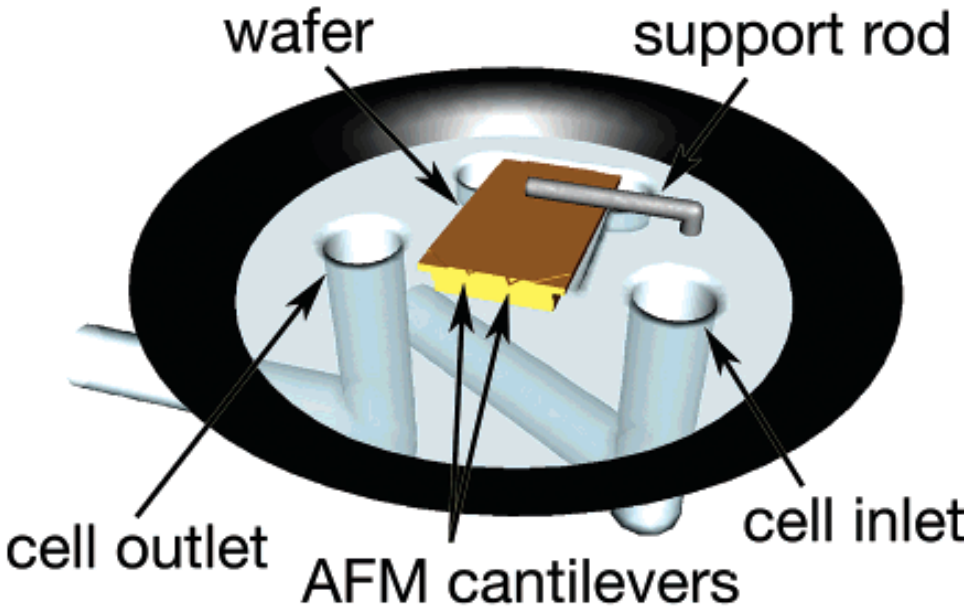

Figure 2.12: Schematic of the computational model of the AFM fluid cell. In this view, the AFM tip is pointing up; a glass slide (not shown), on which the crystals grow and subsequently are scanned, is placed on top of the sealing gasket.

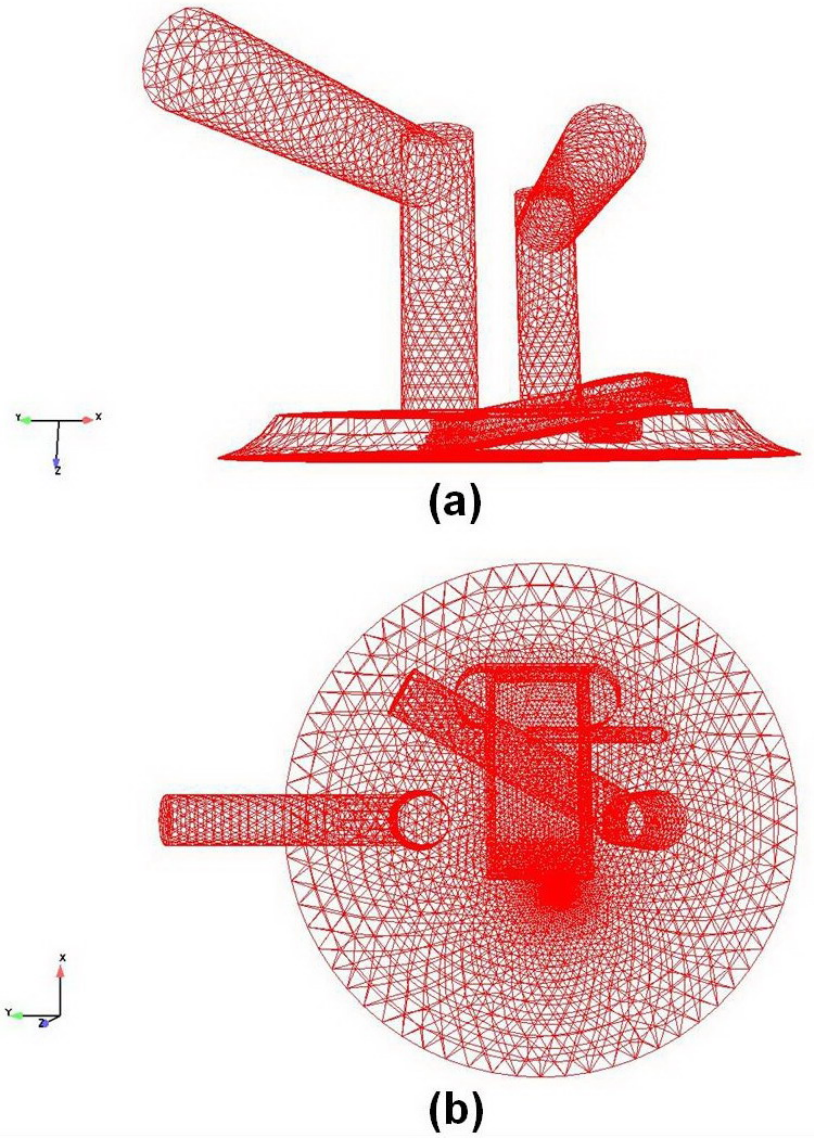

Figure 2.13: (a) side view of the global AFM fluid cell mesh. (b) Top view of the inside of the AFM fluid cell mesh. The mesh shown in (a) and (b) was used for all steady-state simulations (mesh F-22-1), and consisted of 250,517 elements and 57,029 nodes.

mesh, where a circumsphere is defined as the sphere passing through all four vertices of a tetrahedron.

The complete AFM Fluid Cell is composed of a block of glass with sides 1.25 *in.* by 1.25 *in.* on the top and bottom, and 1.25 *in.* by 0.25 *in.* on the sides. Fig. 2.12 shows that the mass transfer domain along with the direction of flow into the fluid cell and placement of the AFM cantilevers. This geometry for the numerical model was derived from a manufacturing schematic provided by Digital Instruments. The schematic was rescaled from inches to units of cell radii, with one cell radius equal to 0.125 *in.* The same geometry was used in the AFM study of Gasperino *et al.* [50].

The substrate and cantilevers in this figure were generated using measurements taken from a Veeco Instruments silicon nitride probe under an optical microscope with a micron resolution ruler. The cantilevers at the end of the probe were generated based upon both optical measurements and design specifications for the DNP-S Sharpened Silicon Nitride Probe from Veeco Instruments. The rescaled measurements for the fluid cell, probe and cantilevers were used to form a virtual geometry using the CAD software Gambit, designed by Fluent Inc..

Fig. 2.13 shows the AFM fluid cell mesh. This model contains 57,029 nodes and 250,517 elements. Fig. 2.14 shows the growing crystal surface mash and the wafer and cantilever mesh with details. A finer mesh refinement is used around the crystal than around the container walls to better resolve the flow structure close to the crystal.

Galerkin finite element formulation

As mentioned, we implemented Galerkin Finite Element Method (GFEM) to solve our governing equations. GFEM is based on a mathematical principle that a function belonging to a certain function space is zero on average when it is made orthogonal to a set of functions that belongs to a subspace of the original function space [46, 47].

To develop the GFEM formulations of our own model, we first need to write our nondimensionalized governing equations as:

$$Re(\partial\bar{\mathbf{v}} + \bar{\mathbf{v}}\cdot\bar{\boldsymbol{\nabla}}\bar{\nu}) - \bar{\boldsymbol{\nabla}}\cdot(\bar{\boldsymbol{\nabla}}\bar{\mathbf{v}} + (\bar{\boldsymbol{\nabla}}\bar{\mathbf{v}})^T) + (\frac{L}{\nu U})\bar{\boldsymbol{\nabla}}\bar{p}\underline{\underline{\mathbf{I}}} = 0 \quad (2.26)$$

$$\bar{\boldsymbol{\nabla}}\cdot\bar{\mathbf{v}} = 0 \quad (2.27)$$

$$Pe(\bar{\mathbf{v}}\cdot\bar{\boldsymbol{\nabla}}\sigma) - \bar{\boldsymbol{\nabla}}^2\sigma = 0 \quad (2.28)$$

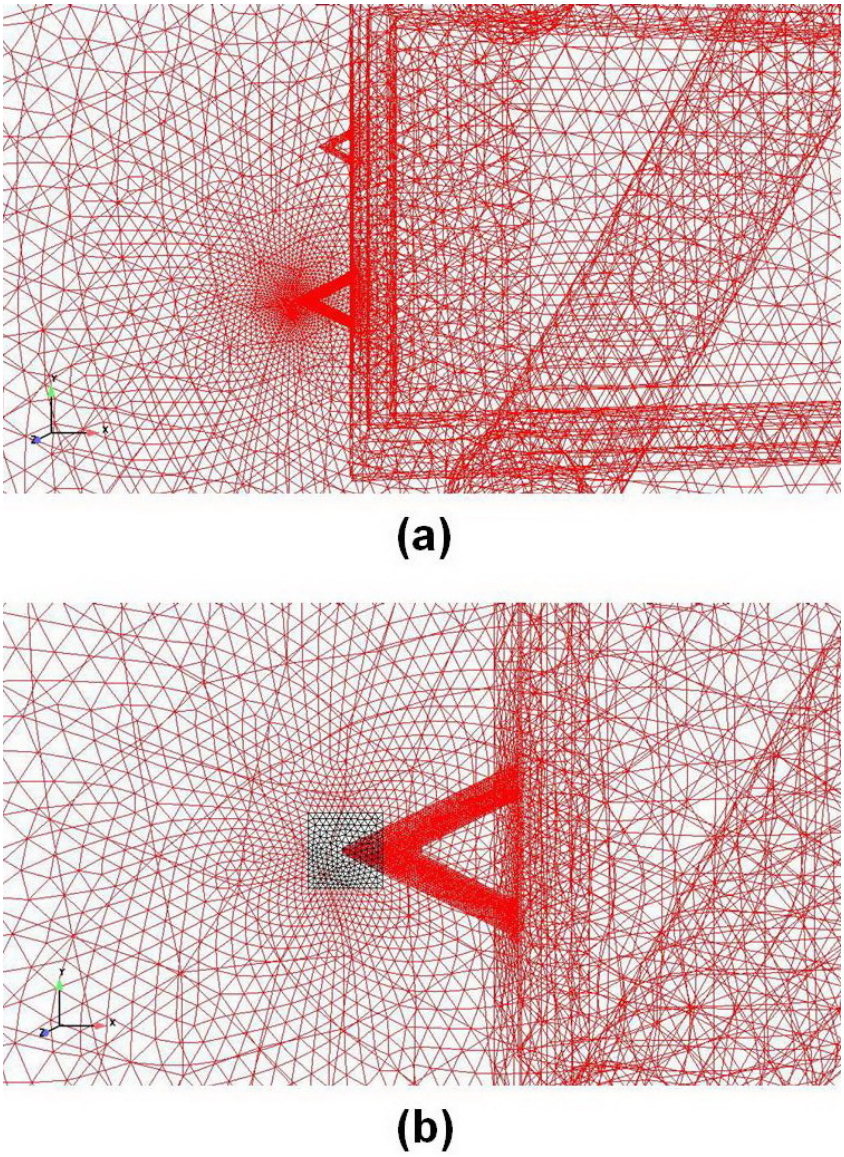

Figure 2.14: Magnified view of surface meshes near cantilever and tip. (a) The surface meshes generated for the AFM cantilevers and substrate. (b) The two-dimensional surface mesh used for the crystal surfaces and surrounding walls. Square domain under tip (colored black) in (b) indicates crystal surface.

where $\bar{\mathbf{v}}$ is the velocity scaled by the centerline velocity at the fluid cell inlet U, $\bar{\boldsymbol{\nabla}}$ is scaled by the characteristic length L which is the crystal size in our model, σ is defined by Equation 2.14, $\bar{t}$ is the time scaled by the convective time $\frac{L}{U}$, $\bar{p}$ is pressure scaled by viscous pressure $\frac{\mu U}{L}$.

Next, we multiply our residual equations by the weighting functions w and integrate the products over the entire domain, Ω:

$$R_u = \int_\Omega \mathbf{w} \cdot (Re(\partial\bar{\mathbf{v}} + \bar{\mathbf{v}} \cdot \bar{\boldsymbol{\nabla}}\bar{\nu}) - \bar{\boldsymbol{\nabla}} \cdot (\bar{\boldsymbol{\nabla}}\bar{\mathbf{v}} + (\bar{\boldsymbol{\nabla}}\bar{\mathbf{v}})^T) + (\frac{L}{\nu U})\bar{\boldsymbol{\nabla}}\bar{p}\underline{\underline{\mathbf{I}}})d\Omega \quad (2.29)$$

$$R_p = \int_\Omega w \cdot (\bar{\boldsymbol{\nabla}} \cdot \bar{\mathbf{v}})d\Omega \quad (2.30)$$

$$R_c = \int_\Omega w \cdot (Sc(\frac{\partial\sigma}{\partial\bar{t}}) + Pe(\bar{\mathbf{v}} \cdot \bar{\boldsymbol{\nabla}}\sigma) - \bar{\boldsymbol{\nabla}}^2\sigma)d\Omega \quad (2.31)$$

where $R_u, R_p,$ and R_c are the weighted residuals for momentum, continuity and species transport respectively, and $\mathbf{w}$ is the weighting functions in vector form. If we represent the last two terms in our Navier Stokes equation as $\boldsymbol{\nabla} \cdot \mathbf{T}$, where $\mathbf{T}$ is the total stress tensor, we can begin to simplify the form of our residual equations into their weak form, which requires that first order spatial derivatives of the unknowns be the highest order derivatives present. Zienkiewicz [155] states that the weak form is often physically more realistic than the original differential equation which implies excessive "smoothness' of the true solution. Primarily, the weak form of our residual equations allows us to easily implement flux-type boundary conditions, which are often used to explain natural phenomena. To reformulate our governing equations into their weak forms, starting with the momentum residual, we use the identity

$$\mathbf{w} \cdot (\boldsymbol{\nabla} \cdot \mathbf{T}) = \boldsymbol{\nabla} \cdot (\mathbf{T} \cdot \mathbf{w}) - \mathbf{T} : \boldsymbol{\nabla}\mathbf{w} \quad (2.32)$$

and with the Gauss-Ostrogradskii theorem,

$$\int_\Omega \boldsymbol{\nabla} \cdot (\mathbf{T} \cdot \mathbf{w})d\Omega = \oint_S \mathbf{n} \cdot (\mathbf{T} \cdot \mathbf{w})dS \quad (2.33)$$

where S is the surface domain, we can get the weak form of the governing equations for

momentum, and species transport as:

$$R_{u,GLS} = \int_\Omega \mathbf{w} \cdot \left[Re \left(\frac{\partial \bar{\mathbf{v}}}{\partial \bar{t}} + \bar{\mathbf{v}} \cdot \bar{\boldsymbol{\nabla}} \bar{\nu} \right) \right] d\Omega + \int_\Omega \mathbf{T} \colon \boldsymbol{\nabla} \mathbf{w} d\Omega - \oint \mathbf{n} \cdot (\mathbf{T} \cdot \mathbf{w}) dS \tag{2.34}$$

$$R_{c,GLS} = \int_\Omega w \cdot \left[Sc \left(\frac{\partial \sigma}{\partial \bar{t}} \right) + Pe(\bar{\mathbf{v}} \cdot \bar{\boldsymbol{\nabla}} \sigma) \right] d\Omega + \int_\Omega \boldsymbol{\nabla} \mathbf{w} \cdot \boldsymbol{\nabla} \sigma d\Omega - \oint \mathbf{w} \mathbf{n} \cdot \boldsymbol{\nabla} \sigma dS \tag{2.35}$$

Then, solution for the the unknowns $\bar{\mathbf{v}}, \sigma$ and $\bar{p}$ in the residual equations can be constructed from linear combinations of piecewise basis functions:

$$\begin{bmatrix} \bar{v}_x(x,y,z,t)\mathbf{e_x} \\ \bar{v}_y(x,y,z,t)\mathbf{e_y} \\ \bar{v}_z(x,y,z,t)\mathbf{e_z} \\ \sigma(x,y,z,t) \end{bmatrix} = \sum_{j=1}^{N} \begin{bmatrix} \bar{v}_x^{(j)}(t)\mathbf{e_x} \\ \bar{v}_y^{(j)}(t)\mathbf{e_y} \\ \bar{v}_z^{(j)}(t)\mathbf{e_z} \\ \sigma^{*(j)}(t) \end{bmatrix} \Phi^j(x,y,z), \tag{2.36}$$

$$\bar{p}(x,y,z,t) = \sum_{j=1}^{N} \bar{p}^{(j)}(t) \Psi^j(x,y,z) \tag{2.37}$$

where $v_x^{(j)}(t)$, $v_y^{(j)}(t)$, $v_z^{(j)}(t)$, and $p^{(j)}(t)$ are the interpolation coefficients representing the nodal values of the velocity components and pressure, N is the total number of nodes in the mesh, and $\Phi^j(x,y,z)$ and $\Psi^j(x,y,z)$ are the basis functions. These two basis functions are different since a lower order basis function is normally used for pressure while solving the Navier-Stokes equation with FEM. Now Eq. (2.37) can be substituted into the Galerkin weighted residuals equations, and we can solve for the unknown interpolation coefficients by assuming appropriate test functions. To complete the transformation of our weighted residuals into Galerkin weighted residuals, the weights, $\mathbf{w}$ and w, in our residual equations are replaced by $\Phi^j(x,y,z)$, the same basis functions from Equation 2.37.

Galerkin/least-squares method

When applied to the Navier-Stokes equations, however, the Galerkin finite element method described in the previous section suffers from numerical instabilities that result in poorly converged or unstable solutions. The particular choice of linear basis functions to represent both the velocity and pressure variables leads to oscillations in the pressure field, while

applications to high Reynolds number flows (highly convective flows) lead to oscillations in the velocity field [119]. To overcome these problems, we have employed the Galerkin/least-squares (GLS) method [63,119], which stabilizes against oscillations in velocity and pressure fields by adding extra terms to the standard weighted Galerkin residuals. The GLS method is one of the most general form of the stabilized finite element methods that combines the features of both the streamline-upwind/Petrov-Galerkin (SUPG) [20] and pressure-stabilizing/Petrov-Galerkin (PSPG) [121] type of stabilization methods. The semi-discrete GLS residuals form for the momentum transfer, mass transfer and the continuity equation in our model are written as follows:

$$\begin{aligned} R_{u,GLS} &= \int_\Omega \mathbf{w}\cdot\left[Re\left(\frac{\partial\bar{\mathbf{v}}}{\partial\bar{t}}+\bar{\mathbf{v}}\cdot\bar{\boldsymbol{\nabla}}\bar{\nu}\right)\right]d\Omega+\int_\Omega \mathbf{T}\colon\boldsymbol{\nabla}\mathbf{w}d\Omega-\oint\mathbf{n}\cdot(\mathbf{T}\cdot\mathbf{w})dS \\ &\quad+\sum_{e=1}^{N_el}\int_{\Omega^e}\tau(\bar{\mathbf{v}}\cdot\bar{\boldsymbol{\nabla}}\mathbf{w})\cdot\left(\frac{\partial\bar{\mathbf{v}}}{\partial\bar{t}}+\bar{\mathbf{v}}\cdot\bar{\boldsymbol{\nabla}}\bar{\nu}-\bar{\boldsymbol{\nabla}}\cdot T\right)d\Omega^e \\ &\quad+\sum_{e=1}^{N_el}\int_{\Omega^e}\delta\bar{\boldsymbol{\nabla}}\cdot\mathbf{w}\bar{\boldsymbol{\nabla}}\cdot\bar{\mathbf{v}}d\Omega^e \end{aligned} \tag{2.38}$$

$$R_{p,GLS} = \int_\Omega w\cdot(\bar{\boldsymbol{\nabla}}\cdot\bar{\mathbf{v}})d\Omega+\sum_{e=1}^{N_el}\int_{\Omega^e}\tau\bar{\boldsymbol{\nabla}}w\cdot\left(\frac{\partial\bar{\mathbf{v}}}{\partial\bar{t}}+\bar{\mathbf{v}}\cdot\bar{\boldsymbol{\nabla}}\bar{\nu}-\bar{\boldsymbol{\nabla}}\cdot T\right)d\Omega^e \tag{2.39}$$

$$\begin{aligned} R_{c,GLS} &= \int_\Omega w\cdot\left[Sc\left(\frac{\partial\sigma}{\partial\bar{t}}\right)+Pe(\bar{\mathbf{v}}\cdot\bar{\boldsymbol{\nabla}}\sigma)\right]d\Omega+\int_\Omega\boldsymbol{\nabla}\mathbf{w}\cdot\boldsymbol{\nabla}\sigma d\Omega \\ &\quad-\oint\mathbf{w}\mathbf{n}\cdot\boldsymbol{\nabla}\sigma dS \\ &\quad+\sum_{e=1}^{N_el}\int_{\Omega^e}\tau_c(\bar{\mathbf{v}}\cdot\mathbf{w})\cdot\left[Pe\left(\frac{\partial\sigma}{\partial\bar{t}}+\bar{\mathbf{v}}\cdot\bar{\boldsymbol{\nabla}}\sigma\right)-\bar{\boldsymbol{\nabla}}^2\sigma\right] \end{aligned} \tag{2.40}$$

In Euqation 2.39 to 2.40, Ω^e represents the element domain and Nel is the total number of elements int each computational domain. The term τ is defined for each element as:

$$\tau = \left[\left(\frac{2}{\Delta\bar{t}}\right)^2+\left(\frac{2\|\bar{\mathbf{v}}_e\|}{h_e}\right)^2+\left(\frac{4}{Reh_e^2}\right)^2\right]^{-\frac{1}{2}} \tag{2.41}$$

where $\Delta\bar{t}$ is the dimensionless time step, $\|\bar{\mathbf{v}}_e\|$ is the L_2-norm of the local velocity in the element, and h_e is the largest dege length in the element. The term δ in the FLS residual

for momentum transfer is defined as:

$$\delta \;=\; \begin{cases} \frac{1}{6} h_e \|\bar{\mathbf{v}}_e\| Re_e & \text{for } Re_e \leq 3, \\ \frac{1}{2} h_e \|\bar{\mathbf{v}}_e\| & \text{for } Re_e \geq 3. \end{cases} \tag{2.42}$$

where Re_e is the element Reynolds number, and is defined as

$$Re_e \;=\; \frac{h_e \|\bar{\mathbf{v}}_e\| Re}{2} \tag{2.43}$$

In Equation 2.40 for the species conservation, τ_c is defined as:

$$\tau_c \;=\; \left[\left(\frac{2Pe}{\Delta \bar{t}} \right)^2 + \left(\frac{2\|\bar{\mathbf{v}}_e\| Pe}{h_e} \right)^2 + \left(\frac{4}{Re h_e^2} \right)^2 \right]^{-\frac{1}{2}} \tag{2.44}$$

In both Equation 2.39, the first term is the standard Galerkin weighted residual for the momentum conservation equation, and the second term is the stabilization term which comes from the least-squares form of the momentum equation evaluated and summed over each element of the computational domain Ω^e. The third term in Eq. 2.39 is another stabilization term which is a least-squares form of the continuity equation. Similarly a stabilization term is added to the Galerkin weighted residual of the continuity equation, as shown in Eq. 2.40. The GLS formulation is consistent with the standard Galerkin formulation since the stabilization terms include the momentum and continuity residuals as common factors, which tend to zero as the solutions converge.

When we substitute our discretized spatial approximations for our variables represented in Equation 2.37 into our GLS residual equations, the equation can be written in the matrix-vector form as:

$$\mathbf{M} \frac{dq}{d\bar{t}} \;=\; \mathbf{F}(\mathbf{q}) \tag{2.45}$$

where the $\mathbf{q}$ is the unknowns vector:

$$\mathbf{q} \;=\; \left[\bar{v}_x^1, \ldots, \bar{v}_x^N, \bar{v}_y^1, \ldots, \bar{v}_y^N, \bar{v}_z^1, \ldots, \bar{v}_z^N, \bar{p}^1, \ldots, \bar{p}^N, \sigma^{*,1}, \ldots, \sigma^{*,N}, \right] \tag{2.46}$$

With the superscripts indicating the global node number. The matrix **M**, known as the mass matrix, contains the coefficients of the time-derivatives of the unknowns and the matrix **F** is a nonlinear vector function of **q** that includes all terms in the weak form of the residuals that do not contain a time-derivative of the unknowns.

Solving the nonlinear equations

To solve the nonlinear set for the solution vector **q**, Newton-Raphson method was used. Iteration is continued until the L_∞-norm of the solution update vector,

$$\|\boldsymbol{\delta}\|_\infty = \max_i |\delta_i| \tag{2.47}$$

and the L_∞-norm of the residual vector:

$$\|\mathbf{R}(\mathbf{q}_l)\|_\infty = \sqrt{\sum_{i=1}^{N} |R_i(\mathbf{q}_l)|^2} \tag{2.48}$$

are less than the specified error tolerance, ϵ, which is usually less than 10^{-6}.

In our model, however, the L_∞-norm of the update vector is comparatively large (because the unknown pressure **p** solved in Navier-Stokes equation contains an uncertain constant). In this case, the L_∞-norm value of the residual vector is used to verify convergence of our problem.

Parallel implementation

The numerical methods hitherto described are implemented in the form of a FORTRAN code on a distributed memory, multiple-processor supercomputer. The main feature of the supercomputer is the large number of processors running in parallel and large memory, which allow us to carry out heavy computation involving millions of degrees of freedom.

There are two key issues in an effective utilization of the supercomputer's massively parallel processing. One is the issue of distributing the computational load among processors, and the other one is the data communication among processors which acts as a bottleneck to the overall computational speed. For an efficient parallel computation, one must ensure that the computational load is evenly distributed among processors, and the computation is carried out with as little inter-processor communication as possible. This is also depends on partitioning sub-domains of the mesh to processors. This work is

important and challenging.

The data structure resulting from the finite element method makes itself suitable for such an efficient parallel computation. The volume and the surface integrals in the weak form collapse to integrals just over each element, due to the piecewise nature of the local basis functions. Hence the component of the residual vector need to be assembled only within each element. By assigning the elemental data set (values of the local basis functions and their derivatives at Gauss points, Gauss weights and etc.) to individual processors of the supercomputer, the element-level residual vector and Jacobian entries for each element can be computed simultaneously, without any inter-processor communication.

After element-level residual vector and Jacobian entries have been computed, we use the GMRES (Generalized Minimal Residual) iterative method [98] to solve the linear equation set. We employ diagonal preconditioning in tandem to speed up the convergence of solution [97, 145]. Not only does the GMRES iterative method allow substantial savings of memory and computational effort compared to direct solution methods such as the Gaussian elimination and LU decomposition, but it is also well suited for an efficient parallel computation. The matrix-vector multiplications involved in the GMRES routine is performed on the element-level, and thus can utilize the same elemental data structure used in the computation of the residual vector and the Jacobian entries. Again this ensures an even distribution of computational load among processors of the supercomputer.

After the matrix-vector multiplication is completed, the resulting update vector residing in individual processor is *scattered* to the global-level, and modified Gram-Schmidt orthogonalization is carried out to construct an update to the global solution vector. The no-slip boundary condition is also implemented at this global-level by replacing the appropriate global residual equation. The new orthogonal vector is then *gathered* back to the individual processor to be used in the next set of matrix-vector multiplication. Such scattering and gathering of data sets are also necessary for preconditioning of the Jacobian matrix between each Newton-Raphson iteration. To reduce the cost inter-processor communication during these scattering and gathering operation, we take advantage of the METIS and MPI scientific library routines to partition the mesh into groups of elements, and assign each partition to individual processor. Communication between processors can now be minimized since only the elemental data sets corresponding to the partition boundaries need to be sent across different processors.

Code development and the memory usage

Cats3D (Crystallization and Transport Simulator), developed by the Derby research group, is used to solve the model equations [39, 74, 99, 101, 146]. The MPI-based parallel code is capable of solving steady-state or transient three-dimensional multiphase problems on an unstructured mesh of tetrahedral elements. The Galerkin-Least Squares finite element implementation is used to discretize the equations, and GFEM with SUPG is used to discretize the species conservation equation. A GMRES iterative solver is used to solve the linear system.

The new version of Cats3D is based on 15-noded tetrahedral elements. The new partition code which read 4-noded mesh decomposes the domain and expands this old mesh into 15-noded tetrahedral elements based mesh. This would lead to more accurate numerical solutions to the our governing equations.

2.2.3 Model validation

To validate our model, we compared our computation results with experimental flow visualization result conducted by Gasperino *et al.* [52]. The experimental flow visualizations were performed in the AFM fluid cell with A particle-path tracing technique [42]. This technique utilizes video microscopy of light reacted tracer particles and reveals the fluid flow path line in the fluid cell. A comparison of the experimental result and the computed flow path line is shown in Fig. 2.15. As we can see, experimental flow trace shows very similar pattern as the calculated flow lines. This agreement between experiment and modeling data validates the model.

2.3 Results and Discussion

We carry out computations for the solute field around a growing crystal in this AFM flow cell. The inner diameter of the cell is 0.66 cm, while the thickness of the cell is taken to be 637 μm [52,130]. We assume that the crystal is a square with sides of length 120 μm that is located directly under the scanning cantilever and tip, as indicated in Figure 2.14(b). We assume that the solvent for all cases is water at 25^oC, with properties listed in Table 2.1. We set an inlet fluid velocity as 1 cm/s, which would correspond to a volumetric flow rate of 4 μL/s and a Reynolds number for flow of $Re = 1.2$. Flow rates of this magnitude have been commonly employed in AFM crystal growth experiments [66, 133]. We also assume that the inlet supersaturation is $\sigma_0 = 0.5$; this assumption is not restrictive, since any other

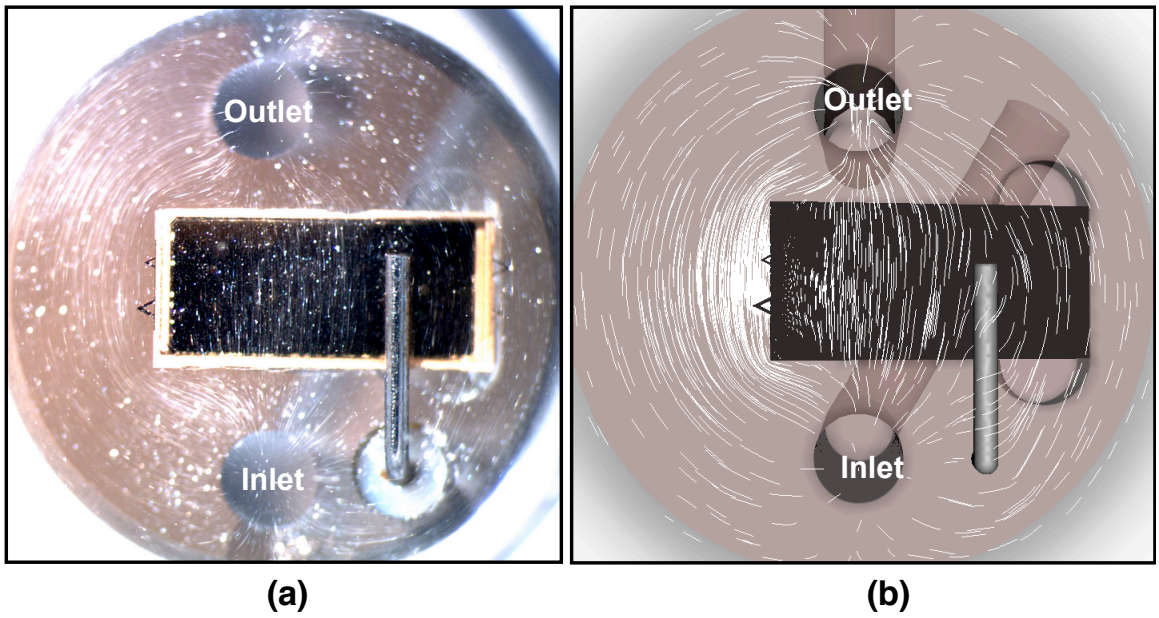

Figure 2.15: (a)Snapshots of pathline trajectories in the AFM fluid cell during flow visualization experiments [52]. (b) computational simulations of the flow pathline.

Table 2.1: Physical properties and system parameters used to model the AFM fluid cell system.

Parameter	Value	Units
Crystal edge length, L_c	0.0120	cm
Fluid cell thickness, L	0.0637	cm
Inlet centerline velocity, U	1.00	cm/s
Solution viscosity, μ	1.00×10^{-2}	g/cm·sec
Solution density, ρ	0.997	g/cm^3

inlet value can be represented by a simple rescaling of the predicted supersaturation field.

In the current study, four representative crystal growth systems are considered, featuring both inorganic and organic molecules of different sizes. We focus on the behaviors that will arise for different crystals grown under nominally identical conditions. Thus, we choose to keep the flow rate, the inlet supersaturation, and the crystal size constant for all simulations performed here. In particular, Gasperino *et al.* [50] showed that flow rate variation had very little effect on solute mass transfer due to the shielding effect of the AFM cantilever and tip during the growth of COM in this system.

Calcium oxalate monohydrate (COM) serves as a reference growth material for our prior [50] and current study. As a major component of kidney stones, COM crystal growth mechanisms [35,56,57,91,153] and growth inhibition [7,66,113,135] have been well studied. We choose to study three additional systems—potassium dihydrogen phosphate (KDP), Lysozyme, and Canavalin. Potassium dihydrogen phosphate, an inorganic crystal that grows rapidly, is a well studied optical crystal [3, 49, 90]. Lysozyme and canavalin are protein molecules that readily crystallize from solution. Canavalin is the major storage protein of the jack bean, and many studies have been done to understand its crystal growth mechanism [8, 29]. Lysozyme is perhaps the most studied of protein crystals; see, e.g., [41, 110, 116]. The properties associated with transport and crystal growth for these systems are listed in Table 2.2.

In the following discussion, we first present the form of the velocity field through the AFM measurement cell, as predicted by our finite-element model. We then present solute

Table 2.2: Physical properties of the crystal growth systems

Property	Units	KDP	COM	Lysozyme	Canavalin
Solute solubility, c_{eq}	g/cm^3	2×10^{-1}	2×10^{-5} [51]	3×10^{-3}	3×10^{-2} [36]
Solute diffusivity, D	cm^2/s	8.75×10^{-6} [59]	8.78×10^{-6} [51]	1.00×10^{-6} [40]	1.23×10^{-6} [67]
Kinetic coefficient, β	cm/s	1.00×10^{-3} [4]	1.55×10^{-8} [51]	1.00×10^{-5} [29]	9.00×10^{-6} [29]
Crystal density, ρ_c	g/cm^3	2.33	2.20 [51]	0.820	1.11 [84]

supersaturation fields in this system near the growing crystal. Numerical results demonstrate the inhomogeneous distribution of surface supersaturation levels caused by the interactions of flow, diffusion, and growth kinetics for the four different crystal systems. Following the details of the numerical solutions, we present scaling analyses to explain the general behavior of these systems, followed by a discussion of implications for interpretation of kinetic data measured for crystal growth in AFM fluid cells.

2.3.1 Velocity field

Gasperino *et al.* [50] provided an extensive discussion of the flow field through this AFM system. Here, we briefly revisit the nature and form of this flow. As stated above, this flow is characterized by a nominal Reynolds number of $Re = 1.2$, which indicates that, while inertia is important, the flow is laminar and steady in nature. Figure 2.16 shows selected pathlines, colored by velocity magnitude, for the flow within the fluid cell.

The global flows are represented in Figure 2.16(a). In this visualization, the fluid cell was placed upside down compared to its typical experimental orientation. Liquid enters and flows across the cell from left to right in the image. The flow across the cell slows somewhat compared to the inlet velocities due to the relatively larger cross sectional area of the cell compared to the inlet. Due to inner blockage of the cell by the support rod and wafer assembly, more fluid is directed toward the tip side of the cell (upper right in image). This redirection of the flow is beneficial, since the higher flow preferentially supplies supersaturated solvent near the growing crystal under the imaging tip.

Pathlines representing flows near the growing crystal are indicated in Figure 2.16(b), which is a view looking at the AFM tip over the growing crystal with the flow directed from bottom to top of this image. Consistent with those computed previously [50], the local flow is aligned in a reasonably uniform manner across the crystal. However, what cannot be seen in this visualization is that the flow is deflected over the cantilever (i.e., out of the plane of this image), so that a nearly stagnant region is formed under the AFM tip. This shielding from the flow and subsequent mass transfer effects were discussed by Gasperino *et al.* [50]. The different flow effects under the cantilever and away from it will be discussed in the subsequent results presented here.

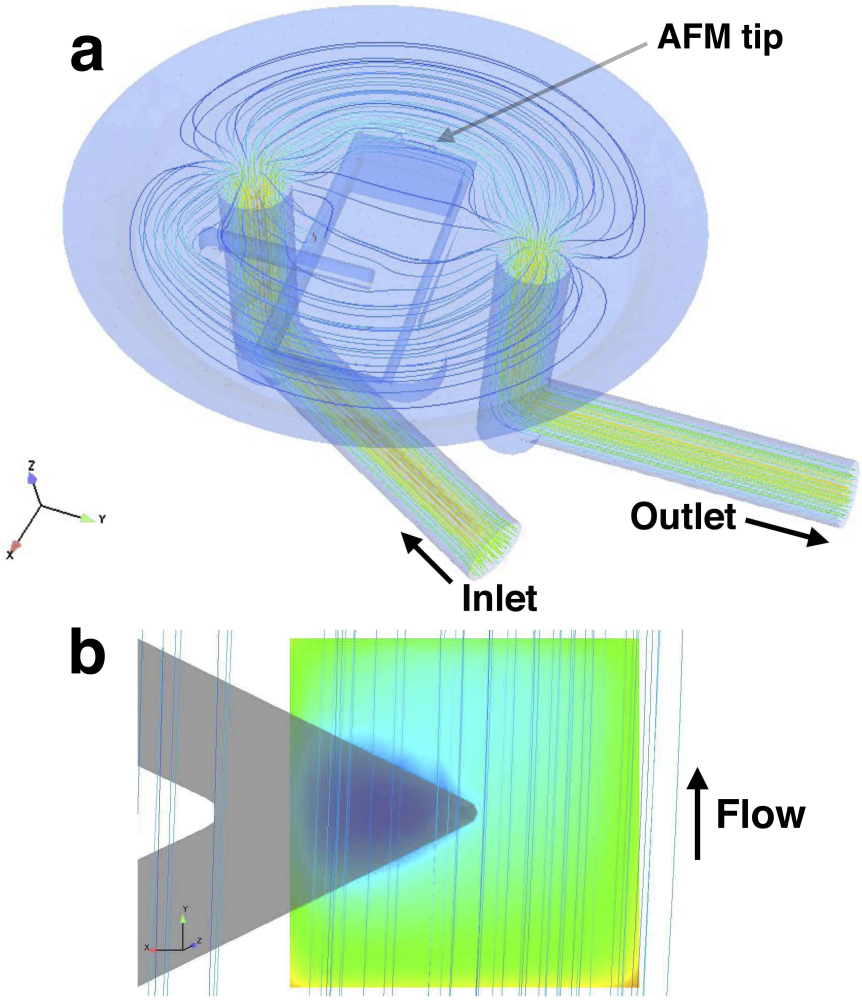

Figure 2.16: (a) Pathlines, colored according to magnitude of velocity (red is faster; blue is slower), show solution flows through AFM fluid cell. (b) Selected pathlines show a uniform flow across the crystal and AFM tip.

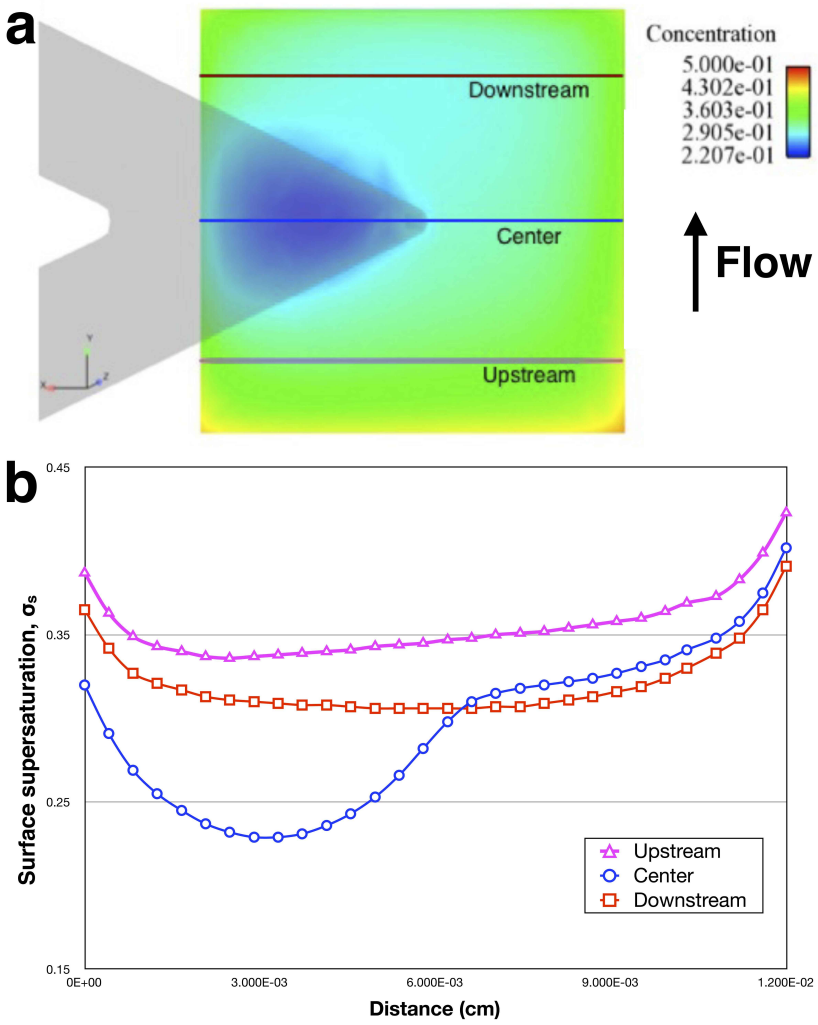

Figure 2.17: Solute supersaturation on the growing COM crystal surface; AFM cantilever is shown in gray. (a) Visualization of the growing crystal surface, colored by surface supersaturation, shows significant depletion under the cantilever. (b) Supersaturation profiles are plotted across the crystal surface along indicated upstream, center and downstream positions. Distance is measured from inward (left) to outward (right) edge of the crystal.

2.3.2 Solute supersaturation field

COM crystal growth

To illustrate the general effects of mass transfer limitations occurring in this system, we initially focus on the spatial distribution of supersaturation computed across the surface of a growing COM crystal (assumed to be a square of 120 μm). Figure 2.17(a) shows surface supersaturation as a function of color across the crystal, with a gray image of the AFM tip overlaying the crystal to show its relative position. The flow direction is indicated by the arrow, and the color scale on the right indicates the predicted level of supersaturation.

Even though this crystal is quite small, there are significant variations in the surface supersaturation, which ranges from a maximum value of $\sigma_s = \sigma_0 = 0.5$ in the outward, upstream corner to a minimum of $\sigma_s = 0.22$ under the AFM cantilever. Examining the outward surface, not covered by the AFM tip, it is evident that the surface supersaturation is higher at the edges of the crystal, where the flowing solution can easily replenish the supply of solute. At the leading edge of the crystal, first exposed to the flow, the supersaturation is highest, and its value decreases in the downstream direction as solute is depleted from the overlying solution via continuous incorporation into the growing crystal.

This effect is also evident in Figure 2.17(b), which plots the supersaturation across the surface along the three lines (indicated by upstream, center, and downstream) drawn across the crystal in Figure 2.17(a). The origin of each plotted profile is the left edge of the crystal. Note that in the outer surface region, to the right beyond the tip, the curves show a steady decrease in supersaturation from upstream to downstream. The upward rise in all curves as distance increases is indicative of the sideways diffusion of solute from adjacent solution flow that has not been depleted of solute.

Of particular significance is the very low surface supersaturation levels directly beneath the AFM cantilever shown in Figure 2.17(a). In this region, the depletion of solute caused by crystal growth cannot be resupplied by the liquid flowing overhead, since most of the flow is directed over the cantilever. The depleted region of surface supersaturation is also evident in the center profile of Figure 2.17(b), where the supersaturation profile is strongly depressed with respect to both upstream and downstream profiles.

Other crystal growth systems

AFM measurements have been applied to measure a wide variety of crystals, each having different transport and kinetic properties. Thus, it is illuminating to consider the effects of

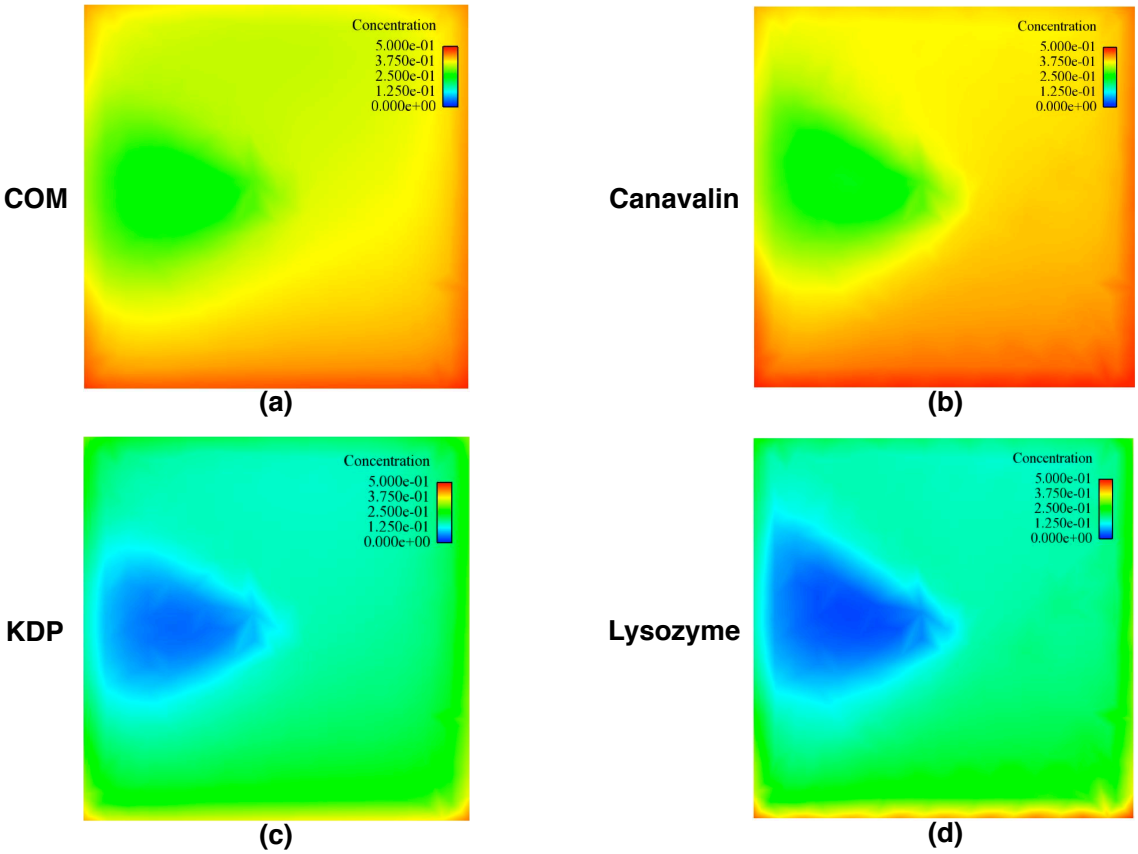

Figure 2.18: Surface supersaturation distributions are shown across crystal surfaces, under identical growth conditions, for (a) COM, (b) KDP, (c) Canavalin, and (d) Lysozyme. Color scale is the same for each plot.

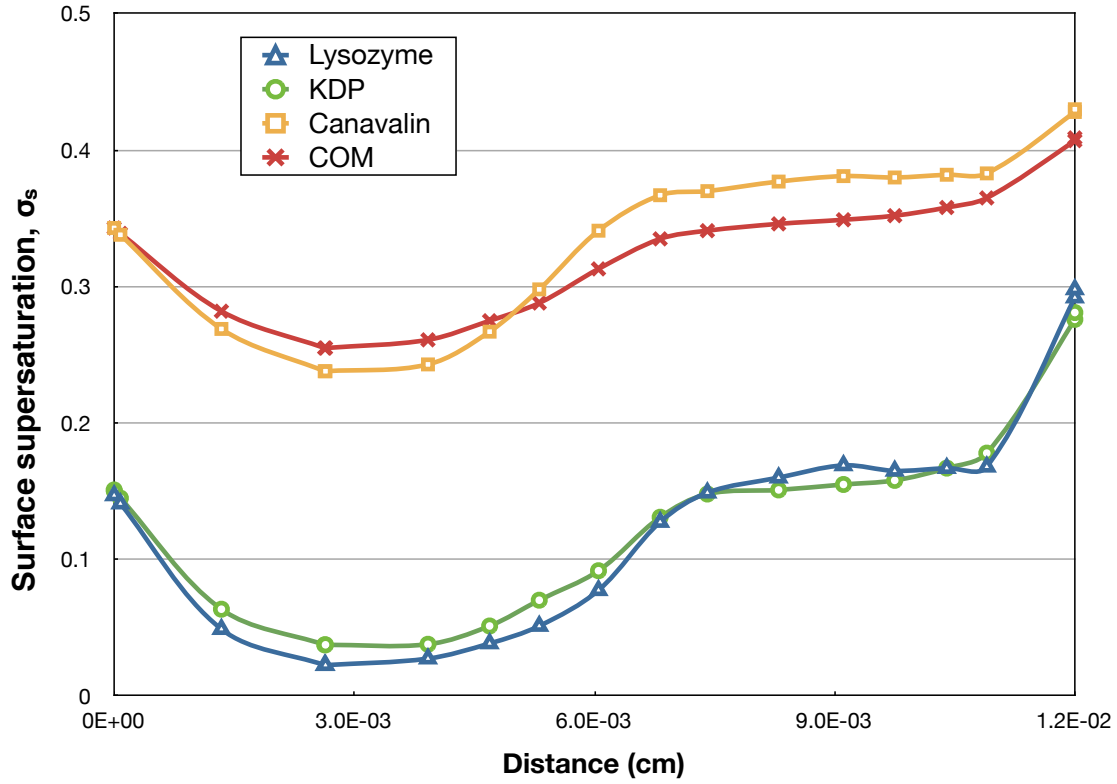

Figure 2.19: Surface supersaturation profiles of KDP, COM, Canavalin and Lysozyme systems are plotted along the center of the crystal surface, as defined by the profile shown in Figure 2.17. The vertical dashed line represents the location of the AFM tip and marks the boundary between the surface region under the cantilever (on left) and that away from it (on right).

mass transport limitations in the AFM flow cell under different conditions. We therefore carry out simulations for the growth of KDP, Lysozyme, and Canavalin and compare their behaviors to that of COM growth.

Predicted supersaturation distributions across the crystal surface under identical conditions of flow and crystal size are shown for these four systems in Figure 2.18. The same color scale for supersaturation is used in all images, and the gray cantilever depiction is not shown for increased clarity. In all cases, the flow direction is from the bottom toward the top of the page. As we can see, with the same initial supersaturation $\sigma_0 = 0.5$ and same fluid flow conditions, the surface supersaturations for these four crystals show similar characteristics but are quantitatively very different. In particular, there are significant

differences in the extent of solute depletion under the AFM cantilever and tip.

A more quantitative comparison is shown by Figure 2.19, where profiles of supersaturation are plotted across the centerline of the crystal, using the same center path as in Figure 2.17(a), for the four different cases. Note that the Lysozyme system exhibits the lowest surface supersaturation levels, with a minimum that is over ten times less than the inlet supersaturation value, followed by the KDP system. Interestingly, in spite of the very different molecular sizes, the Canavalin and COM systems exhibit nearly the same supersaturation profiles, with the profile of Canavalin lying slightly under that of COM across most of the region under the cantilever. However, their order is reversed away from the cantilever, over the outer region of the crystal, with the Canavalin profile overlying that of COM. These different behaviors are understood in terms of diffusional and kinetic interactions, as discussed in the following section.

2.3.3 Scaling analyses

In the following analyses, we focus on the supersaturation distributions across the surfaces of the different growing crystals. We specifically examine the relative values for the different systems in two positions on the crystal surface—the points of minimum supersaturation along the center profiles that occur away from the cantilever and under the cantilever. Via scaling analyses, we will explain the relative ordering of these profiles and focus in particular on the change in ordering of the relative supersaturation minima exhibited by the COM and Canavalin systems, as previously shown in Figure 2.19.

We have assumed a fixed flow rate through the system, which sets a constant value for the Reynolds number of $Re = 1.20$ in eq. (2.5) and makes the flow identical for each case considered. The solute field will be determined by the dimensionless groups appearing in eqs. (2.15) and (2.23). For the analyses that follow, it will be useful to interpret the solutal Peclet number as the product of the dimensionless Schmidt and Reynolds number as follows,

$$Pe = ScRe, \tag{2.49}$$

where $Sc = \nu/D$, with ν denoting the kinematic viscosity of the fluid. The other parameter of interest is the modified Damköhler number, whose definition we repeat here as,

$$Da = \frac{\rho_c \beta L_c}{D c_{eq}}. \tag{2.50}$$

The final dimensionless group corresponds to the solubility ratio, c_{eq}/ρ, and is not affected

Table 2.3: Scaling analysis for the crystal growth systems.

Dimensionless group	KDP	COM	Lysozyme	Canavalin
Modified Damköhler number, Da	16.0	2.33	32.8	3.25
Schmidt number, Sc	1,150	1,140	10,000	8,160
Solubility ratio, c_{eq}/ρ	2.00×10^{-1}	2.00×10^{-5}	3.00×10^{-3}	3.00×10^{-2}
Predicted $\sigma_{s,min}$ away from cantilever	0.10	0.32†	0.10	0.36
Predicted $\sigma_{s,min}$ under cantilever	0.038	0.22†	0.019	0.17

†Reference value used in scaling relationship; see text for more details.

by our new choice of characteristic length scale. The values of these dimensionless groups are listed in the first lines of Table 2.3.

Surface supersaturation away from the cantilever

Figure 2.20 shows the supersaturation fields above the COM and Canavalin crystals on a plane that is aligned normal to the crystal surface and with the direction of flow, parallel to and 2.5 μm away from from the right edge of the crystal. Notice that depletion boundary layers form near the crystal surface (indicated in black at the bottom of the plots) as solute is drawn from the liquid to supply the growth of the underlying crystal. Note also that the boundary layer for the Canavalin growth system is much thinner than that for the COM system.

From classical boundary layer theory [107], we expect that the thickness of a concentration layer within a flow past a surface should scale as

$$\delta_{\sigma} \propto Sc^{-1/3} Re^{-1/2}, \tag{2.51}$$

where δ_{σ} is the solutal boundary layer thickness and the dimensionless Schmidt and

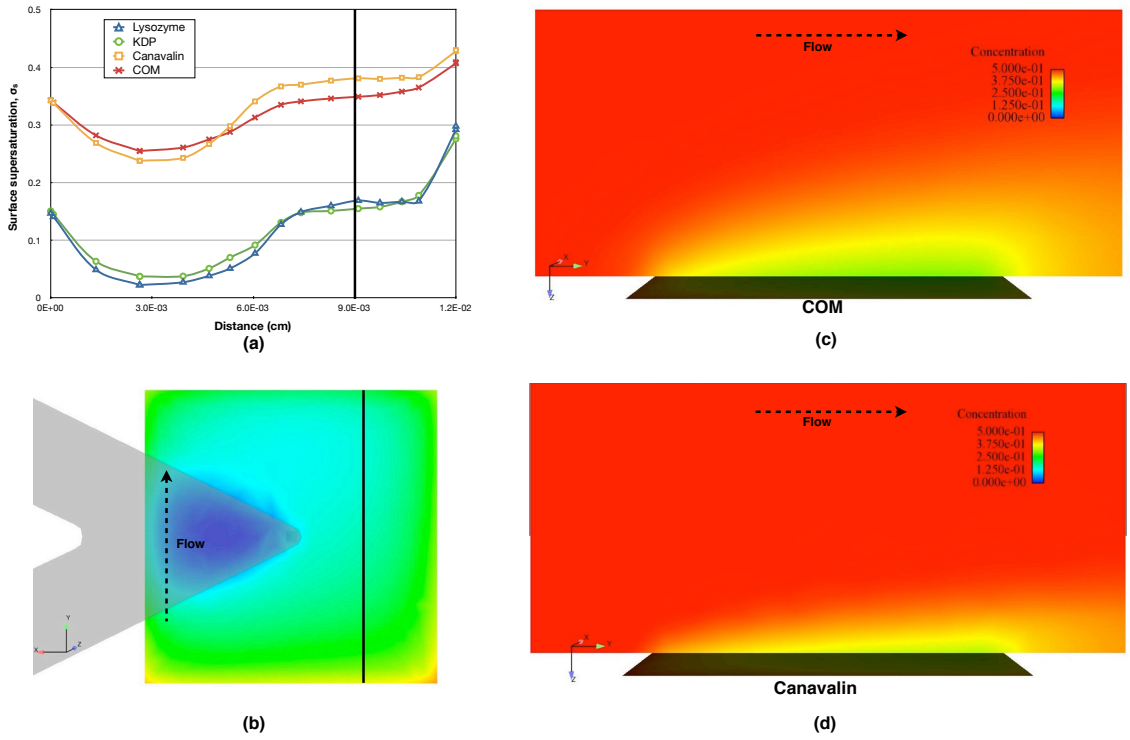

Figure 2.20: Visualization of solute supersaturation field in fluid along a clip plane defined by the solid lines in (a) and (b). Depletion boundary layers are evident above the growing (c) COM crystal and (d) Canavalin crystal.

Reynolds numbers are as previously defined.

We have fixed the fluid and the flow, so that the Reynolds number is constant for each system. Therefore, we expect that the concentration boundary layers for the two systems to be related as

$$\frac{\delta_{\sigma,COM}}{\delta_{\sigma,Canavalin}} = \left(\frac{Sc_{COM}}{Sc_{Canavalin}}\right)^{-1/3} \approx 1.93, \tag{2.52}$$

indicating that the much higher diffusion coefficient of COM is expected to result in a solutal boundary layer thickness that is nearly double that for the Canavalin system. This is in very good agreement with the results shown in Figure 2.20.

To understand behavior of the surface supersaturation profiles requires the consideration of both mass transfer through the boundary layer combined with the surface kinetics associated with the growth of the crystal. Chambré and Acrivos [25] solved for first-order surface reactions in a laminar boundary layer flow via a similarity analysis. They provided an exact solution for surface concentration as a function of position from the leading edge in terms of an infinite series; however, they also showed that a reasonable approximate solution was given by

$$\frac{c(\eta)}{a} = \frac{1}{\eta + 1}, \tag{2.53}$$

where c represents surface concentration, a is the free-stream concentration value, and η is a similarity variable defined as

$$\eta \equiv \frac{1}{0.339} Sc^{-1/3} Re_{\infty}^{-1/2} Da \left(\frac{y}{L}\right)^{\frac{1}{2}}, \tag{2.54}$$

where y represents the distance on the surface from the leading edge, L is the length of the surface, and the dimensionless Schmidt and Damköhler numbers are as defined previously (with β representing the first-order reaction rate constant). The dimensionless Reynolds number in this expression, Re_{∞}, is based upon the free-stream liquid velocity, which is not strictly equivalent to our definition of Re, which is based on the maximum inlet velocity.

We expect the exposed surface of the growing crystal to be nearly equivalent to the reacting surface analyzed by Chambré and Acrivos. Indeed, if we interpret $c/a = \sigma/\sigma_0$ and $L = L_c$, the systems are quite similar mathematically, provided that our original surface flux boundary condition, eq. (2.23), can be simplified to a first-order expression (as is argued to be a good approximation in the following section). Unfortunately, we cannot

directly apply eq. (2.54) to our system, since our flow conditions are different from those of the idealized boundary layer analysis and $Re \neq Re_\infty$.

However, we can circumvent this difficulty by arguing that Re_∞ is constant, due to the identical flow conditions employed in each system, and take the ratio of similarity variables to compare between systems. Therefore, if we choose COM as a reference and observe from Figure 2.19 that the surface supersaturation reaches a nearly constant value of $\sigma_{s,COM} \approx 0.32$ over the exposed surface, we can use eq. (2.53) to compute a value of $\eta_{COM} \approx 0.56$ as the position along the COM surface where this minimum supersaturation is attained. From the definition of η in eq. (2.54), we argue that

$$\begin{aligned} \eta_{Canavalin} &= \left(\frac{Sc_{Canavalin}}{Sc_{COM}}\right)^{-1/3} \left(\frac{Da^*_{Canavalin}}{Da^*_{COM}}\right) \eta_{COM} \\ &\approx 0.41. \end{aligned} \tag{2.55}$$

represents the same position for minimum supersaturation on the Canavalin surface.

Finally, we estimate the expected plateau value for the exposed Canavalin surface supersaturation via eq. (2.53) as,

$$\frac{\sigma_{s,Canavalin}}{\sigma_0} = \frac{1}{\eta_{Canavalin} + 1}. \tag{2.56}$$

With $\sigma_0 = 0.5$ and the value of $\eta_{Canavalin}$ from above, $\sigma_{s,Canavalin} \approx 0.36$, which is in excellent agreement with the minimum surface supersaturation away from the cantilever for the Canavalin system, as shown in Figure 2.19.

We employ the same scaling approach to estimate the minimum surface supersaturations for the remaining systems and list their values in Table 2.3. For both the KDP and Lysozyme systems, a minimum surface supersaturation of $\sigma_s \approx 0.10$ is predicted. This correctly predicts the trend of these surface minima being significantly lower than those of COM and Canavalin; however, their predicted values are not as accurate as that obtained for Canavalin.

Surface supersaturation under the cantilever

The crystal surface under the cantilever is not strongly affected by the free-stream flow, since it is largely shielded from it. Unlike the exposed crystal surface discussed above, we do not expect a boundary layer to form, rather we anticipate the geometry of the gap to be important and diffusion to be the dominant mass transfer mechanism. Thus, we expect

that the surface supersaturation under the AFM cantilever to be primarily determined by the interaction between rates of solute diffusion through the liquid and incorporation into the growing crystal.

We have described solute transport to the surface of the growing crystal by eq. (2.23), which contains the two dimensionless groups, Da and c_{eq}/ρ. We first note that typically $c_{eq}/\rho \ll 1$ for these systems (see Table 2.3), so that this boundary condition is well approximated by a simpler expression,

$$-\frac{d\sigma}{dz} = Da\ \sigma, \tag{2.57}$$

where we have taken z to be a coordinate that is directed normal to the crystal surface, scaled with the crystal dimension, L_c, and we have employed the local modified Damköhler number, Da.

If we imagine that δ is the distance of separation between the cantilever and the crystal surface and ignore the effects of convection in this gap (which is equivalent to arguing that diffusion dominates), we approximate eq. (2.57) as

$$-\frac{b-\sigma_s}{(\delta/L_c)} \approx Da\ \sigma_s, \tag{2.58}$$

whee b represents the supersaturation at the position of the overhead cantilever and σ_s represents the supersaturation at the crystal surface.

Solving this approximate equation yields

$$\sigma_s \approx \frac{b}{\delta/L_c + Da}, \tag{2.59}$$

showing that the surface supersaturation is inversely correlated with the modified Damköhler number.

In reality, solute transport will not be one-dimensional across the gap between cantilever and crystal, and we expect cross-diffusion from adjacent regions. Thus, we do not expect b to be strictly constant for all cases. Nevertheless, we argue that it may not change significantly between the COM and Canavalin systems and that eq. (2.59) implies

$$\frac{\sigma_{s,Canavalin}}{\sigma_{s,COM}} \approx \frac{\delta/L_c + Da_{COM}}{\delta/L_c + Da_{Canavalin}}. \tag{2.60}$$

If we assume that $\delta/L_c = 0.5$, this relation provides an estimate of the minimum supersat-

uration of $\sigma_{s,Canavalin} = 0.17$ on the crystal surface under the cantilever, thus predicting a lower value than that for COM, which is consistent with the finite element results.

We employ the same scaling approach to estimate the minimum surface supersaturations under the cantilever for the remaining systems and list their values in Table 2.3. The values for the KDP and Lysozyme growth systems are predicted to be substantially less than the COM and Canavalin systems and agree reasonably well with those from the computations.

As a final consideration, we note that these simple scaling analyses provide insight to the ordering of the supersaturation profiles and, perhaps most interestingly, the switch in ordering between COM and Canavalin supersaturation minima between the outer, exposed crystal surface and the region under the cantilever. A representation of this behavior is provided in Figure 2.21. For the under-cantilever case described in this section, Figure 2.21(a) schematically depicts the concentration profiles across the gap between cantilever and crystal surface for the two systems. The modified Damköhler number, Da, for Canavalin is greater than that for COM, indicating that surface kinetics are more important with respect to diffusion in this system than in the COM growth system and leading to a smaller surface supersaturation for the Canavalin system.

Figure 2.21(b) portrays the situation for the crystal surfaces away from the cantilever and exposed to the flow of solution. Here, there is an interplay among diffusion, surface kinetics, and fluid flow. The different hydrodynamic characteristics of the COM and Canavalin systems lead to very different thicknesses of the concentration boundary layers. Even though Canavalin has faster surface kinetics, which leads to lower σ_s when diffusion dominates (as in the under-cantilever case), its concentration boundary layer is only half as thick as that for the COM case. With a smaller diffusion layer, the Canavalin system is limited less by mass transfer than the COM case and exhibits a correspondingly higher value of surface supersaturation.

2.3.4 Surface supersaturation for different Da

To expand our understanding, we perform additional finite element computations of solute supersaturation distribution for modified Damköhler numbers ranging from $Da = 0.12$–120, holding all other parameters constant. Physically, this would correspond to keeping the same flow in the cell, keeping all physical properties and dimensions constant, except for changing only the kinetic coefficient of the crystal, β. Surface supersaturation profiles, plotted along the crystal centerline, are shown for these additional cases in Figure 2.22.

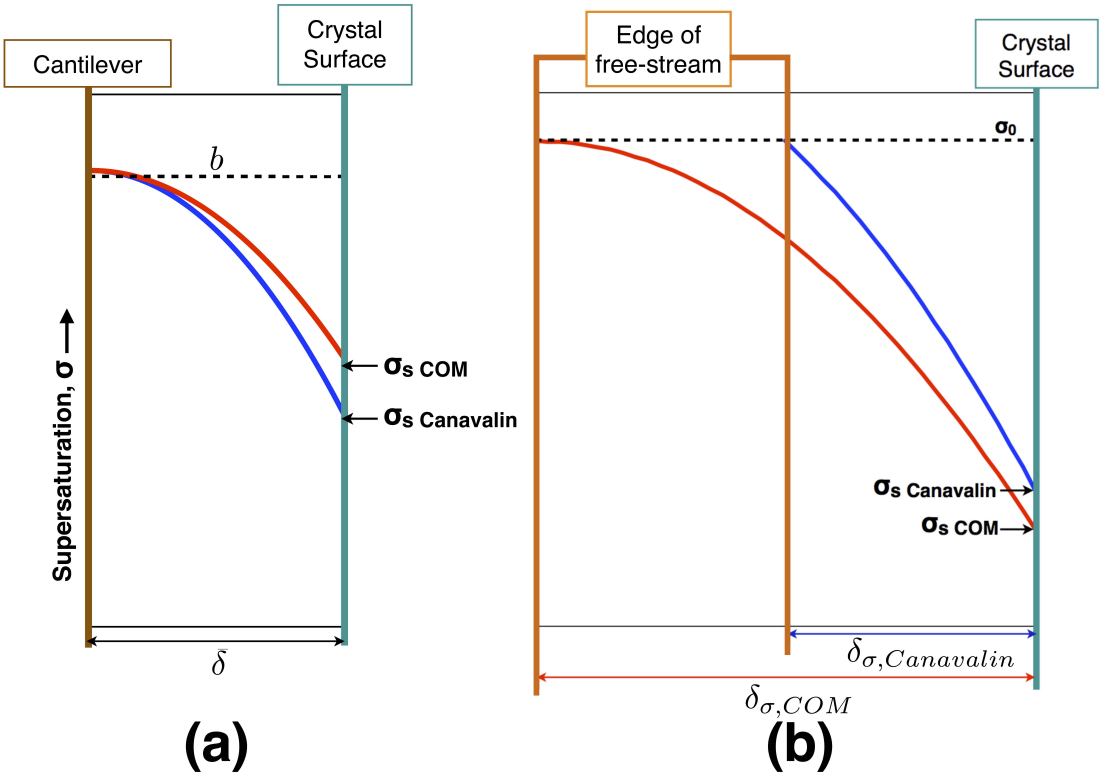

Figure 2.21: Schematic diagrams indicate the different supersaturation profiles in the liquid above the growing crystal, as explained by the scaling analyses presented in text. (a) Solute diffusion effects are considered to dominate under the cantilever, and the higher value of *Da* for Canavalin leads to greater surface depletion. (b) Away from the cantilever, flow is important and the larger boundary layer above the COM crystal increases mass transfer resistance compared to that for the Canavalin system, which results in lower COM surface supersaturation.

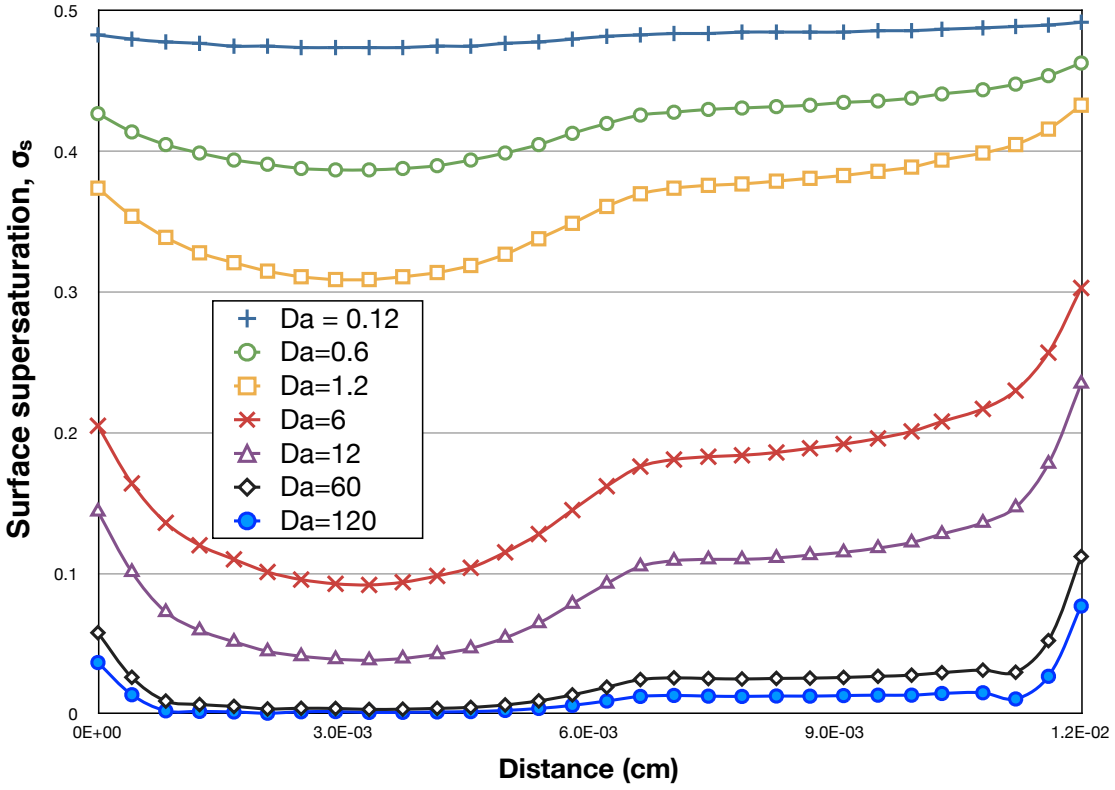

Figure 2.22: Surface supersaturation profiles for growth systems with different values of *Da* are plotted along the center of the crystal surface. The extent of surface depletion increases with *Da*.

Similar to the prior results shown in Figure 2.19, we see that σ_s is highest at the crystal edge away from cantilever and lowest under the center of the cantilever. Consistent with the interpretation of the modified Damköhler number as a ratio between the rates for diffusion and that for crystallization, the results for $Da \ll 1$ show that the level of surface supersaturation is not strongly affected by mass transfer limitations and is not significantly different from the inlet supersaturation level of $\sigma_0 = 0.5$. On the other hand, the results for $Da \gg 1$ indicate that mass transfer limits the diffusion of solute to the rapidly crystallizing surface, so the surface supersaturation is much lower than the inlet values. For $Da \gtrsim 100$, the surface concentration approaches zero, and growth is limited by the rate at which solute can diffuse to the surface of the crystal. The surface supersaturation profiles change most strongly with modified Damköhler numbers that are near unity, $Da \approx 1$, where diffusion and growth are strongly coupled.

2.3.5 Experimental measurement interpretation

Knowing the level of solute depletion under the AFM tip is important for the proper interpretation of any AFM measurement of crystal growth kinetics. Specifically, a typical experiment may directly measure crystal growth rate, V_n, as a function of supersaturation. In ensuing analyses of data, one would be tempted to make a plot of V_n versus the nominal value of different values of the inlet supersaturation, σ_0. The slope of a line fitted through these data could be interpreted as the kinetic coefficient for growth, β, via the classical relationship,

$$V_n = \beta\sigma. \tag{2.61}$$

However, it is quite clear from the prior calculations that the actual value of the surface supersaturation in the vicinity of the scanning tip, σ_s, could be dramatically lower than the nominal supersaturation, σ_0.

We can estimate the error invoked by ignoring mass transfer limitations as follows. If we simply compute the kinetic coefficient using inlet supersaturation,

$$\beta_{observed} = V_n/\sigma_0. \tag{2.62}$$

However, a more fundamental interpretation of the kinetic coefficient is derived via the

relationship,

$$\beta_{true} = V_n/\sigma_s. \tag{2.63}$$

Thus a measure of the relative error is given by

$$\frac{\beta_{true} - \beta_{observed}}{\beta_{true}} = \frac{\sigma_0 - \sigma_s}{\sigma_0}. \tag{2.64}$$

Since σ_s is always less than σ_0 due to mass transfer effects, the true value of the kinetic coefficient, β_{true}, will always be larger than its value calculated using inlet supersaturation, $\beta_{observed}$.

Toward estimating the error caused by ignoring mass transfer limitations in an AFM measurement of a growing crystal, we plot the relative error for the prior simulations as a function of *Da* in Figure 2.23. We compute the relative error based on the surface supersaturation, σ_s, at the center of the crystal, corresponding to the location of the measuring tip of the AFM. Figure 2.23(a) summarizes results from three different set of simulations. Results from the first four materials systems are shown as open squares. The cases discussed in the prior section, for different Damköhler numbers (holding all other factors constant), are indicated by the open circles. A third data set, shown as filled diamonds, is also included in the figure and plots results from additional simulations of COM growth. In these calculations, three crystal sizes, 10, 120, and 180 μm, are simulated by remeshing the domain, with all other physical dimensions and parameters kept constant. Figure 2.23(b) zooms in on these data, focussing on outcomes for the systems with smaller relative error and smaller Damköhler number.

Unlike the discussion of the relative minima fully under the cantilever and far away from it, where scaling arguments could be employed for analysis, the AFM tip is in a transition zone between the limiting behaviors of boundary-layer and diffusion control. Thus, the curves presented in Figure 2.23 are not a universal representation of AFM measurement error. Nevertheless, these results clearly indicate that relative error is strongly affected by the modified Damköhler number. The effects of flow are evident for the cases of Lysozyme, Canavlin, and KDP in Figure 2.23(a). All of these materials have a higher Schmidt number than Sc_{COM}, the value used for the *Da* simulations. In accord with the scaling of eq. (2.51), these three materials have thinner boundary layers and less mass transfer resistance. Thus, their relative errors are all somewhat less than that of the *Da* cases (open circles connected by curve).

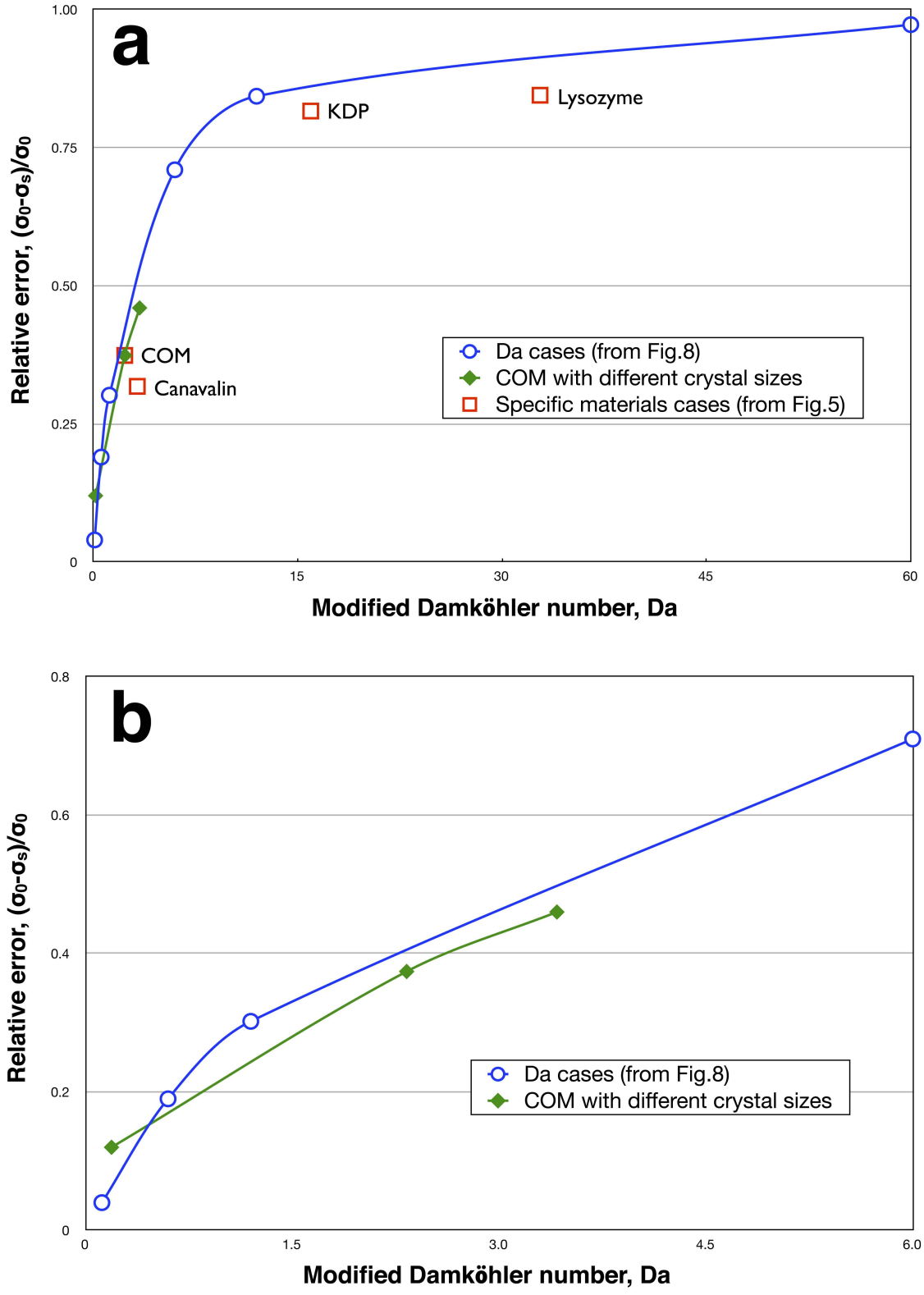

Figure 2.23: Relative error, defined by the change between inlet supersaturation, σ_0, and surface supersaturation, σ_s, at the center of the crystal (underneath the AFM tip) plotted as a function of modified Damköhler number, *Da*, for the different cases considered here.

The results plotted in Figure 2.23(b) can also be understood by flow effects. Reiterating, the Da cases of open circles were conducting changing the Damköhler number alone. For the COM cases with different crystal sizes (filled diamonds), L_c was changed, thus affecting both the local Damköhler and Reynolds number. For these systems, a different Reynolds number changes the thickness of the boundary layer, again per eq. (2.51), thus affecting mass transfer to the surface. This is particularly evident for the cases of smallest Da, where the COM system with a smaller crystal (filled diamond) and smaller Reynolds number, is more limited by mass transfer (due to a thicker boundary layer), thus exhibiting greater relative error than the COM-like system (open circle) with a much larger crystal (but with comparable value of Damköhelr number).

2.4 Summary

We have presented high-fidelity, three-dimensional finite-element computations of flow and mass transfer that arise during AFM measurements of crystals growing from supersaturated liquids. Our results show that supersaturation levels vary considerably over the crystal surface due to coupled effects of solute diffusion, crystal growth kinetics, and solution flow. In particular, depletion at the crystal surface could lead to large errors in the interpretation of kinetic coefficients measured by AFM experiments if such effects are not considered.

Two limiting cases of solute depletion on the crystal surface are well described by relatively simple analyses. Away from the AFM cantilever, flows over and crystallization at the surface result in depletion boundary layers. In these areas, surface supersaturation steadily decreases downstream from the leading edge and is well described by classical boundary layer theory. Under the cantilever, the surface is mostly shielded from solution flow, thus diffusion through the liquid dominates and supersaturation reaches its lowest level over the entire crystal surface. In this case, the behavior is well represented by consideration of the balance between diffusion and surface incorporation, as expressed by the modified Damköhler number, Da

Unfortunately, conditions under the measuring tip of the AFM are neither flow- nor diffusion-dominated, so the simple scaling analyses applied here are not strictly applicable. We expect, in general, that values of σ_s under the AFM tip will be both material and system dependent (i.e., dependent upon cell and cantilever geometry and flow characteristics). However, the results presented here do provide some insight.

For all systems, mass transfer limitations become much more significant as $Da \gtrsim 1$, with supersaturation levels on the surface approaching vanishingly small values for $Da \gtrsim 100$.

If such mass transfer limitations are ignored, significant errors are possible in interpreting AFM measurements of solution crystal growth. Repeating the definition of modified Damköhler number, $Da = \rho_c \beta L_c/(Dc_{eq})$, we see that the only parameter in this group that is not a physical constant is the size of the crystal, L_c. Thus, mass transfer limitations will always be less important for measurements on a smaller crystal.

Increasing the effects of flow will also ameliorate mass transfer limitations by decreasing the thickness of the solute boundary layer during AFM measurements of growing crystals. For a given material, the Schmidt number is fixed, so the only operational parameter available to decrease the boundary layer thickness, per the scaling defined by eq. (2.51), is increasing the Reynolds number via increasing the solution flow rate through the cell. However, the effectiveness of this strategy is likely to be limited, since there may be significant shielding of the crystal surface from the flow caused by the AFM cantilever, as pointed out in the prior computations of Gasperino *et al.* [50].

A rough guide for estimating the difference between the true value of supersaturation on the crystal surface and the inlet supersaturation in an AFM measurement is given by the plots in Figure 2.23. However, we emphasize that these measures are based on results from the specific system simulated here and should not quantitatively be applied to determine errors in other systems. For unambiguous interpretation of AFM data and self-consistent evaluation of fundamental properties, such as kinetic rate constants, a detailed numerical approach, such as that undertaken here, may be needed to "model the measurement" in order to quantitatively ascertain the extent of surface solute depletion.

While our results clarify the role of mass transfer limitations during AFM measurements of solution crystal growth, there may be other phenomena that also impact surface supersaturation levels. For example, nearby crystals, especially upstream of the crystal being imaged, may deplete the solution of solute and further lower the surface supersaturation over the effects considered here. Cantilever geometries that change the shielding of the crystal surface from solution flow may also change the mass transfer behavior in these systems. Finally, scanning effects, such as tapping mode or fast stage movement for high-speed scanning, may alter flows near the crystal surface and subsequently influence mass transfer; preliminary computations of such flows have been carried out by Gasperino [52]. Analyses such as those presented here will be of great utility for understanding and potentially correcting for these effects.

Future work

Nowadays, a fast scanning technology isimplemented in AFM measurement. This technology enables the real-time three-dimensional-observation in AFM at high resolution, and is employed in many area of research and studies [6, 105, 148]. The scanning rates of fast-scanning AFM can be over 100 times faster than conventional AFM. As stated in Section 2.2, our simulations are based on a quasi-steady-state assumption. This assumption is valid because the time scale for mass transport near the crystal (in the order of $1s$) is much smaller than the time scale of normal crystal growth (on the order of $1h$). However, accompany the new fast scanning technology, the AFM fluid cell scanning speed would become much higher and the scanning motion timescale would become comparable to or even smaller than the transport timescale. In this case, to represent the transport and crystal growth condition in a fast scanning AFM fluid cell, this scanning motion needs to be taken into account and a tangent model is required.

We perform preliminary study on momentum transport in a simplified geometry in still fluid to understand the impact of scanning frequency on velocity field, and the results are shown in Figure 2.24. As we can see, when scanning rate is relatively slow (at $10Hz$), the scan introduced flow is laminar and flow streamlines are parallel to crystal surface. When scanning frequency increased to $400Hz$, the scanning motion generated vortex flow and the flow pattern becomes more complicated. This preliminary result shows that the scanning motion does have huge impact on fluid flow, especially at high scanning rate. The mass transport will be greatly affected by fast scanning motion as a result, and a transient model is needed to fully understand this impact.

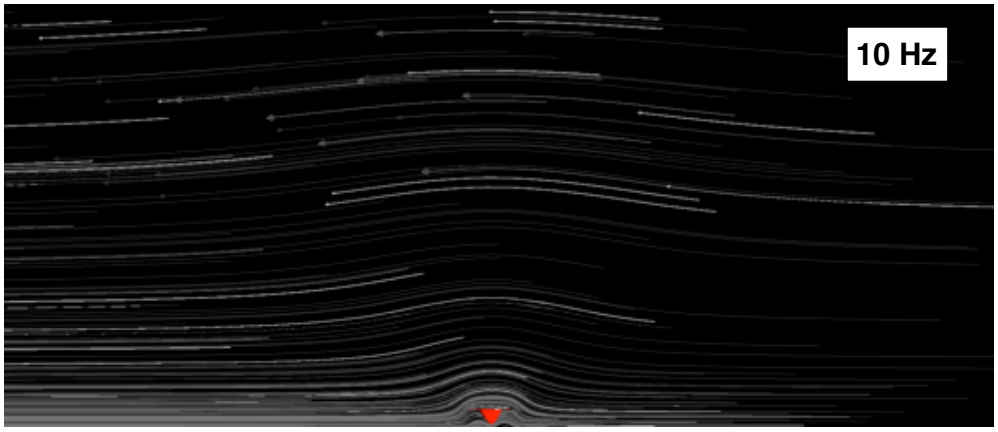

(a)

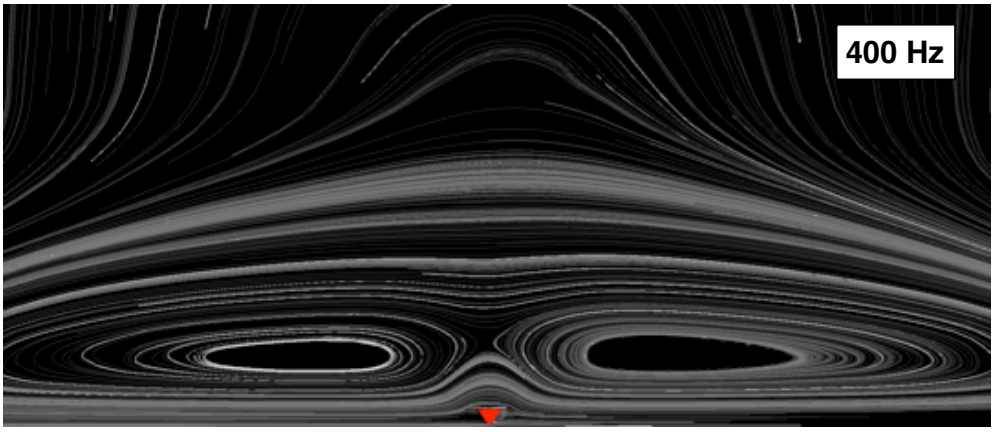

(b)

Figure 2.24: Simulated streamline of flow on a clip plan that passes through AFM scanning tip, and is perpendicular to crystal surface and cantilever. The red triangle at bottom center represents the AFM tip. Figure (a) represents the simulation result when AFM scanner is scanning at the frequency of $10Hz$, while Figure (b) represents the result when the scanning frequency is $400Hz$.

Chapter 3

Phase-Field Analysis in of Nanowire Growth Systems

In this chapter, we apply phase-field method based spiral growth model and island growth model to simulate nanowire crystal growth in solutions. We employ ZnO nanowire growth system as a model system for this study because of the sufficient experimental data available for this growth system. With the simulation results and comparison with experimental observations, we provide discussions about whether phase-field method is a useful tool to model nanowire growth conditions.

3.1 Introduction of Zinc Oxide Nanowire Grown from Aqueous Solution

Zinc oxide (ZnO) is an inorganic $II - VI$ compound. ZnO crystals exist in three forms, which are hexagonal wurtzite, cubic zincblende, and cubic rocksalt. Among them, the hexagonal wurtzite crystal structure is most stable and common, and the ZnO discussed in this thesis is in this type of microstructure.

In materials science, ZnO is a direct wide band gap ($3.3ev$) semiconductor material. ZnO exhibits near UV emission and transparent conductivity as a result of the band gap structure, and is widely applied on optoelectronic devices such as solar cells [10,11], sensors [144], and light emitting diodes [70]. ZnO is naturally a n-type semiconductor materials. Recently with the p-type doping ZnO successfully prepared [62], ZnO becomes one of the most popular materials in semiconductor industry, because ZnO is inexpensive, relatively

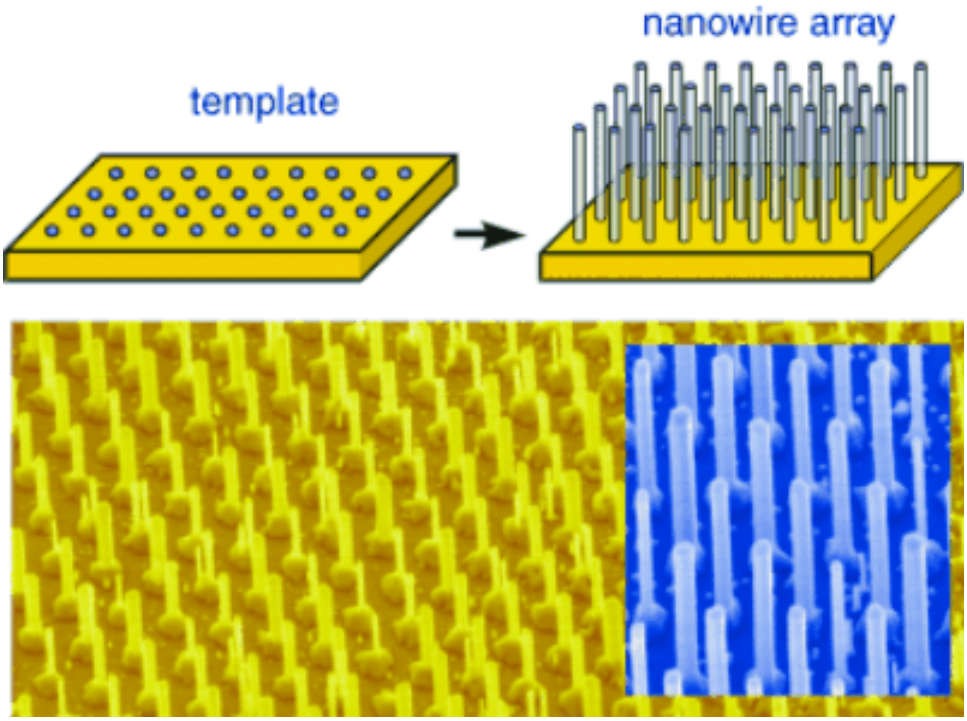

Figure 3.1: Position-controlled fabrication of semiconductor nanowires arrays. [44]

.

abundant, stable, nontoxic and easy to prepare. Additionally, because of it's band gap structure, ZnO has higher breakdown voltage, so it is able to sustain large electric fields. Furthermore, it has lower electronic noise, and is suitable for high-temperature and high-power operation.

Nowadays, with the modern nano-technology, ZnO nanowires gained considerable research interest. In this section, we present an overview of ZnO nanowires and their growth kinetics in aqueous solution.

3.1.1 Overview of ZnO nanowires

Nanowires arrays can be fabricated either with self organization or controlled assembly. Nowadays, people have successfully fabricated position-controlled nano-patterns of semiconductor nanowire arrays [44]. Fig. 3.1 shows a schematic of how these arrays are assembled by patterning the substrate, and these substrates can be prepared with lithographical stamping methods [124].

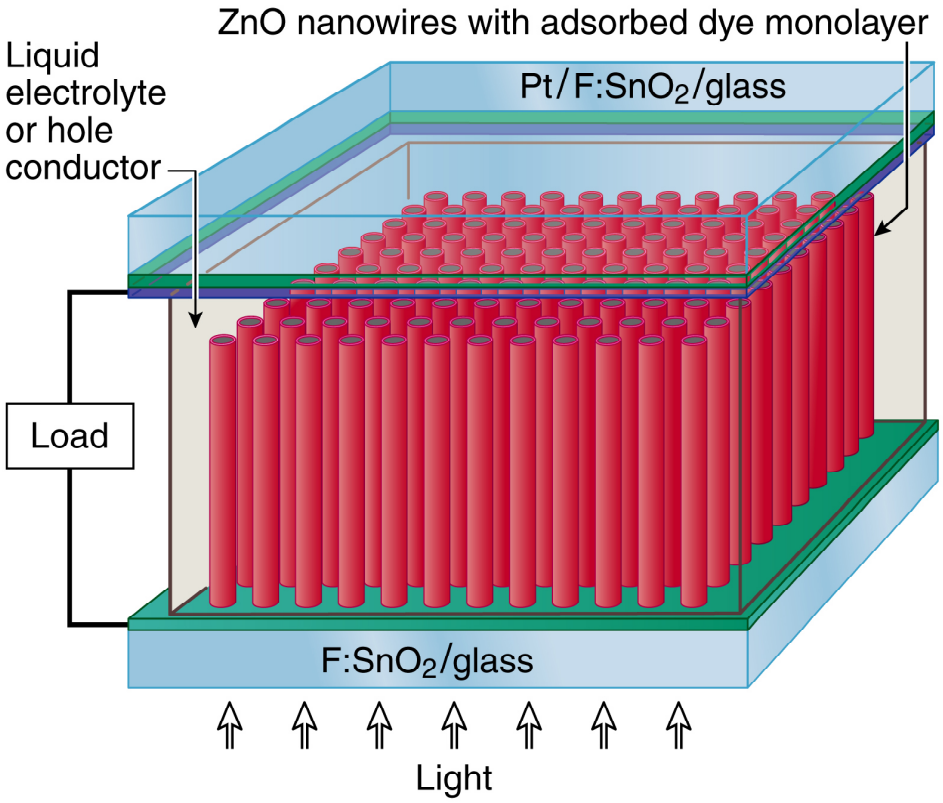

Figure 3.2: Schematic diagram of the nanowire-based DSSC [10]

.

Among the potential semiconductor nanowires materials, ZnO nanowires become very popular. Long and thin ZnO nanowires are relatively easy to make than other materials, because they grow in highly preferred $< 0001 >$ direction. Additionally, ZnO nanowires arrays can be easily transferred by stamping method [45].

ZnO nanowires arrays show many potential applications in optoelectronics, catalysis, sensing, and energy conversion [109,131]. For examples, in area of energy conversion, ZnO nanowires arrays has been used in nanogenerators because of their piezoelectric and semiconducting properties [132]; in optoelectronics field, they have been used as the photoanode in dye-sensitized solar cells (DSSC) [10,76].

DSSC is a low-cost thin film solar cell. It is composed of a semiconductor thin film between a photo-sensitized anode and an electrolyte. This cell was invented by Michael Gratzel and Brian O'Regan in 1991 [92]. This cell is technically attractive because it is made of low-cost materials, and no complex equipment is required. Additionally, it is me-

chanically flexible and can be built into soft sheets. Initially, semiconductor nanoparticles thin films were used in DSSC. With this mesoporous nanoparticles film, the electrolytic solution penetrates in between the nanoparticles, and forms a large semiconductor-dye-electrolyte interface area, which leads to large charge conversion efficiency. However, the electron transfer efficiency is low in these films, which is because when electrons in the semiconductor diffuse through the nanoparticles films, these electrons need to pass through hundreds of inter-particle hopping steps [125,126]. As a result, the numerous nanoparticles boundaries in these films limit electron transport [123]. E. Aydil *et al.* recently developed a nanowires array based DSSC, and a schematic diagram of this cell is showed in Fig. 3.2 [10]. This nanowire based DSSC showed much higher charge collection efficiencies than nanoparticle-based cells, for nanowires provide direct pathways to the electrode. Since ZnO nanowires arrays grown from aqueous solution form dense arrays of long nanowires oriented normal to the substrate surface [10], ZnO nanowires have been used as the photoanode in this nanowire-based DSSCs [10, 76]. However, the overall energy conversion efficiency of this nanowire-based DSSC is still significantly lower than that of typical nanoparticle-based DSSC due to the lower surface area of nanowires in comparison to nanoparticles. Therefore, there is need for engineering arrays of thinner and taller nanowires. To fulfill this need, fundamental understanding of ZnO nanowires growth kinetics is required.

3.1.2 ZnO nanowire growth kinetics

ZnO nanowires are normally synthesized from aqueous solutions. E. Aydil *et al.* fabricated ZnO nanowire arrays from the solution of zinc nitrate hexahydrate and methenamine on seeded SnO_2 transparent conducting substrates [10]. Fig. 3.3 represents SEM images of ZnO nanowires arrays grown from this aqueous solution. As we can see, these ZnO nanowires form dense arrays of long wires.

During the growth of ZnO nanowires from aqueous solution, evidence of spiral growth and island growth was observed on the (0001) face during different experiment stages. As shown in Fig.3.4, during the early stage when the supersaturation is high, island growth mechanism was observed, while during the late stage when the supersaturation is low, spiral growth mechanism was observed.

We revealed how crystal growth in solution in Section 1.1.2. The factor differentiating stable nuclei from unstable ones is the critical size. This size mainly depends on supersaturaion of adjacent solution. Nuclei larger than the critical size are prone to grow. Otherwise, the nuclei are likely to diminish. During the early stage of the ZnO growth,

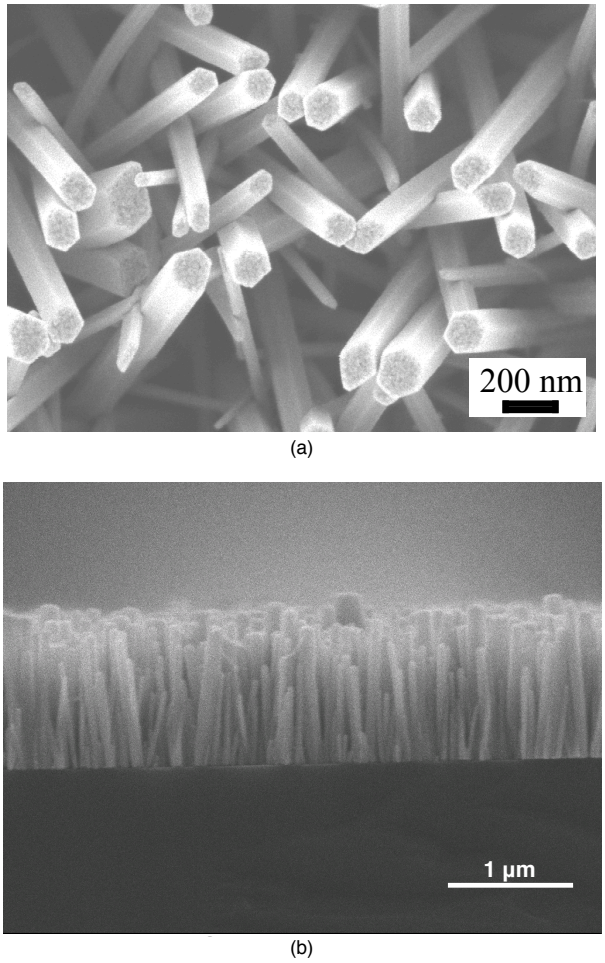

Figure 3.3: (a) Top view SEM image of ZNO nanowires arrays grown for 1h. (b) Cross-sectional SEM image of ZnO nanowire arrays grown for four cycles. [10].

supersaturation is high and the critical size reduces. As a result, newly formed nuclei on ZnO nanowire top surface are predominantly stable. Molecules attach to the kink sites along nuclei walls and these nuclei expend and grow. This growth mechanism is called island growth. During the late stage of ZnO growth, supersaturation is low, the critical size becomes large, and the nucleation barrier is difficult to overcome. Accordingly, there's no nuclei walls for molecules to attach to. Instead, surface molecules would attach to kink sites along the step dislocation on a ZnO nanowire top surface. These steps elongate like a spiral, the raised terraces expand, and a nanowire grows taller. This growth mechanism is called spiral growth, or Burton, Cabrera and Frank (BCF) mechanism. To fully understand these two growth kinetics, information about nanowires surface supersaturation, surface mass transport, and bulk mass transport, and how they affect the growth mechanism and nanowires microstructure is needed. Unfortunately, these effects are very difficult to obtain experimentally, and numerical modeling of this system could fulfill this need. We examine modeling solutions to study these two kinetics, and details will be discussed in following sections.

J. Boercker *et al.* studied the macro-scale bulk mass transport limitation during the nanowire arrays growth with a one-dimensional numerical model [17]. They discovered that the growth of ZnO nanowires in aqueous solutions was mass transport limited, and the growth rate was inversely dependent on the nanowire density. Their results showed that this transport limitation led to nonuniform nanowire length across the substrate, but this limitation could be overcome by stirring the solution near substrate. This macro-scale study revealed how bulk mass transport would affect the growth. However, no information about the growth kinetics was provided. As a result, a study on the surface scale, which is also called the meso-scale, is needed. In this chapter, we apply a phase-field based meso-scale model to study the dynamics of the spiral growth and island growth on a single ZnO nanowire top surface. In this model, we couple step motion, 2-D nucleation and surface mass transport to represent growth of a single ZnO nanowire, so as to study the growth kinetics of both island growth and spiral growth mechanisms.

3.2 Model Formulation

3.2.1 Introduction to phase-field method

In this section, a meso-scale computational model based on phase-field method is presented for transient study on spiral growth and island growth of a vicinal ZnO nanowire top

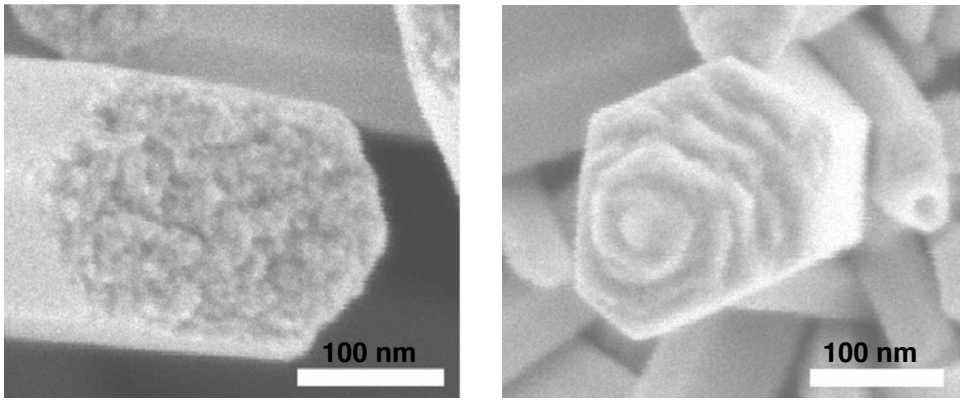

Figure 3.4: High magnification SEM images of a nanowire top surface, the (0001) face, revealing spiral growth mechanism as showed in (a) and island growth mechanism as showed in (b) [10].

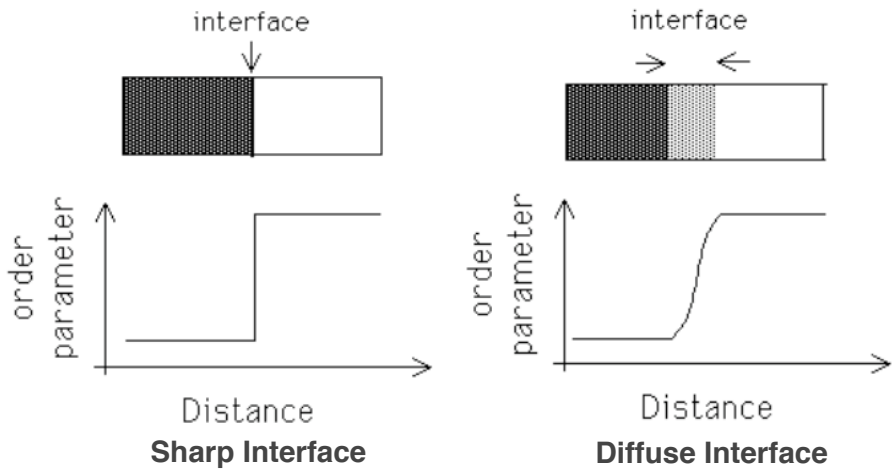

Figure 3.5: Difference between sharp interface and diffuse interface.

surface from solution. In this study, we focus on crystal growth on the top surface of one single ZnO nanowire. We assume ZnO precursor is consumed by heterogeneous reactions on this surface. In other words, there's no reation in solution and no lateral growth on ZnO nanowire walls. In addition, we assume that the growth units behave similarly to ZnO molecules. We incorporate the transport of solute on the crystal surface with the adsorption and desorption of solute molecules in this model, and study the spiral growth and island growth mechanisms with two associate models.

We introduce phase-field method in our model to simulate ZnO nanowire growth. Phase-field method is a mathematical technique based on thermodynamics describing the process of phase transition. In this method, the state of the microstructure is represented continuously by a single variable known as the order parameter, or more commonly, the phase-field parameter (ϕ). One of the distinguishing characteristics of the this approach is that the interface between phases is diffuse. The difference between sharp interface and diffuse interface is shown in Figure 3.5. In crystal growth model, this interface represents steps between terraces.

We implement phase-field method to the study of ZnO nanowire growth because this method provides time-dependent tracing of each individual step, and no moving mesh is involved, which saves calculation cost. As stated in previous section, both island growth mechanism and spiral growth mechanism involve step progress. Therefore, this time-dependent tracing of steps with low simulation cost is promising and encouraging for our

research.

3.2.2 Governing equations

Spiral growth model formulation

A phase-field method based model is developed to study the spiral growth mechanism with no nucleation when solution supersaturation is low. We address this mechanism first, because the model simulating spiral growth mechanism involves surface mass transport and step advancing, while the model simulating island growth involves surface mass transport, step advancing and nucleation. In other words, island growth model is the spiral growth model with a nucleation add-on.

In the spiral growth model, we assume critical size is so big that no nucleus is stable and crystal is growing only through spiral growth mechanism. This model is derived from the Burton, Cabrera, and Frank (BCF) model [21]. This model incorporates both solute transport on crystal surface and step progression. It is assumed that when solute molecules adsorbed on the crystal surface, they would diffuse on this vicinal surface until they incorporate into steps or desorb back into the solution phase. Hence the mass balance of free solute molecules on the crystal surface includes surface diffusion of adsorbed solute molecules, the total mass flux from the solution phase, and the step growth:

$$\frac{\partial \sigma_s}{\partial t} = \mathcal{D}_s \boldsymbol{\nabla}^2 \sigma_s + F - \Phi, \tag{3.1}$$

where σ_s is the dimensionless surface supersaturation of free solute molecules and is given by $\sigma_s = \Omega(c_s - c_{eq})$, where Ω is the atomic area of the solid crystal, and c_{eq} is the equilibrium concentration on the surface. The physical meaning of σ_s is the number of supersaturated solute molecules per atomic area. $\mathcal{D}_s$ represents the surface solute diffusion coefficient. Φ is related to the free molecules loss due to the step growth which is correlated with the incorporation of molecules to the steps. Detailed definition of Φ is given in the "Phase-field Formulation" section. F represents the total mass flux to the crystal surface as indicated in Figure 3.6 (a). The flux term, F, which includes both the adsorption and desorption of solute molecules can be defined as:

$$F = k_{ads}\sigma_b^0 - k_{des}\sigma_s. \tag{3.2}$$

where k_{ads} and k_{des} are the adsorption rate constant in length per time and desorption

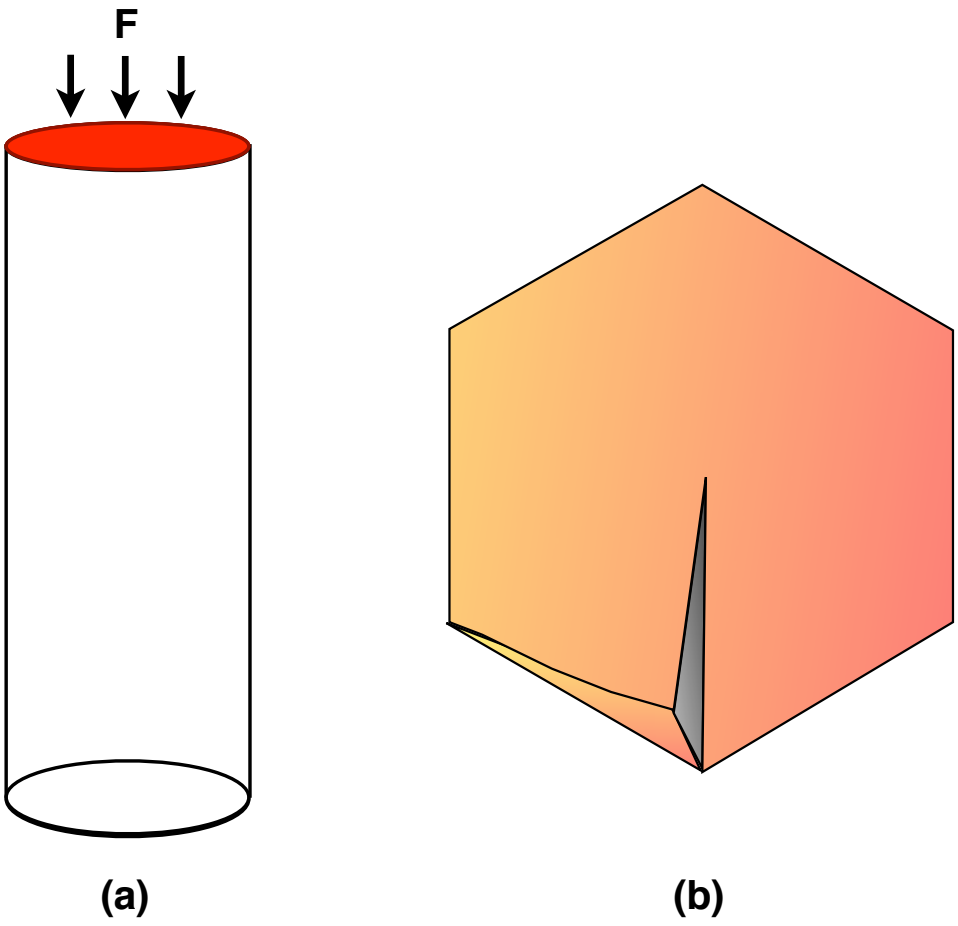

Figure 3.6: (a) We focus on the top surface of a single ZnO nanowire, and F indicates the mass flux rate transport to this top surface. (b) A screw dislocation originating from surface center is introduced as the initial condition.

rate constant, and σ_b^0 is the bulk solute supersaturation in the solution phase evaluated at the surface. Typically $k_{des} \ll k_{ads}$, so we assume $k_{des} = 0$. In other words, we assume ZnO nanowires grow under the desorption-free condition in our system.

To illustrate the geometry of ZnO nanowire top surface, a hexagon domain is used as shown in Figure 3.6 (b). As the requirement for spiral growth to initiate, a single screw dislocation is introduced as the initial condition. Surface molecules diffuse and attach to kink sites along this dislocation. This step then advances like a spiral, and the nanowire grows taller as a result. As mentioned in the beginning of this section, we assumed that all ZnO precursors are consumed by heterogeneous reactions on this top surface. Accordingly, no-flux boundary condition is applied at all six edges of this domain as:

$$\mathbf{n} \cdot \boldsymbol{\nabla} \sigma_s = 0, \tag{3.3}$$

indicating that no excessive molecules diffuse out of or into the domain.

Phase-field formulation

To represent the step formation term, and furthermore to simulate the evolution of steps, phase-field method is applied to reformulate Eq. (3.1) based on the model presented in [81] and [96]. In our model, the value ϕ represents the height of the crystal surface above the initial substrate surface. ϕ is in the unit of $2h_s$ where h_s is the height of a single step. Usually, h_s is the height of a single crystal unit cell in the growth direction. Odd integer values of ϕ correspond to the surface positions of terraces. Even integer and non-integer values of ϕ are associated with the locations of the moving steps, which are of a finite step width.

The evolution of ϕ with time is proportional to the variation of a hypothetical free energy $\mathcal{H}$ [69]:

$$\tau_\phi \frac{\partial \phi}{\partial t} = \frac{\partial \mathcal{H}}{\partial \phi}, \tag{3.4}$$

where,

$$\mathcal{H}(\phi) = \int_V \left(\frac{\omega^2}{2} (\boldsymbol{\nabla}\phi)^2 + \frac{1}{\pi} \cos[\pi(\phi - \phi_s)] + \lambda \left((\phi - \phi_s) + \frac{1}{\pi} \sin[\pi(\phi - \phi_s)] \right) \sigma_s \right) dV. \tag{3.5}$$

In Eq. 3.5, ϕ_s represents the reference substrate surface, and its value is assigned with

the initial condition. For different initial surface conditions in our simulations, ϕ_s varies. We'll provide more details regarding ϕ_s when we discuss initial conditions. The term $\frac{1}{\pi}\cos[\pi(\phi-\phi_s)]$ in this equation is a multi-well potential [68] whose minima are associated with odd integer values of $\phi(x,t)-\phi_s$, corresponding to terrace positions. The term $(\phi-\phi_s)+\frac{1}{\pi}\sin[\pi(\phi-\phi_s)]$ in this equation increases monotonically, and satisfies that with odd integer values of $\phi(x,t)-\phi_s$ (on terraces positions) this term returns the value of $\phi(x,t)-\phi_s$ [93, 129]. Accordingly, this second term is associated with the local number of solid layers above the reference plane and represents the local height of the crystal above the reference surface.

The phase-field evolving equation is derived from Eq. 3.4 and coupled with the solute mass balance equation (Eq. (3.1)) to form our governing equations. We nondimensionalize the governing equations by domain size L as the characteristic length, and the characteristic diffusion time scale L^2/D_s as the characteristic time, and the dimensionless form of our governing equations can be written as:

$$\frac{\mathcal{D}_s\,\tau_\phi}{\omega^2}\frac{\partial\phi}{\partial t} = \boldsymbol{\nabla}^2\phi+\frac{L^2}{\omega^2}\{\sin[\pi(\phi-\phi_s)]+\lambda\sigma_s\{1+\cos[\pi(\phi-\phi_s)]\}\}, \tag{3.6}$$

$$\frac{\partial\sigma_s}{\partial t} = \boldsymbol{\nabla}^2\sigma_s+\frac{L^2}{\mathcal{D}_s}F-\frac{1}{2}\frac{\partial\phi}{\partial t}. \tag{3.7}$$

In Eq. 3.6, τ_ϕ is a mobility parameter which reflects the response rate of the phase field, ω is associated with the finite width of the moving step, and λ is the coupling parameter and is related to the step energy. We will provide more details about τ_ϕ, ω and λ in Section 3.2.4. The last term Φ in Eq. 3.1 which represents the mass loss of free molecules due to step growth can be represented as $\frac{1}{2}\frac{\partial\phi}{\partial t}$ in Eq. 3.7.

A single screw dislocation is introduced as the initial condition as shown in Figure 3.6(b). This initial condition is transferred into phase-field formulation as: $\pi\phi_s = \arctan(y/x)$ [68].

Island growth model formulation

As presented in Section 3.1.2, island growth kinetics consists of molecule surface diffusion, nucleation, and molecule incorporation into nucleus wall (step progression). As stated in previous section, our spiral growth model incorporates molecule surface transport as well as step advancement. Therefore, we develop the island growth model based on the spiral growth model by adding the nucleation component, and the governing equations become:

$$\frac{\mathcal{D}_s\,\tau_\phi}{\omega^2}\frac{\partial\phi}{\partial t} = \boldsymbol{\nabla}^2\phi + \frac{L^2}{\omega^2}\{\sin[\pi(\phi-\phi_s)] + \lambda\sigma_s\{1+\cos[\pi(\phi-\phi_s)]\}\} + 2\lambda_n{\sigma_s}^{i+1}, \tag{3.8}$$

$$\frac{\partial\sigma_s}{\partial t} = \boldsymbol{\nabla}^2\sigma_s + \frac{L^2}{\mathcal{D}_s}F(\delta) - \frac{1}{2}\frac{\partial\phi}{\partial t}. \tag{3.9}$$

Compared to the spiral growth phase-field evolving equation (Eq. 3.6), the term $2\lambda_n{\sigma_s}^{i+1}$ is included in Eq. 3.8 to represent surface nucleation rate [152]. The number 2 stems from our ϕ unit setting, which is $2h_s$. In this model,

$$\lambda_n = \mathcal{D}_s \exp[-Ea/kBT], \tag{3.10}$$

where Ea represents the bonding barrier for the island nucleation on the crystal surface. λ_n is in the order of 1, and we use $\lambda_n = 1$ in our simulations. i in Eq. 3.8 represents the number of molecules needed for a nucleus to reach critical size. In our studies, we assume that a single molecule can serve as a stable nucleus, as a result of the sufficient dangling bonds available on the surface, and we assume $i = 1$ accordingly. This assumption serve as a good starting point to qualitatively study the island growth on nanowire top surface. However, this assumption may not be valid due to the complicated ambient condition around the nanowires in solutions. In reality, the number of atoms forming a stable 2D nucleus need to be calculated from Gibbs-Thomson nucleation theory. To obtain quantitative understanding of island growth mechanism during nanowire growth, further study on i and the impact of i is needed.

Also, in the island growth governing equations, the total mass flow term F in Eq. 3.7 becomes a stochastic flow $F(\delta)$ in Eq. 3.9 by introducing a stochastic function δ. As a result, instead of uniformed flow to the surface, solute molecules are adsorbed to the surface at random position on every time interval. One doubt existing with this stochastic term is that this numerical term, although logical, may not be physically realistic. Further investigation is needed to justify this stochastic flow employment.

We study island growth under two different initial conditions. First, we assume a flat surface as $t = 0$ by setting $\phi_s = 0$. Then we study the island growth with a screw dislocation on top surface by assigning $\pi\phi_s = \arctan(y/x)$ to investigate the interaction between island growth and spiral growth.

3.2.3 Numerical method

Finite element method

As we stated in Section 2.2.2, the essence of Finite Element Method (FEM) is to divide the given computational domain into smaller subdomains, which are called the finite elements. Finite elements together with the partitioned computational domain as a whole is called the finite element mesh. These elements in the mesh are defined by points called nodes. In finite element method, we try to determine the values of the unknown variables at these nodes, which, along with the underlying local interpolation functions, will give us an approximate solution at any point inside the computational domain. More details about FEM are described in Section 2.2.2.

Time integration

As mentioned, this phase-field method based model is a transient model, and time integration is involved. We introduce a forward time-step calculation to solve this transient problem. To solve unknowns at each forward time-step, a second-order accurate Implicit Trapezoid Rule (TR) with fixed time step (h) is used. Particularly, TR is unconditionally stable (A-stable) when the corresponding ODE is stable, and it has the smallest local truncation error coefficient of all second-order A-stable methods. A-stability is a requirement that all numerical solutions generated by a numerical integration method (with arbitrary time step satisfies the equation $\frac{dx}{dt} = \lambda x$, $Re\lambda < 0$) is strictly asymptotically stable.

3.2.4 Implementation

In this section, we provide detailed information regarding the implementation of our models, including the definition and values of the parameters and properties used in our simulations, and the finite element mesh information.

Parameters and properties

As mentioned in Section 3.2.2, the phase-field model parameters used in our model are τ_ϕ, ω, and λ. τ_ϕ represents the response time of the phase field, ω represents the finite width of the moving step, and λ is the coupling parameter and is related to step energy. Value of these parameters can be determined with the thin interface limit analysis [69] according to the following relationships:

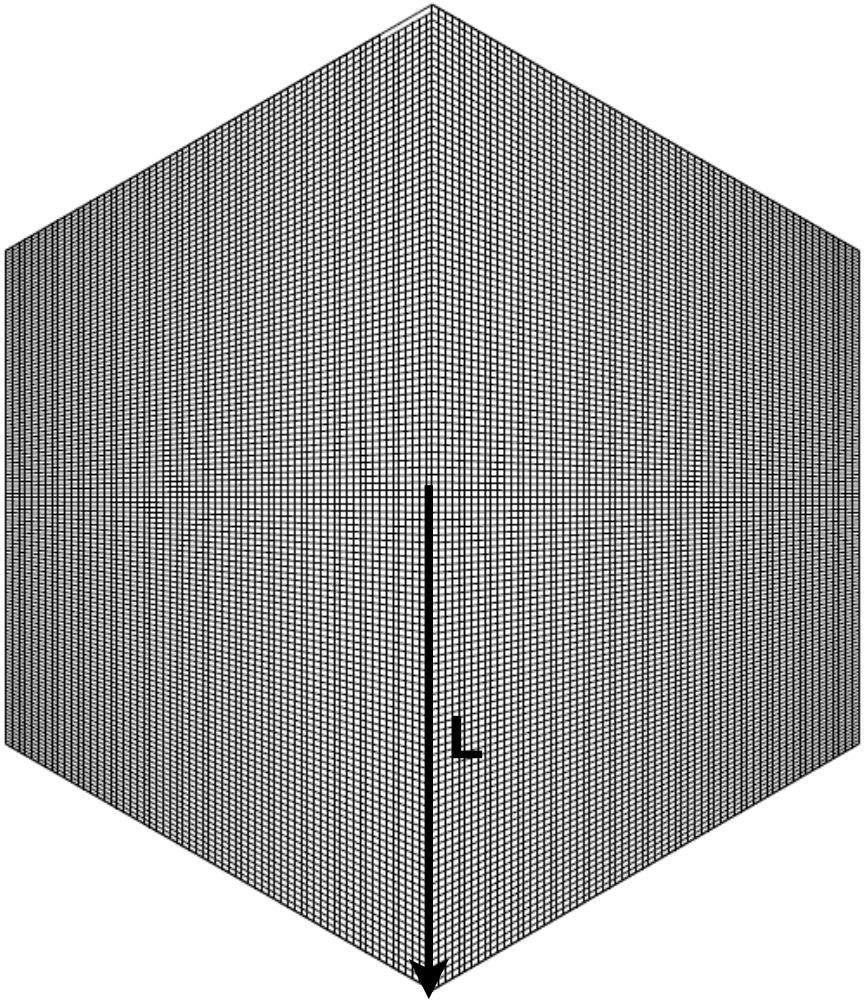

Figure 3.7: Computational domain of the ZnO nanowire top surface. $L = 30nm$

$$\frac{1}{\beta} = a_1(\frac{\tau_\phi}{\lambda\omega} - a_2\frac{\omega}{\mathcal{D}_s}), \tag{3.11}$$

$$d_0 = a_1\frac{\omega}{\lambda}. \tag{3.12}$$

$a_1 = 0.72$ and $a_2 = 0.51$ are both numerical constant [68] , β is the interface kinetic coefficient, $\mathcal{D}_s$ is surface diffusivity, and d_0 is the capillary length. This capillary length is defined as $d_0 = \Omega^2 c_{eq}\gamma/k_BT$, where γ is the step stiffness and is associated with step energy.

In the simulations of ZnO nanowire growth, β goes to infinity which represents instantaneous attachment of molecules at steps, ω is chosen to be $10^{-8}cm$ which is at the same order as the size of a ZnO crystal unit cell, $\mathcal{D}_s$ is chosen to be $10^{-6}cm^2/s$ which is in the same order as of ZnO diffusivity, Ω is chosen to be $10^{-15}cm^2$ to represent average-sized atoms, and γ is chosen to be $0.1ev$ to represent typical hexagonal wurtzite step energy and d_0 becomes $10^{-9}cm$ as a result. With these chosen values, we get $\tau_\phi = 3.7 \times 10^{-10}s$ and $\lambda = 7.2$ according to Eq. 3.11 and Eq. 3.12.

Finite Element Mesh

We implemented FEM to solve the phase-field method based governing equations. Our finite element mesh is shown in Figure 3.7. In the computational domain, we choose the radius of ZnO nanowire to be $30nm$, which is the typical size observed in ZnO growth experiment [10].

3.3 Results and Discussion

3.3.1 Base case for spiral growth

We first simulate the spiral growth kinetics on ZnO nanowire top surface with the spiral growth model provided in Section 3.2.2. Physical properties and system parameters used in this simulation is listed in Table 3.1.

We start our study with a low flow condition, and the total flux to the ZnO top surface is chosen to be $F = 10^{-9}mol/cm^2s$, which is an approximate flow value calculated based on experimental conditions reported in Baxter *et al.* [10]. Results of this simulation are shown in Figure 3.8. In this figure, ZnO top surface is colored by ϕ, which represents terrace height. We plotted the simulated ZnO top surface at different time point. This

Table 3.1: Physical properties and system parameters used to model ZnO nanowire growth.

Parameter	Value	Units
Crystal radius, L	3.00×10^{-6}	cm
ZnO surface diffusivity, D_s	1.00×10^{-6}	cm^2/s
Total mass flux, F	1.00×10^{-9}	mol/cm^2s
Phase-field response time, τ_ϕ	3.67×10^{-10}	s
Step width, ω	1.00×10^{-8}	cm
Coupling parameter, λ	7.20	1

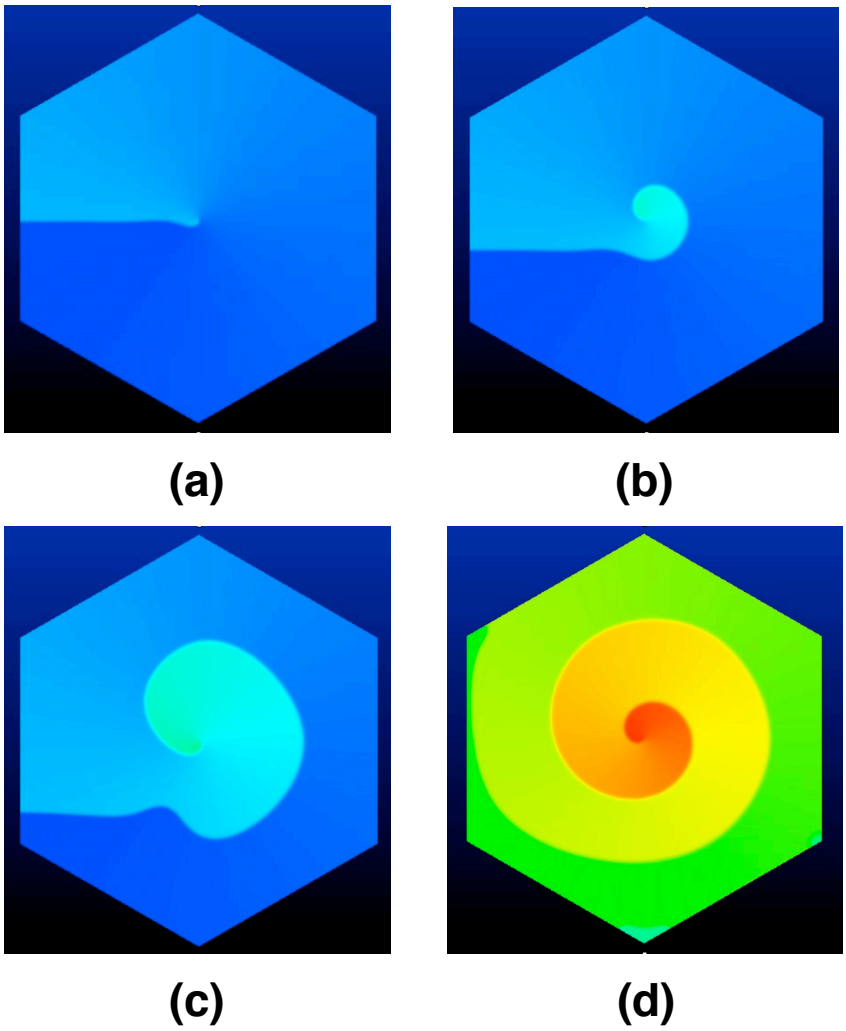

Figure 3.8: Simulated ZnO top surfaces at different time point. These surfaces are colored by ϕ which represents terrace height. Figures in (a), (b), (c) and (d) represent the simulated ZnO surfaces at $t = 2 \times 10^{-4}$, $t = 0.1$, $t = 0.2$ and $t = 4$ in non-dimensional timescale respectively.

figure reveals how ZnO nanowire grow from the initial condition, and exhibits how spiral forms from a step dislocation. We know that a step advances at the same speed under certain growth condition, indicating that the linear speeds at all locations along this step dislocation are the same in our simulation. As a result, the angular speeds at different locations along this step would be different. The closer to the center the location is, the higher the angle speed would be at this location. Therefore, the center proceeds faster than the edge, and a spiral forms. (d) in this figure represents the simulated surface when the spiral is in steady state (step width doesn't change with time). As we can see, compared to the big spiral in figure (c), the step width in figure (d) is much smaller. According to our observation, spirals evolve to steady state by reducing the spacing far from the core and homogenizing the terrace width. As we can see, at steady state (shown in (d) of Figure 3.8), topography of the simulated ZnO top surface agrees with that of the experimentally observed ZnO surface (shown in (b) of Figure 3.4), and terrace width in this simulation is at the same order as experimental observation. This evidence validated this spiral growth model and the system parameters we are using.

In (b) and (c) of Figure 3.8, we can see that the step line is not smooth, while the line smoothens in (d) of this figure. This non-smoothness is due to simulation error with initial time steps, and this error is washed away with time. In this case, this error has no impact on the steady state result. We found this simulation error related to time step length. For this particular low flow simulation shown in Figure 3.8, the time step length is chosen to be $h = 2 \times 10^{-5}$ in non-dimensional timescale. Choosing a smaller time step can solve this initial time steps error.

3.3.2 Impact of higher growth rates

To better understand the spiral growth mechanism of ZnO nanowires, we investigate both local and overall surface supersaturation (σ_s) profile on the ZnO nanowire top surface, and the impact of bulk supersaturation on growth kinetics. Expecting spiral growth mechanism to happen earlier in the experiment with higher total mass flux than the conditions shown in Figure 3.4(b) and Figure 3.8, we choose $F = 1 \times 10^{-8} mol/cm^2 s$ as the start point of the following research.

With this condition, ϕ and σ_s profiles along the diagonal line is shown in Figure 3.9 (a). The location of this diagonal line is shown in (b) of this figure as a solid blue line. As mentioned in Section 3.2.2, the value of ϕ represents the height of the crystal surface above the initial substrate surface. In this case, the profile of ϕ along the diagonal line

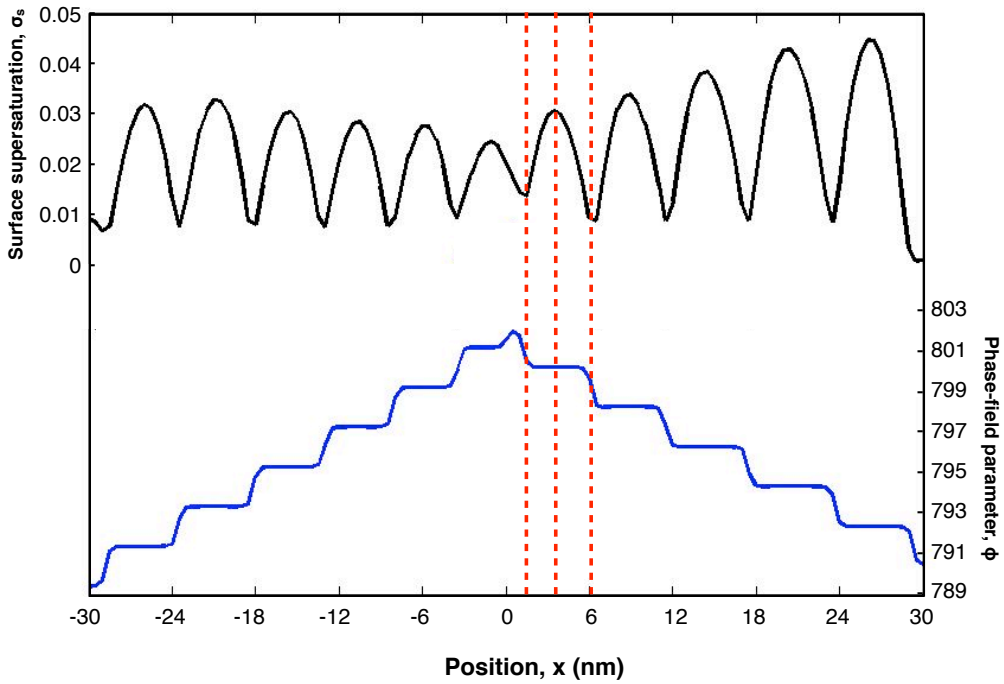

Figure 3.9: (a) Surface supersaturation and phase-field parameter profile along the diagonal line across the domain when $F = 1 \times 10^{-8} mol/cm^2 s$. This diagonal line is shown in (b) as the solid blue line.

can be viewed as a cross-sectional plot of a ZnO nanowire showing terraces shape and height on top surface. In this profile, each flat platform represents a terrace, and the transitions between neighboring platforms represent the steps between adjacent terraces. As we can see, the terraces in the center are higher than those at the edge. This is a result of spiral formation, which agrees with the surface plot in Figure 3.8 and the experimental observation in Figure 3.4.

As illustrated by the red dash lines in Figure 3.9 (a), within each terrace, σ_s reaches its peak at the terrace center and its minimum near the steps. This profile results from the assumption that molecules can't transfer between adjacent terraces. When a growth unit is transported to a terrace surface, it diffuses along this terrace surface until it reaches a step (adjacent to the higher or lower terraces). Due to this no between-terraces transfer assumption, this growth unit incorporates with this step, and this step advances. As a result, σ_s is at its lowest at the step location, and at its peak in the terrace center.

Also based on the σ_s profile in Figure 3.9 (a), we observe that the maximum σ_s at each terrace is higher near the edge and lower near the center of the domain. In other words, global σ_s is higher near the edge than in the center of a nanowire. This behavior is a outcome of the no flux boundary condition. Since steps stop advancing at nanowire edges, and no mass flux flows out of these edges, there is no growth unit consumption at the edges of a nanowire. Therefore, global σ_s is lower at the center than at the edge of a nanowire.

3.3.3 Scaling behavior

With this basic understanding of terrace width, and local and global σ_s distribution, we perform additional computations to investigate how bulk supersaturation (represented by total mass flux F in our simulations) impacts ZnO nanowire growth, ranging F from $F = 1 \times 10^{-9} mol/cm^2 s - 2.5 \times 10^{-7} mol/cm^2 s$ and keeping all other parameters constant.

We first study how total flux F would affect the surface supersaturation. As shown in Figure 3.10, we plot the σ_s profile along the diagonal line with different F. As we can see, higher the total flux results in higher σ_s. This result means that with increased F, the number of free growth unit on the surface increased. This is an important finding. It helps us explain certain growth kinetics which will be provided in the following paragraphs.

Before we introduce more simulation results, we would like to introduce the concept of step velocity. Step velocity is the velocity a step advances in the direction perpendicular to the step line. Like terrace width which was discussed in previous paragraphs, step velocity

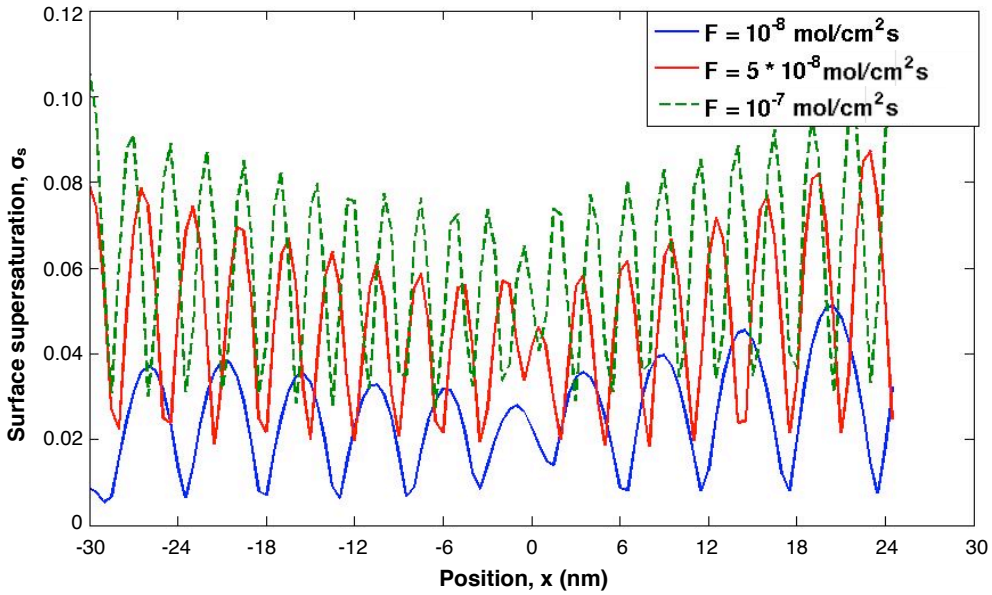

Figure 3.10: Surface supersaturation profiles along the diagonal line across the domain for growth conditions with different value of total flux are plotted.

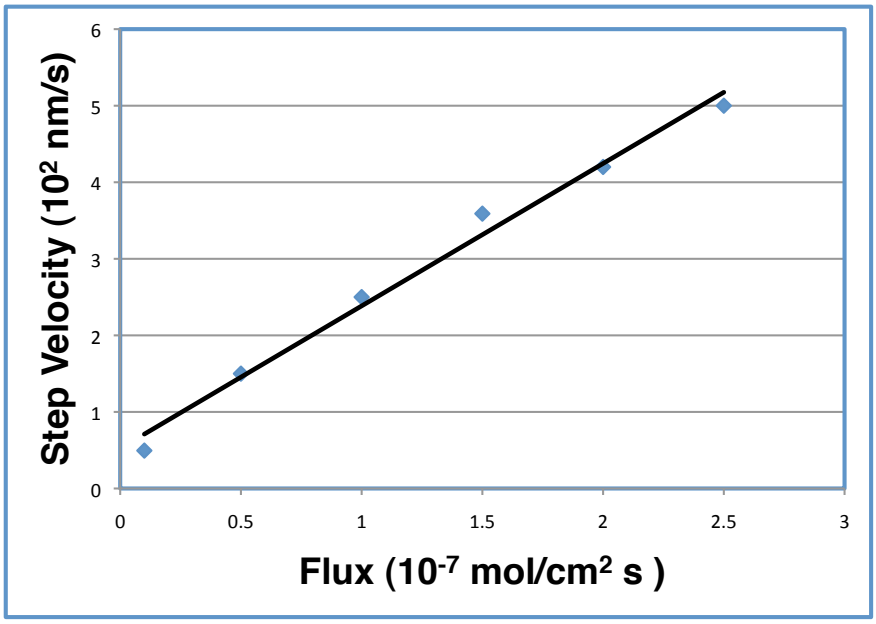

(a)

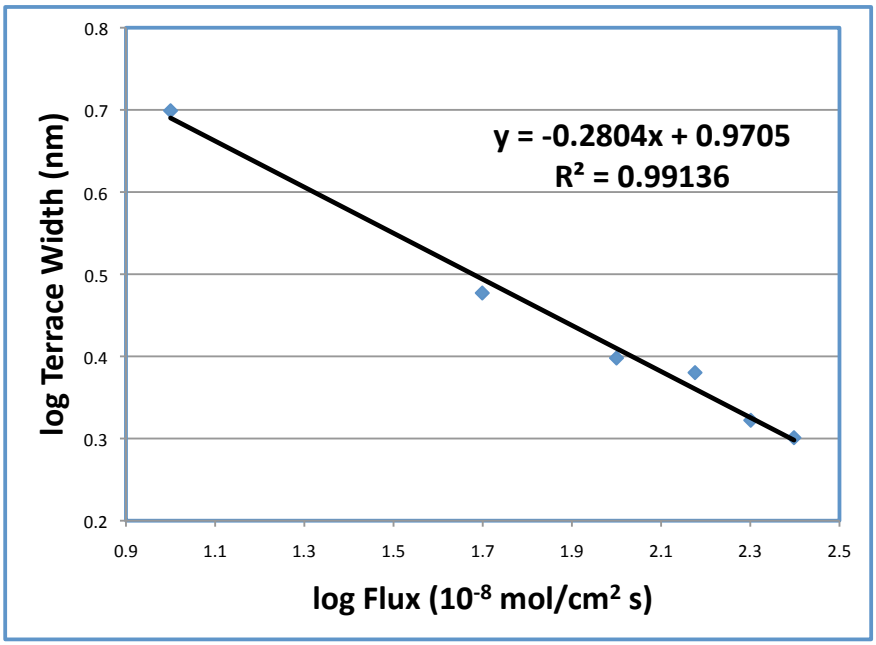

(b)

Figure 3.11: (a) Step velocity versus the change of total flux F in linear scale. (b) Terrace width versus the change of total flux F in log scale.

is also an important parameter determing growth kinetics. For certain growth condition, step velocity and steady state terrace width are both constant.

We plot step velocity and terrace width with the change of F in linear scale and log scale respectively, and the result is shown in Figure 3.11 (a) and (b). As we can see, increased F leads to step velocity increase and terrace width decrease. We anticipate the same trends with the change of bulk supersaturation. These trends are as expected. As shown in Figure 3.10, with increased F, the total free growth units on the surface increased. As a result, the chance for a growth unit to diffuse to and incorporate with a step is higher. Provided that step advancing is a result of incorporation with growth unit, with the increased chance of incorporation, step advances faster, and step velocity increases. As a consequence, the angular speed of the spiral increases, and the spiral evolves faster. In this case, terrace width needs to be reduced further to compensate for this faster angular speed, so it decreases.

In classic scaling theory, Cabrera and Coleman estimated that the mass flux F determines the step velocity(v_∞) and terrace width (l), and v_∞ increases linearly with F while l increases linearly with $F^{-1/3}$ [24]. As can be seen in Figure 3.11, our simulation results show that:

$$v_\infty \sim F, \tag{3.13}$$

$$l \sim F^{-0.28}. \tag{3.14}$$

These results agree well with the Cabrera and Coleman estimation.

Taking a closer look at Figure 3.10, we can see that the global σ_s difference between center and edge is different when the total flux changes. We discern this difference in Figure 3.12 by plotting σ_s profiles under two different flow conditions, and identify the σ_s center-to-edge differences (L_1 in figure (a) and L_2 in figure (b)) in both cases. As we can see, L_1 which is the center-to-edge σ_s difference when $F = 1 \times 10^{-7} mol/cm^2 s$ is obviously larger than L_2 which is this difference when $F = 1 \times 10^{-8} mol/cm^2 s$. As we analyzed before, the global σ_s difference between domain center and edge is a result of the no flux boundary condition and growth unit accumulation at the edge. In this case, when the total flux F (or bulk supersaturation) increases, the growth unit accumulation increases, which results in a higher center-to-edge σ_s difference.

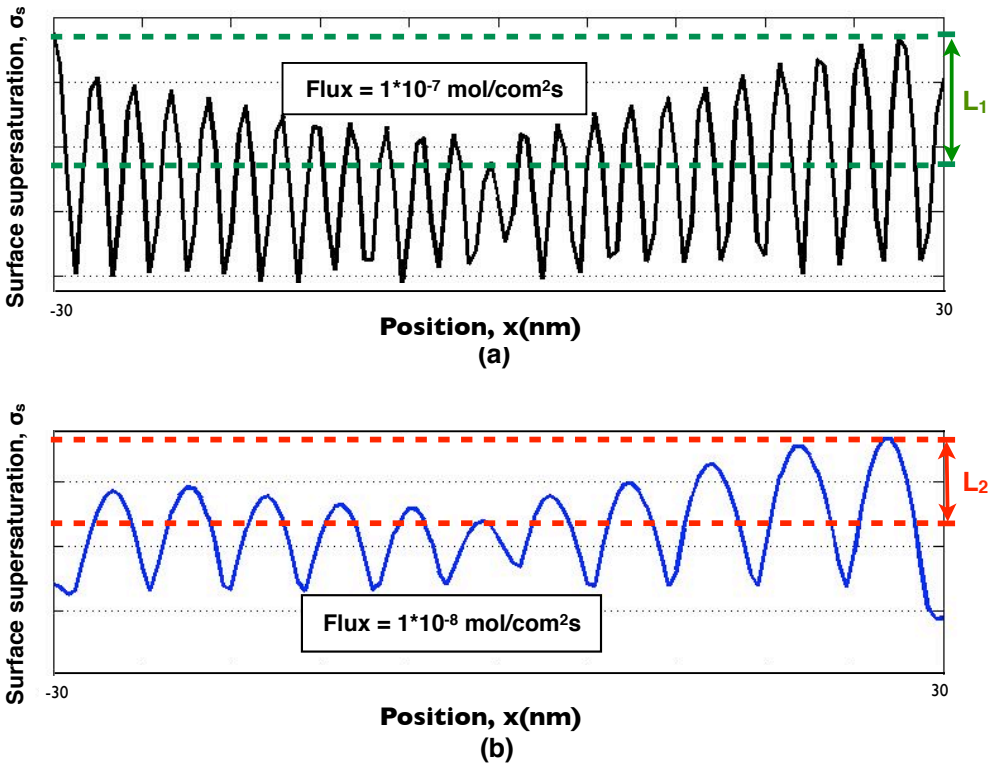

Figure 3.12: Comparison between surface supersaturation differences with different total mass flux. (a) and (b) shows σ_s profiles along the diagonal line across the domain with $F = 1 \times 10^{-7} mol/cm^2 s$ (a) and $F = 1 \times 10^{-8} mol/cm^2 s$ (b). L_1 and L_2 in (a) and (b) represent global σ_s difference across the domain.

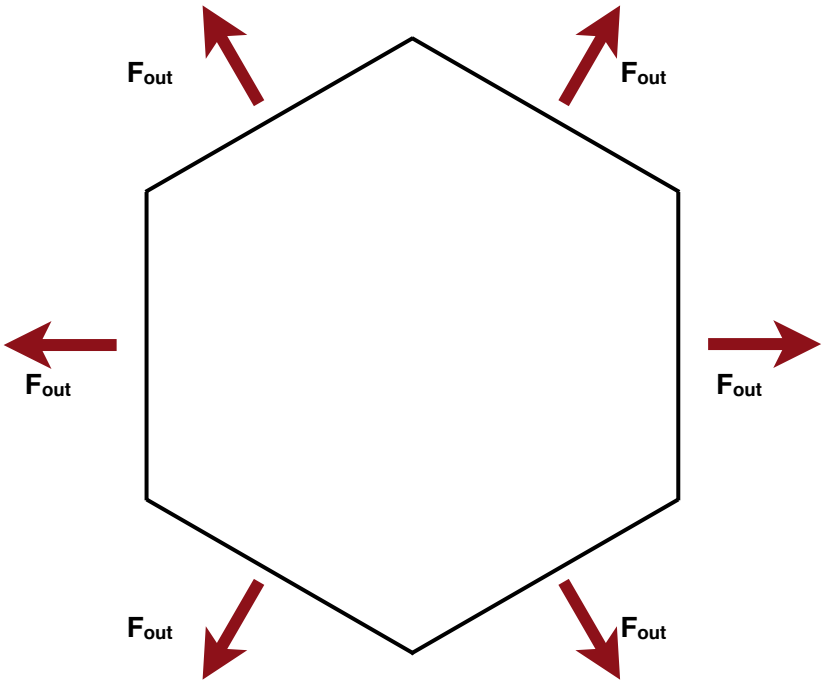

Figure 3.13: Schematic of outward mass flux boundary condition. F_{out} represents the mass flux outward from the domain

3.3.4 Effect of edge flow boundary condition

What would the spiral growth kinetics change when there is a boundary flux out of the the domain? In the case of possible edge transparency and edge detachment, a ZnO nanowire surface boundary with outward mass flux from the domain could be a valid situation. In this case, we modify our boundary conditions and add boundary flux F_{out} to the domain. The direction of F_{out} is indicated in Figure 3.13. As we can see, F_{out} is in the direction perpendicular to the boundary line and outward from the domain.

We perform a simulation with total flux $F = 1 \times 10^{-7} mol/com^2 s$ and boundary flux $F_{out} = 1\%F$. We plot σ_s profiles along the diagonal line both with and without outward boundary flows in Figure 3.14. As we can see, terraces width near the center of the domain remains the same when the outward flux boundary condition is applied, while edge terraces vanishes with this outward flux boundary condition. This boundary flux also causes variation of local σ_s profile. As shown in this figure, when no flux boundary condition is applied at the edges of the domain, the maximum σ_s at each terrace is higher near the edge and lower near the center. When a small outward flux which equals to 1% of the total flux F is applied at the boundary, the value of the σ_s peak near the center of the domain remains unchanged while the peak values of σ_s on terraces near the edge reduce remarkably. With this outward boundary flux, the growth unit accumulation near the domain edge no longer exits. Instead, there's a growth unit consumption near the edge. When this consumption caused by outward flow becomes higher than the growth unit consumption caused by crystal growth, the global σ_s near the edge becomes lower than that near the center.

We plot ϕ profiles along the diagonal line both with and without outward boundary flows in Figure 3.15. As previously mentioned, this profile of ϕ can be viewed as a cross-sectional plot of a ZnO nanowire. In this case, according to Figure 3.15, the ZnO nanowire is straight with constant nanowire thickness with no-flux boundary condition, while this thickness decreases with time with the outward flux boundary condition. In other words, this outward flux results in shrinking of nanowire thickness.

As we can see, a small outward boundary flux (1% of the total flux) leads to different growth kinetics and behavior. Further investigation is required in this topic to fully understand the impact of boundary conditions.

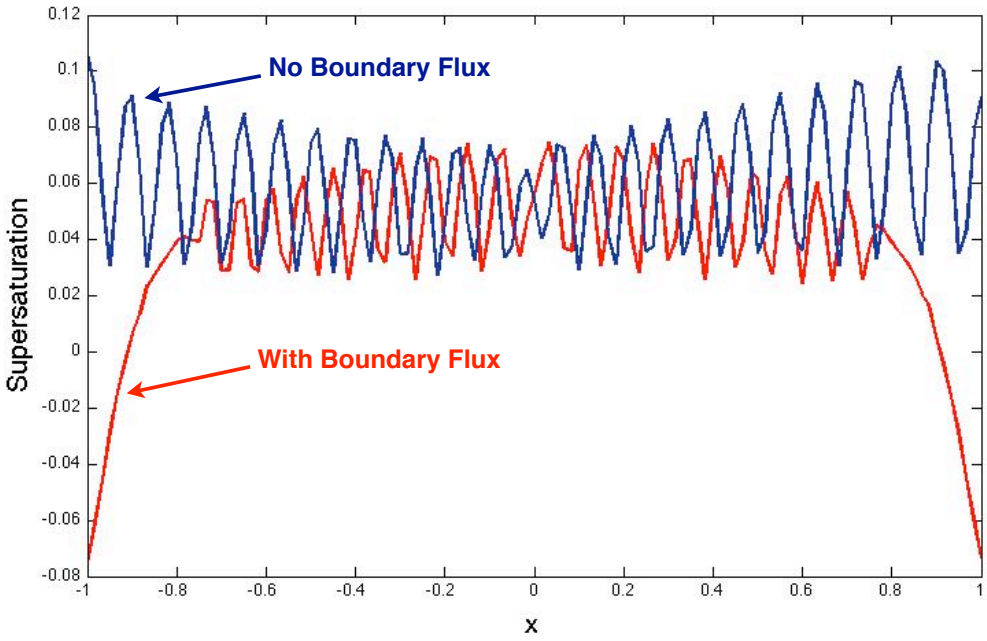

Figure 3.14: Surface supersaturation profiles along the diagonal line across the domain with and without outward boundary flows. Scale of x axis is nondimentionalized by domain radius $L = 30nm$.

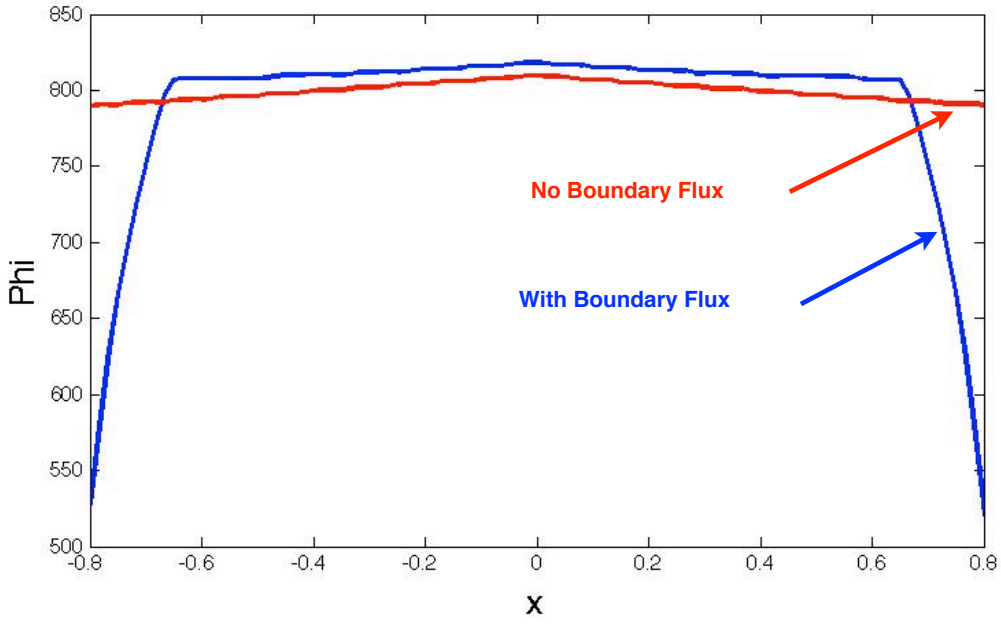

Figure 3.15: ϕ profiles along the diagonal line across the domain with and without outward boundary flows. This profile of ϕ can be viewed as a cross-sectional plot of a ZnO nanowire. Scale of x axis is nondimentionalized by domain radius $L = 30nm$.

3.3.5 Island growth mechanism

As stated in Section 3.1.2, during the early stage of ZnO nanowire growth, evidence of island growth mechanism was observed, while evidence of spiral growth mechanism was observed towards the end when bulk supersaturation was low. We perform simulations to exam the spiral growth mechanism in Section 3.3.1. In this section, we investigate island growth mechanism of ZnO nanowire growth with the island growth model provided in Section 3.2.2. As mentioned, this model couples step advancing (step growth) with growth unit nucleation.

We first perform simulations with no flux boundary condition and with a flat surface as the initial condition.

We study the total mass flux (bulk supersaturation) impact by simulating the nanowire growth with different total mass fluxes by ranging F from $F = 1 \times 10^{-7} mol/cm^2 s - 1 \times$

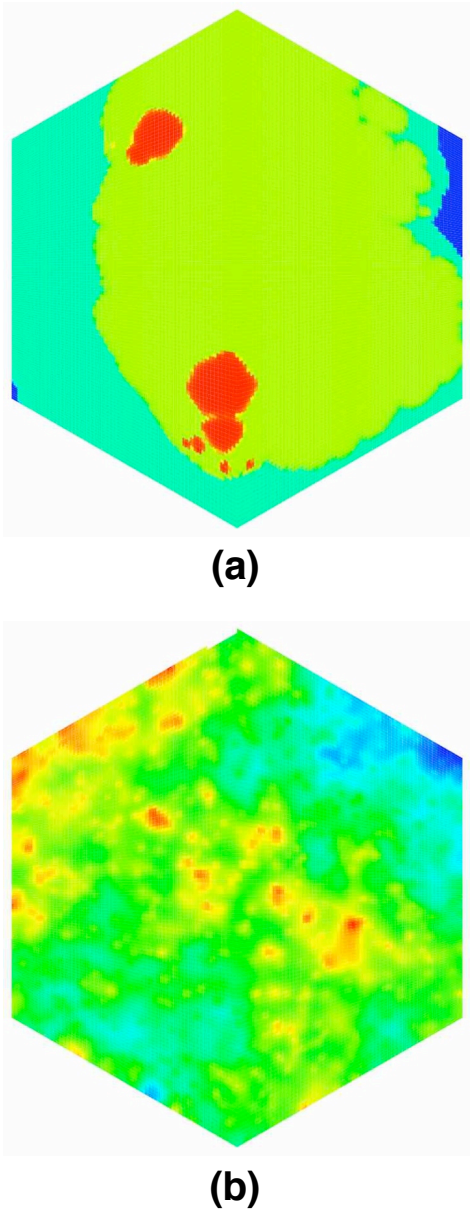

Figure 3.16: Simulated ZnO top surfaces with different total mass flow. These surfaces are colored by ϕ which represents terrace height. Figures in (a) and (b) represent the simulated ZnO surfaces with $F = 1 \times 10^{-7} mol/cm^2 s$ and $F = 1 \times 10^{-6} mol/cm^2 s$ respectively.

$10^{-6}mol/cm^2s$. This flux range covers the total mass flux in the early stage of experiments to the middle stage of experiments. We plot the simulated ZnO top surfaces (colored by ϕ) with different F in Figure 3.16. As shown, in Figure 3.16 (a), in the middle stage of experiments, when F is low, the nucleation rate is low. A few stable nuclei form on the surface, and grow into a plane with step advancing. In other words, when bulk supersaturation is low, the growth process is dominated by step growth. When the total flux F increases, we observe a change of growth kinetics. As shown in Figure 3.16 (b), when F increases to $1 \times 10^{-6}mol/cm^2s$, which represents the high solution supersaturation condition in the early stage of experiments, numerous stable nuclei form and we observe incomplete planes. In this case, ZnO nanowire mainly grow by nuclei formation, and we name this growth state as nucleation dominated. Therefore, according to the simulation results, increased total flux (bulk supersaturation) leads to change of growth dominating factor.

Additionally, the simulated top surface morphology shown in Figure 3.16 (b) shows similarity with experimental observation shown in Figure 3.4 (a). This agreement is consistent with this island growth model.

We then start our simulation with a screw dislocation as the initial condition (this initial condition was described in Figure 3.6). We perform this simulation with total mass flux $F = 1 \times 10^{-7}mol/cm^2s$, and the results are shown in Figure 3.17. This growth process is an incorporation of growth unit nucleation, and step growth from the steps along stable nuclei edges and the spiral line. In other words, this growth is a result of both island growth and spiral evolvement. In this figure, we observe rough edge of steps due to the incorporation of the growing spiral and the growing islands. Besides, by introducing island growth mechanism, we can see that this simulated result show better agreement with experimental observation (shown in Figure 3.4 (b)) compared to the spiral growth only simulation.

In addition, we compare the terrace width of this result and the terrace width in the spiral growth only simulation with the same initial condition and total mass flux. We find that the average terrace width of these two cases are almost the same. In other words, the addition of nucleation and island growth doesn't affect the spiral evolvement, and the spiral angular speed remains the same.

According to our study, by introducing island growth mechanism with the screw dislocation initial condition, simulation results show better agreement with experimental observations. Hence, we can say that the spiral growth mechanism observed in experiments during ZnO nanowire growth is actually an incorporation of both spiral growth and island growth.

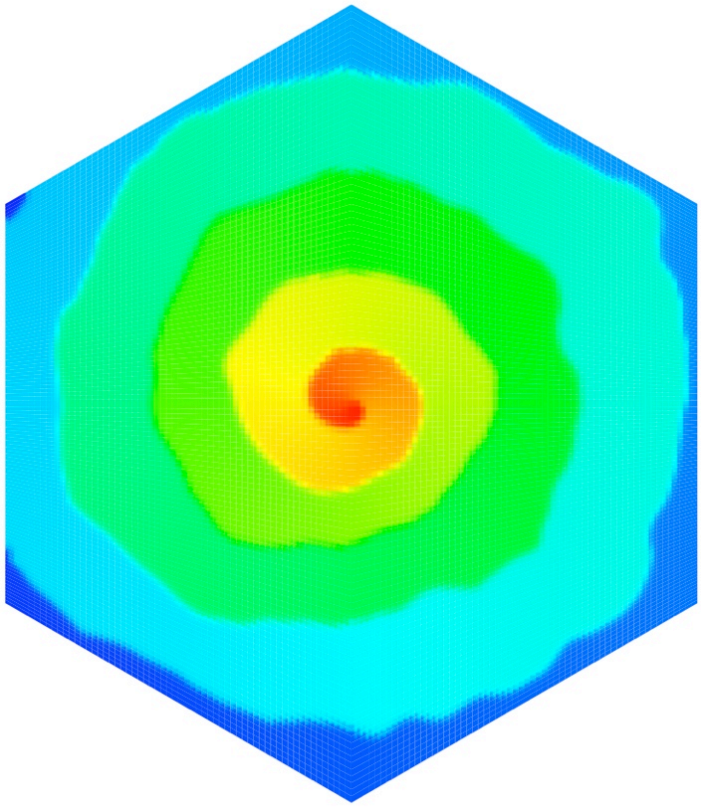

Figure 3.17: Simulated ZnO top surface with a screw dislocation as initial condition with island growth model. This surface is colored by ϕ.

3.4 Summary

In this chapter, we apply phase-field method based models to simulate nanowire crystal growth and employ ZnO nanowire growth as a model system.

We first apply phase-field based spiral growth model to simulate ZnO nanowire growth when supersaturation is low. This model predicts evolution of moving steps and shows agreement with experimental observations. We also clarifies how bulk supersaturation would affect the spiral growth, and our simulated results are consistent with the classic CC estimation theory.

We observe uncertainty in boundary conditions at domain edges. A no flux boundary condition leads to inconsistent local concentration which is higher near the domain edge and lower near the domain center. A leaking outward flux at boundary leads to remarkable change of concentration profile and nanowire thickness.

We then introduce nucleation to the system. This model predicts kinetic roughing and rough spiral edges. These results show qualitative agreement with experimental data.

As we can see, these phase-field based models show qualitatively similar behaviors compared to experimental observations. However, these models contain parameters that are not well characterized, especially in the nucleation model. As a result, simulation results of these models must be carefully evaluated before they can be used to quantitatively predict actual nanowire growth.

Chapter 4

Conclusion and Discussion

In this thesis, we apply numerical models to analyze crystal growth processes in solution. Our work in this thesis consists of two parts, each focusing on different scales of solution crystal growth.

First, we provide a macro-scale fluid dynamics model to study solution crystal growth systems in AFM fluid cells. This work focuses on flow and mass transfer during crystal growth, and their impact on crystal growth conditions. A parallel, three-dimensional finite element model is applied to compute fluid flow and mass transfer during crystal growth in AFM fluid cells. Based on our simulation results, surface supersaturation considerably varies over the crystal surface during AFM measurements. This is a result of flow and diffusion limitations caused by AFM cantilever location and geometry.

Two limiting cases of solute depletion on the crystal surface are well described by relatively simple analyses. Away from the AFM cantilever, surface supersaturation steadily decreases downstream from the leading edge and this behavior is well described by classical boundary layer theory. Under the cantilever, the crystal surface is mostly shielded from solution flow, thus supersaturation reaches its lowest level over the entire crystal surface. In this case, the supersaturation change is well represented by consideration of the balance between diffusion and surface incorporation, as expressed by the modified Damköhler number, Da.

As we can see, if mass transfer effects are ignored, significant errors are possible in AFM measurements of solution crystal growth, since surface supersaturation underneath cantilever can be significantly lower than bulk supersaturation. By modeling crystal growth during AFM measurement, we provide a method to assess these errors.

Next, we apply phase-field method based models to simulate nanowire crystal growth.

This work focuses on micro-scale spiral step growth and island growth kinetics on crystal surfaces during growth and on understanding the correlation between island growth and spiral growth mechanisms. We employ ZnO nanowire growth as a model system.

We first study spiral growth mechanism. Our model predicts spiral evolution and simulated results agree with experimental observations. We investigate how bulk supersaturation would impact the nanowire growth. We observe that global surface superstation increases with the increase of bulk supersaturation. Step velocity of spiral growth increases while terrace width decreases with the increase of bulk supersaturation. Our simulated results and correlations agree with the classic scaling theory. We then investigate boundary conditions applied at edges of the domain. Depending on whether or not edge transparency and edge detachment exist, either an outward leaking flow boundary condition or a no flux boundary condition could be valid. A no flux boundary condition leads to inconsistent local concentration. A leaking outward flux at boundary leads to considerable change of concentration profile and nanowire thickness. Further investigation on this topic is needed to fully understand the boundary impact.

We then introduce nucleation and island growth mechanism to the system. This model predicts kinetic roughing and rough spiral edges, which show qualitative agreement with experimental observation. By introducing island growth with the screw dislocation initial condition, we reveal how spiral evolving and island growth interact and correlate.

While the phase field approach is promising in many respects, its results depend on parameters that are difficult to evaluate for real systems. While qualitative results are illuminating, more study will be needed for these tools to be quantitatively predictive of actual growth systems.

Bibliography

[1] T. R. Albrecht, S. Akamine, T. E. Carver, and C. F. Quate. Microfavrication of cantilever styli for the atomic force microscope. J. Vac. Sci. Technol. A, 8:3386–3396, 1990. 23

[2] S. Alexander, L. Hellemans, O. Marti, J. Schneir, V. Elings, P. K. Hansma, M. Longmire, and J. Gurley. An atomic resolution atomic force microscope implemented using an optical lever. Journal of Applied Physics, 65(1):164 –167, jan 1989. 23

[3] H. Alexandru and S. Antohe. Prismatic faces of kdp crystal, kinetic and mechanism of growth from solutions. Journal of Crystal Growth, 258(12):149 – 157, 2003. 51

[4] H. V. Alexandru and S. Antohe. Prismatic faces of kdp crystal, kinetic and mechanism of growth from solutions. Journal of Crystal Growth, 258:149–157, Oct 2003. 52

[5] P. Anandan and R. Jayavel. Crystal growth and characterization of semiorganic single crystals of l-histidine family for nlo applications. Journal of Crystal Growth, 322(1):69 – 73, 2011. 2

[6] T. Ando, N. Kodera, E. Takai, D. Maruyama, K. Saito, and A. Toda. A high-speed atomic force microscope for studying biological macromolecules. Proceedings of the National Academy of Sciences, 98(22):12468–12472, 2001. 73

[7] P. Antinozzi, C. Brown, and D. Punch. Calcium oxalate monohydrate crystallization: citrate inhibition of nucleation and growth steps. Journal of Crystal Growth, 125:215–222, 1992. 51

[8] J. Baird, R. McFeeters, and K. Caraballo. Specific rate of protein crystallization determined by the guggenheim method. International Journal of Thermophysics, pages 1–11, 2013. 51

[9] S. Balay, V. Eijkhout, W. D. Gropp, L. C. McInnes, and B. F. Smith. Efficient Management of Parallelism in Object Oriented Numerical Software Libraries. Birkhauser Press, 1997. 36

[10] J. B. Baxter, A. M. Walker, K. van Ommering, and E. S. Aydil. Synthesis and characterization of zno nanowires and their integration into dye-sensitized solar cells. Nanotechnology, 17:304–312, 2006. xi, 2, 75, 77, 78, 79, 81, 90

[11] W. J. E. Beek, M. M. Wienk, and R. A. J. Janssen. Hybrid solar cells from regioregular polythiophene and zno nanoparticles. Adv. Mater., 86:1009–1013, 2005. 75

[12] F. H. Bertrand, M. R. Gadbois, and P. A. Tanguy. Tetrahedral elements for fluid flow. Int. J. Num. Meth. Eng., 33:1251–1267, 1992. 36

[13] K. Binder and P. Fratzl. G. kostorz, editor. Phase Transformations in Materials, page 409, 2001. 4

[14] G. Binnig, C. F. Quate, and C. Gerber. Atomic force microscope. Phys. Rev. Lett., 56(9):930–933, Mar 1986. ix, 14, 24

[15] G. Binning, C. Gerber, E. Stoll, T. R. Albrecht, and C. F. Quate. Atomic resolution with the atomic force microscope. Europhys. Letts, 3:1281–1286, 1987. 21

[16] R. B. Bird, W. E. Stewart, and E. N. Lightfoot. Transport Phenomena. John Wiley and Sons, 1960. 31, 32

[17] J. E. Boercker, J. B. Schmidt, and E. S. Aydil. Transport limited growth of zinc oxide nanowires. Crystal Growth and Design, 9(6):2783–2789, 2009. 80

[18] P. F. Bordui and S. Motakef. Hydrodynamic control of solution inclusion during crystal growth of $ktiopo_4$ (KTP) from high-temperature solution. Journal of Crystal Growth, 96:405–412, 1989. 10

[19] J. C. Brice. The Growth of Crystals from Liquids. North-Holland Physics Publishing, Amsterdam, The Netherlands, 1973. 2

[20] A. N. Brooks and T. J. R. Hughes. Streamline Upwind/Petrov-Galerkin Formulations for convection dominated flows with particular emphasis on the incompressible Navier-Stokes equations. Comput. Methods Appl. Mech. Engrg., 32:199–259, 1982. 45

[21] W. Burton, N. Carbrera, and F. Frank. The growth of crystal and the equilibrium structure of their surfaces. Philosophical Transactions of the Royal Society A, 243:299–358, 1951. 83

[22] W. K. Burton and N. Cabrera. Crystal growth and surface structure. part i. Discuss. Faraday Soc., 5:33–39, 1949. 7, 8

[23] W. K. Burton, N. Cabrera, and F. C. Frank. The growth of crystals and the equilibirum structure of their surfaces. Phil. Trans. Roy. Soc. London, 243(R-2):299–358, 1951. 7, 8

[24] N. Cabrera and R. V. Coleman. The Art and Science of Growing Crystals. John Wiley, 1963. 1, 98

[25] P. L. Chambr and A. Acrivos. On chemical surface reactions in laminar boundary layer flows. Journal of Applied Physics, 27(11):1322–1328, 1956. 62

[26] A. Chernov. Formation of crystals in solutions. Contemporary Physics, 30(4):251–276, 1989. 7

[27] A. Chernov and E. Givargizov. Modern crystallography III: crystal growth, volume 169. Springer-Verlag Berlin, 1984. 7

[28] A. A. Chernov. The spiral growth of crystals. Soviet Physics Uspekhi, 4:116–148, 1961. 7, 10

[29] A. A. Chernov. Protein crystals and their growth. Journal of Structural Biology, 142(1):3 – 21, 2003. Macromolecular crystallization in the structural genomics era. 51, 52

[30] B. Coles, R. Compton, J. Booth, Q. Hong, and G. Sanders. A hydrodynamic afm flow cell for the quantitative measurement of interfacial kinetics. Chemical Communications, pages 619–620, 1997. ix, 25, 26

[31] B. Coles, R. Compton, M. Suarez, J. Booth, Q. Hong, and G. Sanders. A hydrodynamic afm flow cell for the quantitative measurement of interfacial kinetics: the aqueous dissolution of salicylic acid and calcium carbonate. Langmuir, 14:218–225, 1998. 25

[32] M. Crouzeix and P. A. Raviart. Conforming and non-conforming finite element methods for solving the stationary stokes equation. Série Analyse Numérique, 7:33–76, 1973. 36

[33] S. A. de Vries, P. Goedtkindt, S. L. Bennett, W. J. Huisman, M. J. Zwanenburg, D.-M. Smilgies, J. J. De Yoreo, W. J. P. van Enckevort, P. Bennema, and E. Vlieg. Surface atomic structure of kdp crystals in aqueous solution: An explanation of the growth shape. Phys. Rev. Lett., 80(10):2229–2232, Mar 1998. 2

[34] W. Deen. Analysis of Transport Phenomena. Oxford University Press, 1998. 31

[35] S. Deganello and O. Piro. The crystal structure of calcium oxalate monohydrate (whewellite). Neues Jahrb Mineral Monatsh, 2:81, 1981. 51

[36] R. DeMattei and R. Feigelson. The solubility dependence of canavalin on ph and temperature. Journal of Crystal Growth, 110(1-2):34 – 40, 1991. 52

[37] J. Derby, S. Kuppurao, Q. Xiao, A. Yeckel, and Y. Zhou. Large-scale numerical modeling of bulk crystal growth from the melt and solution. In J. P. van der Eerden and O. S. L. Bruins, editors, Science and Technology of Crystal Growth, pages 111–122. Kluwer academic publishers, Dordecht, The Netherlands, 1995. 37

[38] J. J. Derby, Y.-I. Kwon, A. Pandy, P. Sonda, A. Yeckel, T. Jung, and G. Muller. Developing quantitative, multiscale models for microgravity crystal growth. Annals of the New York Academy of Sciences, 1077:124–145, 2006. 36

[39] J. J. Derby, Y.-I. Kwon, J. C. Rojo, B. Vartak, and A. Yeckel. Finite element modeling of 3d fluid dynamics in crystal growth systems. International Journal of Computational Fluid Dynamics, 12(3-4):225–240, 1999. 49

[40] S. B. Dubin, G. Feher, and G. B. Benedek. Study of the chemical denaturation of lysozyme by optical mixing spectroscopy. Biochem, 12:714–719, 1973. 52

[41] S. D. Durbin and W. E. Carlson. Lysozyme crystal growth studied by atomic force microscopy. Journal of Crystal Growth, 122(14):71 – 79, 1992. 51

[42] M. V. Dyke. Album of Fluid Motion. The Parab olic Press, Stanford, California, 1982. 49

[43] D. Elwell and H. J. Scheel. Crystal Growth from High-Temperature Solutions. Academic Press, New York, 1975. 2

[44] H. J. Fan, P. Werner, and M. Zacharias. Semiconductor nanowires: From self-organization to patterned growth. Small, 2(6):700–717, 2006. xi, 76

[45] Z. Fan, J. C. Ho, Z. A. Jacobson, R. Yerushalmi, R. L. Alley, H. Razavi, and A. Javey. Wafer-scale assembly of highly ordered semiconductor nanowire arrays by contact printing. Nano Letters, 8(1):20–25, 2008. PMID: 17696563. 77

[46] B. A. Finlayson. The Method of Weighted Residuals and Variational Principles, with Application in Fluid Mechanics, Heat and Mass Transfer. Academic Press, 1972. 41

[47] B. A. Finlayson and L. E. Scriven. The method of weighted residuals - a review. Applied Mechanics Reviews, 19:735–748, 1966. 41

[48] F. C. Frank. The influence of dislocations on crystal growth. Discuss. Faraday Soc., 5:48–54, 1949. 7, 8

[49] K. Fujioka, S. Matsuo, T. Kanabe, H. Fujita, and M. Nakatsuka. Optical properties of rapidly grown kdp crystal improved by thermal conditioning. Journal of Crystal Growth, 181(3):265 – 271, 1997. 51

[50] D. Gasperino, A. Yeckel, B. K. Olmsted, M. D. Ward, and J. J. Derby. Mass Transfer Limitations at Crystallizing Interfaces in an Atomic Force Microscopy Fluid Cell: A Finite Element Analysis. Langmuir, 22:6578–6586, 2006. viii, ix, 16, 28, 29, 30, 36, 41, 51, 53, 72

[51] D. Gasperino, A. Yeckel, B. K. Olmsted, M. D. Ward, and J. J. Derby. Mass transfer limitations at crystallizing interfaces in an atomic force microscopy fluid cell: a finite element analysis. Langmuir, 22(15):6578–6586, 2006. PMID: 16831000. 52

[52] D. J. Gasperino. Modeling of transport processes during solution, melt and colloidal crystal growth. Thesis, University of Minnesota, 2008. x, 49, 50, 72

[53] R. Ghez and G. H. Gilmer. An analysis of combined surface and volume diffusion processes in crystal growth ii. asymmetric capture at steps. Journal of Crystal Growth, 21:93–109, 1974. 10

[54] G. H. Gilmer, R. Ghez, and N. Cabrera. An analysis of combined surface and volume diffusion processes in crystal growth. Journal of Crystal Growth, 8:79–93, 1971. 10

[55] L. J. Griffin. Observation of uni-molecular growth steps on crystal surfaces. Phil. Mag., 41:196–199, 1950. 8

[56] S. Guo, M. Ward, and J. Wesson. Direct visualization of calcium oxalate monohydrate (com) crystallization and dissolution with atomic force microscopy (afm) and the role of polymeric additives. Langmuir, 18:4284, 2002. 51

[57] N. Gvozdev, E. Petrova, T. Chernevich, O. Shustin, and L. Rashkovich. Atomic force microscopy of growth and dissolution of calcium oxalate monohydrate (com) crystals. Journal of Crystal Growth, 261:539–548, 2004. 51

[58] N. V. Gvozdev, E. V. Petrova, T. G. Chernevich, O. A. Shustin, and L. N. Rashkovich. Atomic force microscopy of growth and dissolution of calcium oxalate monohydrate (COM) crystals . Journal of Crystal Growth, 261:539–548, 2004. 14, 34

[59] A. Hilger. *KDP*-family Single Crystals. Bristol, Philadelphia and New York, 1991. 52

[60] J. H. Hoh and P. K. Hansma. Atomic force microscopy for high-resolution imaging in cell biology. Trends in Cell Biology, 2(7):208 – 213, 1992. 14

[61] Q. Hong, M. Suarez, B. Coles, and R. Compton. Mechanism of solid/liquid interfacial reactions. the maleic acid driven dissolution of calcite: an atomic force microscopy study under defined hydrodynamic conditions. Journal of Physical Chemistry B, 101:5557–5564, 1997. 25

[62] Y.-J. Huang, M.-F. Shih, C.-C. Liu, S.-Y. Chu, and K.-Y. Lo. Effect of arsenic implantation dose on p-type zno films obtained via thermal diffusion from silicon substrates. Electrochemical and Solid-State Letters, 13(11):H373–H375, 2010. 75

[63] T. J. R. Hughes, L. P. Franca, and G. M. Hulbert. A new finite element formulation for computational fluid dynamics: VIII. The Galerkin/least-squares method for advective-diffusive equations. Comput. Methods Appl. Mech. Engrg., 73:173–189, 1989. 45

[64] J. C. Jacco, G. M. Loiacono, M. Jaso, G. Mizell, and B. Greenberg. Flux growth and properties of $ktiopo_4$. Journal of Crystal Growth, 70:484–488, 1984. 2

[65] T. Jung, X. Sheng, C. K. Choi, W.-S. Kim, J. A. Wesson, and M. D. Ward. Probing crystallization of calcium oxalate monohydrate and the role of macromolecule additives with in situ atomic force microscopy. Langmuir, 20(20):8587–8596, 2004. PMID: 15379479. viii, 16, 18

[66] T. Jung, X. Sheng, C. K. Choi, W.-S. Kim, J. A. Wesson, and M. D. Ward. Probing crystallization of calcium oxalate monohydrate and the role of macromolecule additives with in situ atomic force microscopy. Langmuir, 20:8587, 2004. 49, 51

[67] W. Kadima, A. McPherson, M. Dunn, and F. Jurnak. Characterization of precrystallization aggregation of canavalin by dynamic light scattering. Biophysical Journal, 57(1):125 – 132, 1990. 52

[68] A. Karma and M. Plapp. Spiral surface growth without desorption. Physical Review Letters, 81:4444–4447, 1998. 86, 90

[69] A. Karma and W.-J. Rappel. Quantitative phase-field modeling of dendritic growth in two and three dimensions. Physical Review E, 57:4323–4349, 19998. 85, 88

[70] R. Könenkamp, R. C. Word, and C. Schlegel. Vertical nanowire light-emitting diode. Appl. Phys. Lett., 85:6004, 2004. 75

[71] W. Kossel. Zui Theorie Der Kristallwachstums. Nachur. Ges. Gottingen, 2:135–145, 1927. 8

[72] F. Kuemmeth, A. R. Champagne, A. J. Couture, and D. C. Ralph. Nanometer-scale scanning sensors fabricated using stencil lithography. Applied Physics Letters, 82:1111–1113, 2003. 21

[73] Y. Kwon, B. Dai, and J. Derby. Assessing the dynamics of liquid-phase solution growth via step growth models: From bcf to fem. Progress in Crystal Growth and Characterization of Materials, 2007. 10

[74] Y.-I. Kwon. Continuum transport and meso-scale step growth models for solution crystal growth. PhD thesis, Univeristy of Minnesota, 2007. 36, 49

[75] Y.-I. Kwon and J. Derby. Modeling the coupled e?ects of interfacial and bulk phenomena during solution crystal growth. Journal of Crystal Growth, 230:328–335, 2001. 10

[76] M. Law, L. E. Greene, J. C. Johnson, R. Saykally, and P. D. Yang. Nanowire dye-sensitized solar cells. Nat. Matter., 4:455–459, 2005. 77, 78

[77] P. Leblanc and G. S. Frankel. A study of corrosion and pit ting initiation AA2024-T3 using atomic force microscopy. Journal of the Electrochemical Society, 149:B239B247, 2002. 14

[78] A. Y. Lee, D. Erdemir, and A. S. Myerson. Crystal polymorphism in chemical process development. Annual Review of Chemical and Biomolecular Engineering, 2(1):null, 2011. 2

[79] H. Lin, F. Rosenberger, J. Alexander, and A. Nadarajah. Convective-diffusive transport in protein crystal growth. Journal of crystal growth, 151(1):153–162, 1995. 10

[80] H. Lin, P. G. Vekilov, and F. Rosenberger. Facet morphology response to nonuniformities in nutrient and impurity supply ii. numerical simulations. Journal of Crystal Growth, 158:552–559, 1996. 10

[81] F. Liu and H. Metiu. Stability and kinetics of step motion on crystal surfaces. Physical Review E, 49:2601–2616, 1994. 85

[82] X. Lu, T. Hanrath, K. P. Johnston, and B. A. Korgel. Growth of single crystal silicon nanowires in supercritical solution from tethered gold particles on a silicon substrate. Nano Letters, 3:93–99, 2003. 2

[83] A. J. Malkin, Y. G. Kuznetsov, and A. McPherson. AFM studies of the nucleation and growth mechanisms of macromolecular crystals. Journal of Crystal Growth, 196:489–502, 1999. 14

[84] A. McPherson and R. Spencer. Preliminary structure analysis of canavalin from jack bean. Archives of Biochemistry and Biophysics, 169(2):650 – 661, 1975. 52

[85] E. A. Meulenkamp. Synthesis and growth of zno nanoparticles. J. PHys. Chem. B, 102:5566–5572, 1998. 2

[86] G. Meyer and N. M. Amer. Novel optical approach to atomic force microscopy. Applied Physics Letters, 53(12):1045 –1047, sep 1988. 23

[87] V. J. Morris, A. R. Kirby, and A. P. Gunning. Atomic Force Microscopy for Biologists. Imperial College Press, 1999. 14, 21

[88] G. M?ller and J. Friedrich. Crystal growth, bulk: Methods. In E. in Chief: Franco Bassani, G. L. Liedl, , and P. Wyder, editors, Encyclopedia of Condensed Matter Physics, pages 262 – 274. Elsevier, Oxford, 2005. viii, 2, 3

[89] A. Nadarajah, F. Rosenberger, and J. I. D. Alexander. Modelling the solution growth of tgs crystals in low gravity. Journal of crystal growth, 104(2):218–232, 1990. 10

[90] M. Nakatsuka, K. Fujioka, T. Kanabe, and H. Fujita. Rapid growth over 50 mm/day of water-soluble kdp crystal. Journal of Crystal Growth, 171(34):531 – 537, 1997. 51

[91] G. Nancollas and G. Gardner. Kinetics of crystal growth of calcium oxalate monohydrate. Journal of Crystal Growth, 21:267–276, 1974. 51

[92] B. O'Regan and M. Gratzel. A low-cost, high-efficiency solar cell based on dye-sensitized colloidal tio2 films. Nature, 353(6346):737–740, 1991. 77

[93] O. Penrose and P. C. Fife. Thermodynamically consistent models of phase-field type for the kinetic of phase transitions. Physica D, 1:44–62, 1990. 86

[94] L. Prandtl. über flüssigkeitsbewegung bei sehr kleiner reibung. Intern. Math. Kongr., Verh. III:484–491, 1904. 17

[95] A. Ratkovich and R. L. Penn. Zinc oxide nanoparticle growth from homogenous solution: Inuence of zn:oh, water concentration, and surfactant additives. Materials Research Bulletin, 44:993–998, 2009. 2

[96] A. R*ä*tz and A. Voigt. Various phase-field approximations for epitaxial growth. Journal of Crystal Growth, 266:278–282, 2004. 85

[97] Y. Saad. Highly parallel preconditioners for general sparse matrices. In G. Golub, A. Greenbaum, and M. Luskin, editors, Recent Advances in Iterative Methods, pages 165–99. Springer-Verlag, New York, 1994. 48

[98] Y. Saad and M. Schultz. GMRES: A generalized minimum residual algorithm for solving nonsymmetric linear systems. SIAM J. Sci. Stat. Comput., 7:856–69, 1986. 48

[99] A. G. Salinger. The interactions of transport mechanisms in convecting and reacting systems. PhD thesis, University of Minnesota, 1993. 49

[100] A. G. Salinger, Q. Xiao, Y. Zhou, and J. J. Derby. Massively parallel finite element computations of three-dimensional, time-dependent, incompressible flows in materials processing systems. Computer Methods in Applied Mechanics and Engineering, 119(1):139–156, 1994. 10

[101] A. G. Salinger, Q. Xiao, Y. Zhou, and J. J. Derby. Massively parallel finite element computations of three-dimensional, time-dependent, incompressible flows in materials processing systems. Computer Methods in Applied Mechanics and Engineering, 119(12):139 – 156, 1994. 49

[102] A. G. Salinger, Q. Xiao, Y. Zhou, and J. J. Derby. Massively parallel finite element computations of three-dimensional,time-dependent, incompressible flows in materials processing systems. Comput. Methods Appl. Mech. Engrg., 119:139–156, 1994. 37

[103] T. E. Schaffer and H. Fuchs. Optimized detection of normal vibration modes of atomic force microscope cantilevers with the optical beam deflection method. Journal of Applied Physics, 97(8):083524, 2005. 23

[104] H. J. Scheel. Historical aspects of crystal growth technology. Journal of Crystal Growth, 211:1–12, 2000. 1

[105] G. Schitter, P. Menold, H. Knapp, F. Allgower, and A. Stemmer. High performance feedback for fast scanning atomic force microscopes. Review of Scientific Instruments, 72(8):3320–3327, 2001. 73

[106] H. Schlichting and K. Gersten. Boundary Layer Theory. Springer, 1999. 17

[107] H. Schlichting and K. Gersten. Boundary Layer Theory. Springer-Verlag, 8th edition, 2004. 60

[108] W. Schmidt and R. Alkire. Use of atomic force microscopy to image surfaces during fluid flow. Journal of the Electrochemical Society, 141:85–87, 1994. 25

[109] L. Schmidt-Mende and J. L. MacManus-Driscoll. Zno - nanostructures, defects, and devices. Materials Today, 10(5):40 – 48, 2007. 77

[110] J. D. Schmit and K. Dill. Growth rates of protein crystals. Journal of the American Chemical Society, 134(9):3934–3937, 2012. 51

[111] H. Sefidroodi, P. C. Chua, and M. A. Kelland. Thf hydrate crystal growth inhibition with small anionic organic compounds and their synergistic properties with the kinetic hydrate inhibitor poly(n-vinylcaprolactam). Chemical Engineering Science, 66(10):2050 – 2056, 2011. 2

[112] X. Sheng, T. Jung, J. A. Wessen, and M. D. Ward. Adhesion at calcium oxalate crystal surfaces and the effect of urinary constituents . National Academy of Science USA, 102:267, 2004. 14

[113] Y. Shirane, Y. Kurokawa, S. Miyashita, H. Komatsu, and S. Kagawa. Study of inhibition mechanisms of glycosaminoglycans on calcium oxalate monohydrate crystals by atomic force microscopy. Urological Research, 27:426–431, 1999. 51

[114] B. R. Silver, V. Fulop, and P. R. Unwin. Protein crystallization at oil/water interfaces. New J. Chem., 35:602–606, 2011. 2

[115] I. N. Stranski. Zum Problem des Kristallwachstums. Z. Phys. Chem., 102:267–275, 1922. 8

[116] M. Sugiyama, D. Gasperino, J. J. Derby, and V. H. Barocas. Proteinsaltwater solution phase diagram determination by a combined experimental–computational scheme. Crystal Growth & Design, 8(12):4208–4214, 2008. 51

[117] Y. Takeda, T. Kondow, and F. Mafun. Self-assembly of gold nanoparticles in protein crystal. Chemical Physics Letters, 504(4-6):175 – 179, 2011. 2

[118] J. Tansock and C. Williams. Force measurement with a piezoelectric cantilever in a scanning force microscope. Ultramicroscopy, 42-44(Part 2):1464 – 1469, 1992. 23

[119] T. E. Tezduyar. Stabilized finite element formulations for incompressible flow computations. In J. W. Hutchinson and T. Y. Wu, editors, Advances in Applied Mechanics, pages 1–44. Academic Press, Inc., 1992. 45

[120] T. E. Tezduyar, S. Aliabadi, M. Behr, and S. Mittal. Massively parallel finite element simulation of compressible and incompressible flows. Computer Methods in Applied Mechanics and Engineering, 119(1):157–177, 1994. 10

[121] T. E. Tezduyar, R. Shih, and S. Mittal. Time-accurate incompressible flow computations with quadrilateral velocity-pressure elements. University of Minnesota Supercomputer Institute Research Report, UMSI 90/143, August 1990. 45

[122] M. Tortonese, R. C. Barrett, and C. F. Quate. Atomic resolution with an atomic force microscope using piezoresistive detection. Applied Physics Letters, 62(8):834 –836, feb 1993. 23

[123] G. M. Turner, M. C. Beard, and C. A. Schmuttenmaer. Carrier localization and cooling in dye-sensitized nanocrystalline titanium dioxide. The Journal of Physical Chemistry B, 106(45):11716–11719, 2002. 78

[124] H. E. Unalan, Y. Zhang, P. Hiralal, S. Dalal, D. Chu, G. Eda, K. B. K. Teo, M. Chhowalla, W. I. Milne, and G. A. J. Amaratunga. Zinc oxide nanowire networks for macroelectronic devices. Applied Physics Letters, 94(16):163501, 2009. 76

[125] J. van de Lagemaat and A. J. Frank. Nonthermalized electron transport in dye-sensitized nanocrystalline tio2 films: transient photocurrent and random-walk modeling studies. The Journal of Physical Chemistry B, 105(45):11194–11205, 2001. 78

[126] L. Vayssieres, K. Keis, A. Hagfeldt, and S.-E. Lindquist. Three-dimensional array of highly oriented crystalline zno microtubes. Chemistry of Materials, 13(12):4395–4398, 2001. 78

[127] P. G. Vekilov, J. I. D. Alexander, and F. Rosenberger. Nonlinear response of layer growth dynamics in the mixed kineticsbulk-transport regime. Phys. Rev. E, 54:6650–6660, 1996. 10

[128] P. G. Vekilov, H. Lin, and F. Rosenberger. Unsteady crystal growth due to step-bunch cascading. Phys. Rev. E, 55:3202–3214, 1997. 10

[129] S.-L. Wang, R. Sekerka, A. Wheeler, B. Murray, S. Coriell, R. Braun, and G. McFadden. Thermodynamically-consistent phase-field models for solidification. Physica D, 69:189 – 200, 1993. 86

[130] W. Wang. Modeling of Continuum Transport and Meso-Scale Kinetics during Solution Crystal Growth. PhD thesis, University of Minnesota, 2014. 49

[131] Z. L. Wang. Zinc oxide nanostructures: growth, properties and applications. Journal of Physics: Condensed Matter, 16(25):R829, 2004. 77

[132] Z. L. Wang and J. Song. Piezoelectric nanogenerators based on zinc oxide nanowire arrays. Science, 312(5771):242–246, 2006. 77

[133] M. D. Ward. Snapshots of crystal growth. Science, 308:1566, 2005. 49

[134] M. D. Ward, S. Guo, and J. A. Wesson. Direct Visualization of Calcium Oxalate Monohydrate (COM) Crystallization and Dissolution with Atomic Force Microscopy (AFM) and the Role of Polymeric Additives . Langmuir, 18:4284, 2002. 14

[135] M. D. Ward, X. Sheng, T. Jung, and J. A. Wesson. Probing adhesion forces and macromolecule binding at calcium oxalate single crystal surfaces: towards an understanding of kidney stone formation. Polymeric Materials Science and Engineering, 90:273, 2004. 51

[136] J. M. Watkins, D. J. DePaolo, F. J. Ryerson, and B. T. Peterson. Influence of liquid structure on diffusive isotope separation in molten silicates and aqueous solutions. Geochimica et Cosmochimica Acta, 75(11):3103 – 3118, 2011. 2

[137] G. H. Westphal and F. Rosenberger. On diffusive-advective interfacial mass transfer. Journal of Crystal Growth, 43:687–693, 1978. 34

[138] R. Wiesendanger. Contributions of scanning probe microscopy and spectroscopy to the investigation and fabrication of nanometer scale structures. Journal of Vacuum Science Technology B: Microelectronics and Nanometer Structures, 12(2):515 –529, mar 1994. 14

[139] S. Wilkins, M. Suarez, Q. Hong, B. Coles, and R. Compton. Atomic force microscopy under defined hydrodynamic conditions: three-dimensional flow calculations applied to the dissolution of salicylic acid. Journal of Physical Chemistry B, 104:1539–1545, 2000. ix, 27

[140] E. Williams, N. Bartelt, et al. Thermodynamics of surface morphology. Science, 251(4992):393–400, 1991. 7

[141] Q. Xiao, A. G. Salinger, Y. Zhou, and J. J. Derby. Massively parallel finite element analysis of coupled, incompressible flows: A benchmark computation of baroclinic annulus waves. International journal for numerical methods in fluids, 21(10):1007–1014, 1995. 10

[142] Q. Xiao, A. G. Salinger, Y. Zhou, and J. J. Derby. Massively parallel finite element analysis of coupled, incompressible flows: A benchmark computation of baroclinic annulus waves. Intern. J. Numer. Meths. Fluids, 21:1007–1014, 1995. 37

[143] D. Xu and D. Xue. Chemical bond analysis of the crystal growth of kdp and adp. Journal of Crystal Growth, 286(1):108 – 113, 2006. 2

[144] M. Yang, D. Wang, L. Peng, Q. Zhao, Y. Lin, and X. Wei. Surface photocurrent gas sensor with properties dependent on ru(dcbpy)2(ncs)2-sensitized zno nanoparticles. Sens. Actuators B, 117:80–85, 2006. 75

[145] A. Yeckel and J. J. Derby. Numerical experiments in diagonal preconditioning with applications to incompressible flows in materials processing. submitted, 1996. 48

[146] A. Yeckel and J. J. Derby. Parallel computation of incompressible flows in materials processing: Numerical experiments in diagonal preconditioning. Parallel Computing, 23(9):1379 – 1400, 1997. Parallel computing methods in applied fluid mechanics. 49

[147] A. Yeckel, Y. Zhou, M. Dennis, and J. J. Derby. Three-dimensional computations of solution hydrodynamics during the growth of potassium dihydrogen phosphate: Ii. spin down. Journal of crystal growth, 191(1):206–224, 1998. 10

[148] M. Yokokawa, C. Wada, T. Ando, N. Sakai, A. Yagi, S. H. Yoshimura, and K. Takeyasu. Fast-scanning atomic force microscopy reveals the ATP/ADP-dependent conformational changes of GroEL. EMBO, 25:4567 – 4576, 2006. 73

[149] J. D. Yoreo, Z. Rek, N. Zaitseva, and B. Woods. Sources of optical distortion in rapidly grown crystals of kh_2po_4. Journal of Crystal Growth, 166:291–297, 1996. viii, 7, 11

[150] J. J. D. Yoreo, H. Teng, and P. M. Dove. Kinetics of calcite growth: Interpreting chemical affinity-based rate laws through the lens of direct observation. Journal of Crystal Growth, 166:291, 1996. 17, 25

[151] J. J. D. Yoreo and P. G. Vekilov. Principles of crystal nucleation and growth. Reviews in Mineralogy and Geochemistry, pages 57–93, 2003. viii, 4, 5, 7

[152] Y.-M. Yu and B.-G. Liu. Contrasting morphologies of o-rich zno epitaxy on zn- and o-polar thin film surfaces: Phase-field model. Phys. Rev. B, 77:195327, May 2008. 87

[153] R. Zauner and A. G. Jones. Determination of nucleation, growth, agglomeration and disruption kinetics from experimental precipitation data: the calcium oxalate system. Chemical Engineering Science, 55:4219–4232, 2000. 51

[154] Y. Zhou and J. J. Derby. Three-dimensional computations of solution hydrodynamics during the growth of potassium dihydrogen phosphate i. spin up and steady rotation. Journal of crystal growth, 180(3):497–509, 1997. 10

[155] O. Zienkiewicz and R. Taylor. The Finite Element Method Volume 3: Fluid Dynamics. Butterworth-Heinemann, 2000. 43